

Aus der Sektion für Translationale Neurodegeneration „Albrecht Kossel“

Klinik und Poliklinik für Neurologie der Universitätsmedizin Rostock

Sektionsleiter: Prof. Dr. Dr. Andreas Hermann

Themenvergebender Hochschullehrer: PD Dr. phil. nat. habil. Moritz Frech

**In Vitro Disease Modeling and Pathophysiological
Characterization of Fatty Acid Hydroxylase-Associated
Neurodegeneration**

Inauguraldissertation

zur Erlangung des akademischen Grades

Doktor der Medizinwissenschaften (Doctor rerum humanarum)

der Universitätsmedizin Rostock

vorgelegt von

Fatima Efendic, geb. am 22.02.1991 in Bosnia and Herzegovina

Rostock, 13.09. 2024



Dieses Werk ist lizenziert unter einer
Creative Commons Namensnennung 4.0 International Lizenz.

FIRST REVIEWER: Prof. Dr. med. Andreas Wree

SECOND REVIEWER: Prof. Dr. Philip Seibler

THIRD REVIEWER: Prof. Dr. Dr. Andreas Hermann

DATE OF DEFENCE: 19.02.2025

Table of contents

1	Introduction	1
1.1	Fatty Acid Hydroxylase-Associated Neurodegeneration	1
1.2	Fatty Acid 2-Hydroxylase	2
1.2.1	Cell signaling via FA2H	4
1.2.2	FA2H-KO animal model.....	6
1.2.3	FA2H in Human Diseases	8
1.3	Oligodendrocyte development.....	9
1.3.1	Myelin formation and function.....	11
1.3.2	Myelin composition and wrapping	12
1.3.3	Protection of axon	14
1.3.4	Node formation	15
1.3.5	Demyelination in neurodegenerative disorders.....	17
1.4	Autophagy impairments and neurodegeneration	18
1.4.1	Autophagy in the neurodegenerative disease FAHN	19
1.5	Human iPS cells as disease models	20
2	Aim	23
3	Materials and methods	24
3.1	Material.....	24
3.1.1	Instruments.....	24
3.1.2	Chemicals and reagents.....	25
3.1.3	Cell culture media and supplements	28
3.1.4	Antibodies and primers	31
3.1.5	Cell culture media	37
3.1.6	Cell lines.....	39
3.2	Cultivation of the cell lines.....	40
3.2.1	Cell culture medium.....	40
3.2.2	Coatings	42
3.2.3	Matrigel coating.....	42
3.2.4	Poly-L-ornithine/ Laminin coating	42
3.2.5	Cell count	42
3.2.6	Freezing and thawing of cells	43
3.2.7	Cultivation of human fibroblasts and HEK293T cells.....	44
3.3	Generation of iPSCs from Fibroblasts	44
3.3.1	Reprogramming human fibroblasts into iPSCs	44
3.3.2	Expansion and maintenance of human iPSCs.....	45
3.4	Characterization of iPSCs	46
3.4.1	Alkaline phosphatase staining	46
3.4.2	Sample preparation for karyotyping.....	46
3.4.3	Differentiation of human iPSCs into three germ layers.....	46
3.4.4	Sample preparation for short tandem repeat analysis.....	47

3.4.5	Flow cytometry	47
3.4.6	Sample preparation for targeted sequencing	48
3.4.7	Immunofluorescence staining of iPSCs and EBs	48
3.4.8	qRNA isolation, reverse transcription and quantitative polymerase chain reaction ..	48
3.4.9	Agarose gel electrophoresis	50
3.4.10	Immunofluorescence Staining	50
3.5	Differentiation of iPSCs into neural progenitor cells (NPCs).....	51
3.5.1	Cultivation of neural progenitor cells	51
3.5.2	Cultivation of neural differentiated cells.....	51
3.5.3	Differentiation of iPSCs into neural progenitor cells (NPCs)	51
3.6	Differentiation of iPSCs into Oligodendrocyte progenitor cell (OPCs).....	52
3.6.1	Cultivation of oligodendrocyte progenitor cells and Oligodendrocyte	52
3.6.2	Differentiation of iPSCs into Oligodendrocyte progenitor cell (OPCs)	53
3.6.3	Reproduction of lentivirus vectors	53
3.6.4	Lentivirus virus generation	54
3.6.5	Titer determination	55
3.6.6	Differentiation of iPSCs into OLIG2+ precursors.....	55
3.6.7	Derivation of OPCs form iPSCs.....	56
3.6.8	O4-based purification	57
3.6.9	Checking the purity of O4 expression in a small fraction of the O4+ cells by FACS	58
3.7	Coculture of maturing iPSCs-derived neurons and O4+ OLs	58
3.7.1	Cultivation of Coculture	58
3.7.2	Coculture of maturing iPSCs-derived neurons and O4+ OLs	58
3.8	Protein Isolation and Western Blot.....	59
3.8.1	Protein isolation.....	59
3.8.2	Protein concentration measurement	59
3.8.3	Gel preparation.....	60
3.8.4	Western Blot	61
3.9	Quantifications and Statistics	61
3.9.1	Colocalization Analyses.....	62
4	Results	63
4.1	Generation and characterization of iPSC line	63
4.1.1	Evidence of pluripotency	64
4.1.2	Analysis of transgene expression using RT-PCR.	67
4.1.3	<i>In vitro</i> trilineage differentiation potential of iPSCs	67
4.1.4	Analysis of Genetic Stability.....	68
4.1.5	Short tandem repeat analysis.....	68
4.1.6	FA2H Variants Analysis	69
4.2	Generation and Characterisation of Neural Progenitor Cells	69
4.3	Generation and Characterization of a Neural Differentiated Cells.....	71
4.4	Generation of iPSC-derived oligodendrocytes.....	74

4.5	Coculture of iPSC-derived oligodendrocytes and neurons	80
4.6	Pathophysiological characterizations of FAHN disease	82
4.6.1	FA2H protein expression in FA2H-deficient cells.....	82
4.6.2	Subcellular localization of the FA2H protein	83
4.6.3	Characterization of the Oligodendrocyte and Coculture	86
4.6.4	Myelin sheath examination and Ranvier node.....	94
4.7	Analysis of autophagy	98
5	Discussion.....	100
5.1	FAHN iPSCs model.....	100
5.1.1	iPSC generation.....	100
5.1.2	OPCs generation	100
5.1.3	Coculture generation.....	101
5.2	Pathophysiology of FAHN disease	102
5.3	Impairment of Myelin sheath in FA2H-Deficient Cells.....	105
5.4	Myelin sheath examination and Ranvier node	108
5.5	Autophagy is affected following loss of FA2H	111
6	Summary	114
7	Outlook.....	116
8	References.....	117
9	List of Figures	129
10	Table.....	131
11	Abbreviation.....	133
12	Additional figures.....	136
12.1	Characterisation of the cell systems.....	136
13	Acknowledgements.....	138
14	Declaration.....	139

1 Introduction

1.1 Fatty Acid Hydroxylase-Associated Neurodegeneration

Fatty acid hydroxylase-associated neurodegeneration (FAHN) emerges as a rare neurodegenerative disorder. In humans, autosomal recessive mutations in the enzyme fatty acid 2-hydroxylase, encoded by the *FA2H* gene, are implicated in FAHN OMIM (#611026) (Edvardson et al. 2005). These genetic anomalies are associated with a spectrum of neurodegenerative phenotypes, including leukodystrophy (as reported in OMIM #612319) (Uchida et al. 200; Edvardson et al. 2008), fatty acid hydroxylase associated neurodegeneration with brain iron accumulation (NBIA), and hereditary spastic paraplegia (HSP) type SPG35 (OMIM #612319), (Kruer et al. 2010; and Dick et al. 2010). The *FA2H* gene is integral to the conversion of ceramide into 2-hydroxyl sphingolipids, a critical component in myelin. Reductions in FA2H enzyme result in significant demyelination, particularly of the optic nerves and spinal cord (Potter et al.2010).

Initial explorations into mutations related to FAHN, conducted by Edvardson and colleagues (Edvardson et al. 2008), identified two distinct mutations presenting with variable clinical manifestations. One patient group displayed progressive spasticity and ataxia, while another exhibited mild gait disturbances and spasticity. An intronic *FA2H* mutation led to the production of an enzymatically inactive variant, while a missense mutation in another group led to a single amino acid change, substantially reducing the enzyme's activity, as confirmed through *in vitro* activity assays. The research of Edvardson et al (Edvardson et al. 2008), along with subsequent fibroblast analyses by Maier et al. (Maier et al. 2011), suggested the potential existence of a second enzyme with fatty acid 2-hydroxylase activity. Further mutations identified in unrelated families by Dick et al. supported these findings (Dick et al. 2008). These patients exhibited classic HSP and, in some cases, leukodystrophy. Notably, an *in vitro* functional assay showed that a mutation resulting in an amino acid exchange in one family retained 40-60% of the 2-OH ceramide levels compared to the wild-type enzyme. Conversely, an 18-base pair (bp) deletion within the cytochrome b5 domain in another family completely abolished enzyme activity (Zöller et al. 2008; Dick et al. 2008; Dick et al. 2010, Potter et al.2010).

To date, more than 106 cases of FAHN have been documented, with a variety of different *FA2H* mutations (Kruer et al. 2010; Garone et al. 2011; Tonelli et al. 2012; Cao et al. 2013; Rupps et

al. 2013; Donkervoort et al. 2014; Hashemi et al. 2023; German et al. 2023; Lidangzhi Mo et al. 2024).

1.2 Fatty Acid 2-Hydroxylase

The FA2H is identified as a monooxygenase enzyme with a critical molecular presence of 43 kDa localized to the membrane of the endoplasmic reticulum (ER), executing an essential function in the biosynthesis of 2-hydroxyacyl sphingolipids (Hama et al. 2010). This specialized enzyme refrains from acting on ceramides; rather, it employs fatty acids, which are subsequently transformed into hydroxylated sphingolipid variants (see Figure 1). This enzymatic process is characterized by its selectivity for fatty acid substrates, displaying a consistent pattern regardless of their saturation status (Mizutani et al. 2008). The initial identification of the human variant of this enzyme was credited to the investigative work of Alderson et al. (Alderson et al. 2004). They delineated its presence by comparing it to the well-established *FA2H*, noting predominant expression in the brain and pancreas, and a reduced presence in the kidneys. Continuing this line of inquiry, Eckhardt et al. explored a murine analog of the gene, correlating its expression with anatomical regions such as the brain, stomach, skin, kidney, and testes (Eckhardt et al. 2005). Their time-course analysis of gene expression in the brain indicated congruence with myelin gene expression profiles.

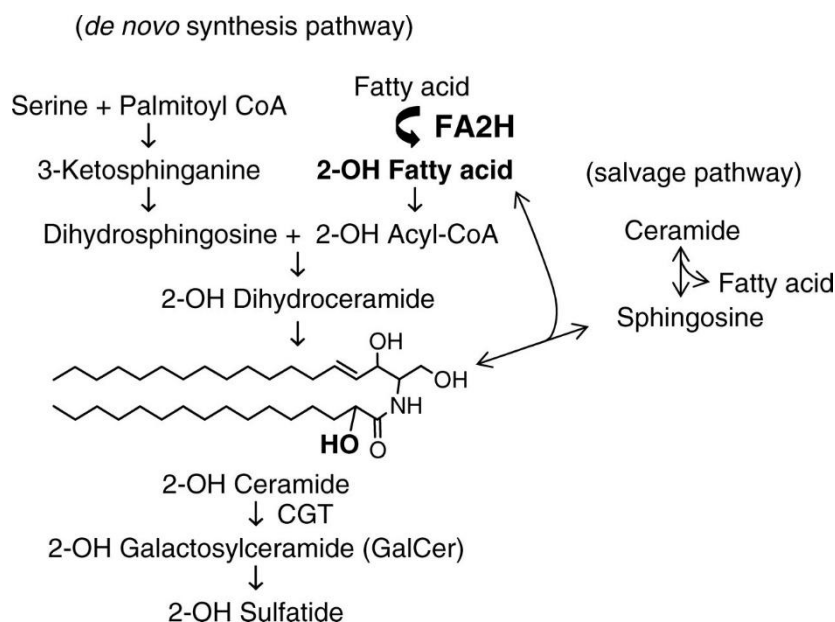


Figure 1: The process of 2-OH sphingolipid formation. The creation of these specific sphingolipids utilizes the same catalytic proteins as those for sphingolipids without hydroxylation, with a significant distinction. In this mechanism, 2-OH fatty acids generated by FA2H are incorporated by ceramide synthases, differing from their non-hydroxy analogs. Essentially, the process initiates with FA2H hydroxylating free fatty acids. Following this, Acyl-CoA synthetases (ACS) activate these 2-OH fatty acids. Subsequently, ceramide synthases (CerS) transform these activated 2-OH fatty acyl-CoAs into

dihydrosphingosine, creating 2-OH dihydroceramide. The conversion continues as dihydroceramide desaturase (DES) desaturates this intermediate, leading to 2-OH ceramide production. This 2-OH-ceramide acts as a foundational molecule that undergoes further alterations through various enzymes, culminating in the generation of diverse sphingolipids like sphingomyelins, glycosphingolipids, galactosylceramides, and sulphatides. This summary is based on the work of Nathan L. Alderson et al. from 2005.

The FA2H protein, comprising 372 amino acids, is tethered to the ER via four transmembrane domains, ensuring its proper orientation within the membrane (Figure 2). Its structure includes a conserved cytochrome b5 domain on the cytosolic side, noted for a heme-binding site at its N-terminus (residues 8-86). This site is posited to function as an electron acceptor site, pivotal for the enzyme's catalytic activity (Eckhardt et al. 2023). At the C-terminus of *FA2H* is a catalytic sterol desaturase domain, which is typical of ER-associated desaturases and hydroxylases (Shanklin and Cahoon, 1998; Eckhardt et al. 2005). This domain is composed of four conserved histidine-rich motifs, implicated in the chelation of iron and the subsequent electron donation to fatty acids. Additionally, an ER retention motif situated at the C-terminus underscores the enzyme's localization within the ER matrix. Despite the enzyme demonstrating the capability to hydroxylate free fatty acids *in vitro*, the replication of this activity *in vivo* conditions and its biological relevance remain to be conclusively determined (Alderson et al. 2005).

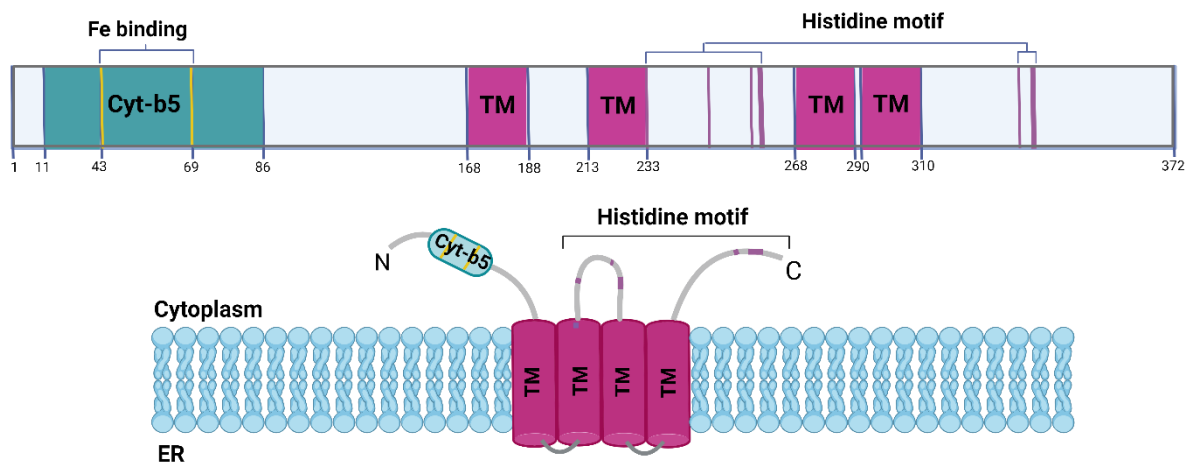


Figure 2: Domain organization of *FA2H* gene: The cytochrome b5 domain contains a conserved heme-binding domain. It has been demonstrated that the cytochrome b5 domain is required for optimal *FA2H* activity, and that it provides electrons to the catalytic di-iron. The *FA2H* catalytic domain has four putative transmembrane domains; the C-terminal tail is cytoplasmic. The catalytic site of *FA2H* has a histidine motif between transmembrane domains 2 and 3. It is proposed that the histidine residues in the motif coordinate the non-heme di-iron cluster at the active site. Figure created with BioRender.

In humans, animals, fungi, and protists, the FA2H enzyme features an N-terminal cytochrome b5-like domain responsible for electron transfer from NAD(P)H. However, plant enzymes lack this domain and instead interact with separate cytochrome b5 proteins within the ER membrane (Nagano, M. et al., 2012). It remains unclear if cytochrome b5 can partially substitute for the cytochrome b5-like domain, especially in cases of FA2H with mutations in this domain. The X-ray crystal structure of the baker's yeast FA2H enzyme (SCS7p) has been determined, although it lacks the N-terminal cytochrome b5-like domain (Zhu G. et al., 2015). This study confirmed the predicted four-transmembrane domain structure of the enzyme, with the N-terminal cytochrome b5 domain and C-terminus facing the cytosol (Alderson, N.L et al., 2004; Eckhardt M. et al., 2004; Zhu G. et al., 2015). Despite FA2H being a di-iron enzyme, the yeast ortholog has two zinc ions in the di-metal ion binding site (Zhu G. et al., 2015). Structural differences between SCS7p and the related stearoyl-CoA desaturase-1 (SCD1) suggest that acyl-CoAs are unlikely substrates for *FA2H/Scs7p*, whereas a ceramide fits well into the enzyme's catalytic center. Conversely, the only established *in vitro* FA2H assay used free fatty acids as an efficient substrate (Nagano, M. et al., 2012). It remains an open question whether free fatty acids serve as substrates *in vivo*. Heme, synthesized in mitochondria, must be transferred to the ER-localized FA2H protein when its cytochrome b5-like domain is properly folded. A screen for FA2H interaction partners identified progesterone receptor membrane component 1 (PGRMC1) as a binding partner of FA2H (Hardt, R. et al., 2018). PGRMC1 binds heme and is considered a putative heme chaperone (Piel, R.B. et al., 2016). Its yeast homolog (*Dap1*) is required for activating several CYP450 enzymes (Hughes, A.L et al., 2007). A PGRMC1 antagonist reduced FA2H activity (Hardt, R. et al., 2018), suggesting PGRMC1 might be involved in delivering heme to the cytochrome b5 domain of FA2H.

1.2.1 Cell signaling via FA2H

The foundational link between cellular differentiation and 2-OH glucosylceramides (GlcCer), play a crucial role in the maturation process of cultured human keratinocytes. The study illustrated that when *FA2H* levels were reduced using siRNA technology knockdown, it adversely affected the differentiation process, disrupting the formation of epidermal lamellar structures. The intricate relationship between *FA2H*, sphingolipids, and cellular differentiation has been further elucidated through the collective efforts of several research groups, including those led by Hiroko Hama, (Hama et al. 2009). Pivotal studies explored the effects of dibutyryl cAMP (dcAMP) on rat Schwann cells and D6P2T Schwannoma cells (Maldonado et al. 2008; Alderson et al. 2009 and Hama et al. 2009). The dcAMP is established as an agent that induces

the cessation of the cell cycle and promotes differentiation in Schwannoma cells. These studies consistently found that dcAMP exposure resulted in the upregulation of *FA2H* expression in both Schwann and Schwannoma cells. Intriguingly, siRNA-mediated suppression of *FA2H* interrupted this cell cycle exit, underscoring *FA2H*'s role in this critical cellular transition. Additionally, this *FA2H* knockdown was associated with a decrease in the levels of two key cyclin-dependent kinase inhibitors, further implicating *FA2H* as a significant player in the regulation of cell cycle progression and the differentiation pathway.

Other research has bolstered the understanding of 2-OH sphingolipids' pivotal role in cell differentiation, with notable insights emerging from a study on differentiation and lipogenesis in adipocytes (Guo et al. 2010). In this context, an upsurge in *FA2H* expression was seen to coincide with the differentiation phase, a process that could be reversed by siRNA-induced *FA2H* knockdown. Moreover, *FA2H* knockdown was found to curtail basal and insulin-stimulated glucose uptake in mature adipocytes, which could suggest an accelerated endocytosis of the glucose transporter 4 (GLUT4) potentially due to increased raft lipid mobility. This phenomenon might also be influenced by a signaling mechanism directly involving 2-OH sphingolipids, a possibility that has been contemplated.

The connection between *FA2H* sphingolipids and apoptosis was initially brought to light by Kyogashima and colleagues (Kyogashima et al. 2008), demonstrating that kidney extract fractions containing 2-OH-ceramides had a more pronounced apoptotic effect on human tumor cell lines compared to those lacking 2-OH-ceramides. The effect of different C6 ceramides on the proliferation of breast cancer cells was investigated using both stereoisomers of 2-OH-C6 ceramide/dihydroceramide and their non-hydroxy counterparts (Schulz et al. 2011). Consistently, 2-OH ceramides exhibited a more substantial growth inhibitory impact, with the R stereoisomers manifesting the most pronounced effects. This line of research was extended by Kota et al. who in 2013, examined the R and S stereoisomers of C16 ceramides, closely resembling endogenous ceramides, on C6 glioma cells, uncovering similar growth inhibitory patterns (Kota et al. 2013). In the CNS, 60% of the fatty acids present in myelin galactolipids are hydroxylated at the C2 position (*FA2H*) (Maldonado et al. 2008). This concentration of 2-hydroxy fatty acids is not observed in other mammalian tissues, indicating a critical function for the 2-hydroxyl modification in sustaining myelin integrity. However, the precise mechanism by which *FA2H* is downregulated in the CNS, particularly within oligodendrocyte cells, remains poorly understood.

1.2.2 FA2H-KO animal model

In the quest to understand FA2H's role more profoundly, Zöller et al. (Zöller et al. 2008) were at the forefront, developing the inaugural knockout (KO) *FA2H*^{-/-} mice model deficient in *FA2H* gene across all tissues. Notably, these mice lacked 2-OH sphingolipids within their CNS and PNS, yet there was no observed impact on oligodendrocyte maturation or myelin architecture. Moreover, nerve conduction velocities remained within normal ranges for up to five months of age. However, at the advanced age of 18 months, these animals began to exhibit signs of axonal and myelin sheath deterioration, specifically within the spinal cord and sciatic nerves. By the age of 22 months, symptoms evolved into progressive hind limb paralysis alongside a pattern of demyelination. These observations led researchers to conclude that while 2-OH sphingolipids might not be essential for myelin's initial formation, they seem indispensable for its long-term integrity and preservation. Additionally, the mice presented with unique dermatological symptoms, including sebocyte hyperproliferation, sebaceous gland enlargement, altered serum lipid profiles, and periodic hair loss (Zöller et al. 2008). These findings are particularly compelling as they indicate, despite the absence of *FA2H* gene, that 2-OH sphingolipids are still present in the epidermis, hinting at the possible existence of an alternate fatty acid hydroxylase pathway or enzyme (Maldonado et. al. 2007).

In a remarkable finding, even in the absence of *FA2H*, the presence of 2-hydroxy sphingolipids was still detected within the epidermal layers of the animals. This observation implies the potential activity of an alternative enzyme capable of 2-hydroxylating fatty acids. Potter et al. have developed a novel mouse model that can specifically deplete *FA2H* in the myelin-producing cells of the central nervous system (CNS). This was achieved by using the *FA2H*^{flx/flx} Cnp1-Cre mouse line (Potter et. al. 2011). This approach, leveraging the precision of the Cre-lox recombination method, allowed for the targeted ablation of *FA2H* in myelinating oligodendrocytes and Schwann cells, resulting in a comprehensive *FA2H*^{-/-} phenotype. When 12-month-old *FA2H*^{flx/flx} Cnp1-Cre mice from both the targeted and global KO models were examined, marked CNS demyelination and axonal degeneration were observed, with peripheral nervous system (PNS) anomalies being notably less pronounced. The synthesis of these findings with previous mouse model research illuminates a trend where CNS abnormalities appear to precede those in the PNS. The models also unveiled previously unreported signs of cerebral impairment, as substantial motor and cognitive deficits became apparent. As this symptom was not reported or analyzed in previous models, it is unclear whether this finding is present in other models as well. Intriguingly, spatial learning and memory assessment revealed

that only the mice with a total lack of *FA2H* exhibited deficits, suggesting that *FA2H* expression in cell types beyond OLs might be implicated in cognitive integrity (Potter et al. 2011).

The Mouse Model of Spastic Paraplegia SPG35 (*FA2H*^{-/-} mice, Fa2htm1Meck; MGI:3829000) (Jordans et al., 2022) was generated and genotyped as described by Zöller et al. (2008). This model focuses on investigating the myelin sheath, with a preliminary focus on Schmidt-Lanterman incisures (SLIs), also known as myelin incisures or Schmidt-Lanterman clefts. SLIs are cytoplasmic channels of Schwann cells in the myelin internodes. Myelin was isolated from the sciatic nerves of *FA2H*^{-/-} and *FA2H*^{+/+} mice aged 6, 13, and 17 months. Western blot analysis of GalC, MBP, and CNP showed normal expression in young *FA2H*^{-/-} mice (6 and 13 months) but reduced expression in 17-month-old *FA2H*^{-/-} mice. Proteome analysis results suggest a potential increase in the number of SLIs. However, other proteins known to be present in SLIs and identified in our mass spectrometry screen were not increased in *FA2H*^{-/-} mice. Furthermore, Western blot analysis revealed no significant changes in L-MAG levels, which is also abundant in SLIs. The study also quantified SLIs in teased fibers of sciatic nerves using fluorescently labeled phalloidin. The number of SLIs significantly increased in 17-month-old mice but not in younger mice. Given that the paranodal structure is disturbed in mice lacking sulfatide, the group investigated whether the absence of 2-hydroxylated sulfatide affects paranodes in older mice. Jordans et al. measured the length of nodes of Ranvier and paranodes in 17-month-old mice using Caspr as a paranodal marker. They observed differences in node length between genotypes, but these differences were not significant. This observation suggests that the presence of 2-OH sphingolipids in cells other than OLs is essential for memory and learning (Jordans et al., 2022).

The most recent animal model to study FAHN was developed in *Drosophila melanogaster* by Mandik and colleagues (Mandik F. et al. 2022). The research group generated a compound heterozygous line *dfa2h1/dfa2h2* model and focused on the cellular mechanisms in FAHN, in particular the observed behavioural abnormalities, which included motor and flight impairment as well as shortened lifespan. They also investigated changes in mitochondrial dynamics and autophagy. The phenotypic and disease progression results of these studies were found to be very similar to other animal models. One-week-old *dfa2h1/dfa2h2* model flies exhibited a number of movement disorders such as tremor, uncoordinated flight and reduced activity. As the model flies aged to three weeks, the observed movement disorders progressively worsened. By studying autophagy and mitophagy, the group discovered mitochondrial dysfunction and

altered autophagy, characterised by the accumulation of autolysosomes and increased levels of the autophagy marker LC3B (Mandik F. et al. 2022).

1.2.3 FA2H in Human Diseases

The *FA2H* deficiency results in a human disease called FAHN or HSP35 or SPG35 (Edvardson, S. et al., 2008; Dick et al., 2010). Typical clinical signs of FAHN include spasticity of the lower limbs, ataxia, cognitive issues, and leukodystrophy (Gregory, A. et al., 2011). FAHN is classified under a group of diseases known as NBIA (Kruer et al., 2010). Iron deposits in the basal ganglia causing lesions in the globus pallidus ("eye-of-the-tiger sign") are common in these diseases. Over 106 different mutations in the human *FA2H* gene causing FAHN/SPG35 have been documented (Edvardson, S. et al., 2008; Dick et al., 2010; Kruer et al., 2010; Pierson, T.M.; et al., 2012; Pensato, V. et al., 2014; Donkervoort, S. et al., 2014; Zaki, M.S. et al., 2015; Kara, E. et al., 2015; Soehn, A.S.; et al., 2016; Bekta, s, G. et al., 2017; Travaglini, L. et al., 2018; Bengner, M. et al., 2019; Landouré, G. et al., 2029; Rattay, T.W et al., 2019; Tsang, M.H.Y. et al., 2020). Transgenic mouse lines with either total or conditional *FA2H* knockout have been developed, serving as animal models of FAHN (Potter et al., 2011; Maier H et al., 2011). Studies on these mice revealed that the synthesis of 2hFA-SL in myelinating cells is crucial for maintaining the myelin sheath, though not for its formation (Potter et al., 2011; Maier H et al., 2011). The phenotypes of both the total and oligodendrocyte-specific *FA2H* knockout were similar and resembled human disease symptoms (Potter et al., 2011; Maier H et al., 2011) suggesting that most symptoms result from *FA2H* deficiency in myelinating glia. However, the oligodendrocyte-specific knockout did not show learning and memory deficits observed in the total knockout (Maier H et al., 2011), indicating low *FA2H* expression in other brain cell types. This implies that cognitive impairment in FAHN might result from the loss of *FA2H* activity in neurons. Nevertheless, most FAHN-related symptoms in the mouse models are due to FA2H loss in oligodendrocytes, raising the question of how changes in myelin lipid composition lead to axonal degeneration. Proteome analysis of myelin from *FA2H*^{-/-} mice revealed a specific accumulation of a major myelin protein, Opalin, in compact myelin (Hardt R. et al., 2021). This supports the role of 2hFA-SL in apical membrane sorting, as previously discussed. Altered trafficking or accumulation of myelin membrane proteins could link altered myelin lipids to axonal pathology. FAHN, as part of the NBIA group, shows iron accumulation in the basal ganglia (Meyer E et al., 2015), observed in most FAHN patients (Ratty T.W. et al., 2019). However, the mechanism by which *FA2H* deficiency leads to brain iron accumulation remains unclear. Cultured fibroblasts from FAHN and other NBIA cases exposed to high iron showed a stronger

intracellular iron increase than control fibroblasts, possibly due to reduced lysosomal degradation and increased recycling of the transferrin receptor (Drecourt, A. et al., 2018). While FAHN is characterized by upper motor neuron axon degeneration in the CNS, peripheral neuropathy has been noted in some FAHN patients (Pierson, T.M et al., 2012; Ratty T.W. et al., 2019; Axpe, I.R et al., 2017). A similar late-onset peripheral neuropathy was observed in older *FA2H*^{-/-} mice (Potter et al., 2011). Proteome analysis of peripheral myelin identified elevated levels of a membrane complex containing the adhesion molecule CADM4, localized in Schmidt–Lanterman incisures (Jordans S., et al., 2022). This suggests that 2hFA-galactosylceramide or 2hFA-sulfatide may be involved in CADM4 trafficking or turnover, though further studies are needed to confirm this.

1.3 Oligodendrocyte development

During mid-gestation in humans and just before delivery in rodents, the initial formation of oligodendrocytes (OLs) begins in the cervical spinal cord (Fu et al. 2002; Lai et al. 2016). This occurs in the motor neuron progenitor domain (pMN) of the ventral spinal cord, influenced by sonic hedgehog (SHH) and bone morphogenetic protein (BMP) from the ventral and dorsal sides, respectively (S.K. Lee et al. 2005; Andrew M. Ravanelli, 2015). OLs primarily proliferate in the ventral spinal cord, with some proliferation also in the dorsal part. The pMN region is marked by OLIG2 expression, essential for developing motor neurons and OLs. The maturation of OLs progresses through six stages: pre-oligodendrocyte progenitor (preOPC), oligodendrocyte progenitor (OPC), pre-oligodendrocyte, immature oligodendrocyte, mature oligodendrocyte, and finally myelinating oligodendrocyte, which forms myelin sheaths around neuronal axons. Proteins necessary for myelin formation are activated during OL maturation, though initially in small amounts. The *FA2H* gene, crucial in this process, is primarily found in OLs but is expressed at low levels. In myelinating OLs and Schwann cells, the enzyme UDP-galactose: ceramide galactosyltransferase (CGT) produces GalCer with 2-hydroxy and non-hydroxy fatty acids (Hama et al. 2010).

OLIG2 and *SOX10* are key transcriptional regulators in the OLs lineage, consistently expressed throughout OLs development (Abney et al. 1983; Raff et al. 1979). Early OPCs are dynamic, dividing and migrating, characterized by *SOX10* and *OLIG2* expression, and surface markers like *NG2*, *PDGFR α* , and *A2B5*. However, during oligodendroglial differentiation, genes like *MAG*, *MYRF*, *FA2H*, *MBOAT1*, *LSS*, and *HSD17B7* have reduced expression during the OPC migratory phase (M. Wedel et al. 2020). As OPCs finish migrating, they divide and become more complex, entering the pre-oligodendrocyte phase, marked by O4 gene expression (Bansal

and Pfeiffer, 1989). In the immature OL phase, cell division stops, and the cells develop a complex branched structure, expressing GalCer, 2',3'-cyclic nucleotide 3'-phosphodiesterase (CNP), MAG, and APC proteins (Lu O. Sun et al. 2018; Meireles et al. 2018). FA2H, found in the ER of OLs in the CNS and Schwann cells in the PNS, works with ceramide CGT to synthesize GalCe (Eckhardt et al. 2005). FA2H hydroxylates free fatty acids during ceramide synthesis, a crucial step demonstrated by Anderson et al (Anderson et al. 2009). In the subsequent phase of myelination, there is a marked simplification of cellular morphology. It is important to note that during the migration of lipids and proteins to the myelin extensions of myelinating OLs, FA2H is highly expressed and plays a crucial role (Kota et al. 2014). During OL maturation, key myelin proteins like MBP, PLP, MAG, and myelin oligodendrocyte glycoprotein (MOG) are expressed. FA2H plays a significant role in lipid migration to myelin extensions and influences membrane protein turnover by affecting lipid mobility in membrane subdomains (Lin Guo et al. 2012). The differentiation process and expression of the transcription factors required for the differentiation and maturation of oligodendrocyte is described in Figure 3, B. The balance between OLIG2 and NGN2 orchestrates the timing of the shift towards gliogenesis. OPCs expressing PDGFR α mature into premyelinating oligodendrocytes, marked by the expression of O4 and SOX10. The progression of these oligodendrocytes is characterised by the presence of PLP, MBP, and MAG.

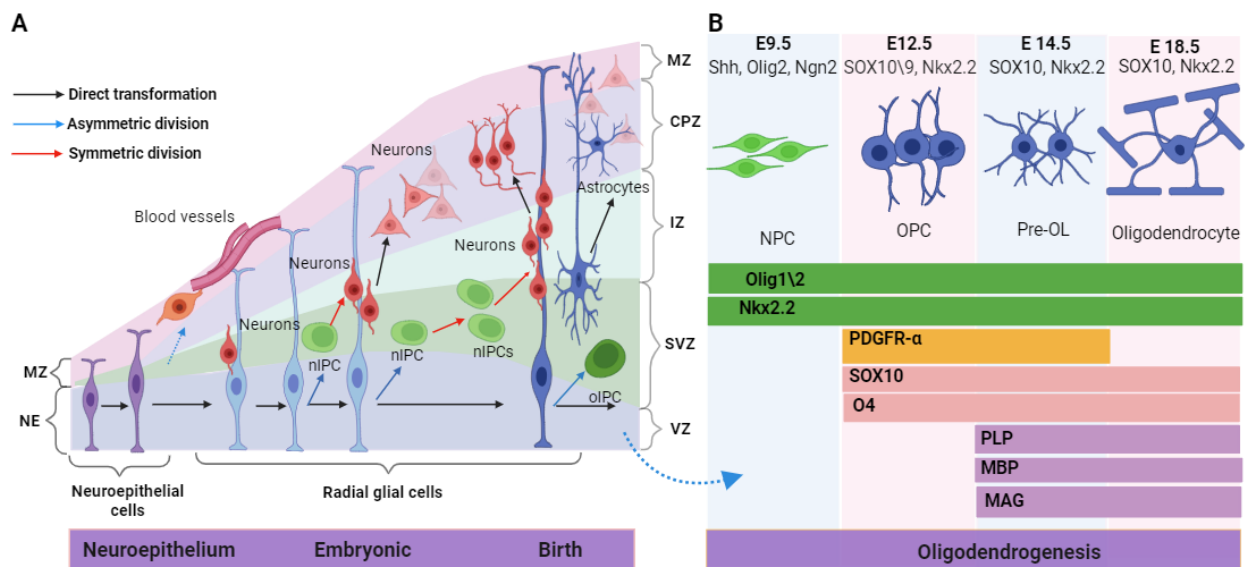


Figure 3: Neurogenesis and oligodendrogenesis processes from neuroectodermal tube development. A, the process of neurogenesis in the development of the cortex involves several key areas: CP (cortical plate), IZ (intermediate zone), MZ (marginal zone), with cells like nIPC (neurogenic intermediate progenitor cell), oIPC (oligodendrocyte-producing intermediate progenitor cell), RG (radial glia), SVZ (subventricular zone), and VZ (ventricular zone) playing vital roles. B, the balance between OLIG2 and NGN2 regulates the timing of the shift towards gliogenesis. OPCs expressing PDGFR α mature into premyelinating oligodendrocytes, which are marked by the expression of O4 and

SOX10. The progression of these oligodendrocytes is characterized by the presence of PLP, MBP, and MAG. This summary is based on visuals created with Bio render.

1.3.1 Myelin formation and function

Previous research has indicated that *FA2H* is highly expressed in the human brain and becomes upregulated during the myelination process in the mouse brain ((Zoller et al. 2008; Krueger et al. 2010; Potter et al. 2011). *FA2H* plays a pivotal enzymatic role, catalysing the 2-hydroxylation of free fatty acids, thereby providing the essential precursors for the synthesis of myelin 2-hydroxy galactolipids (Alderson et al. 2005; Eckhardt et al. 2005; Y. Uchida et al. 2007; Hama et al. 2008). Oligodendrocytes are unique in their ability to insulate numerous axons of varying widths, creating a range of lengths and thicknesses of myelin layers for each individual cell. Notably, the distribution of myelin lengths is meticulously orchestrated along each axon, indicative of a targeted regulatory mechanism governing the size of each myelin section. The strategic regulation of myelin layer dimensions over specific axons is believed to be integral to the regulation of nerve signal speeds (Waxman and Simons, et al. 1984). The creation of myelin involves a series of steps that encompass the growth of OLs tendrils, contacting axons, the organization of membrane proteins, consolidation, and the formation of myelin segments (Simons and Nave, et al. 2015). Neuregulin 1 (*NRG1*) within the CNS is recognized for its role in sustaining the survival of newly specialized OLs, though its exact contribution to myelin creation is yet to be fully elucidated (Fernandez et al. 2000; Brinkmann et al. 2008; Bechler et al. 2015; Redmond et al. 2016). The pathway involving integrin interactions with laminin-2 is also shown to be critical in controlling the number of OLs and is essential for myelin development in experimental conditions, with its absence linked to the loss of myelin (Brinkmann et al. 2008). Although some researchers have proposed that *FA2H* may influence the levels of other proteins within lipid rafts that regulate mobility (Maldonado et al. 2007), which is critical for myelin formation, the significant question of how diminished *FA2H* expression during OLs differentiation impacts myelin formation in FAHN disorders remains unanswered. Recently, Jordans et al. demonstrated that *FA2H*-dependent synthesis of 2-hydroxy ceramide/GlcCer is essential for the correct formation and secretion of lipid lamellar bodies in differentiating human keratinocytes (Jordans et al. 2022). This study also introduced the compelling possibility that 2-hydroxy lipids significantly affect cell migration, potentially due to their role in altering membrane fluidity or influencing the organisation of lipids and proteins within sphingolipid- and cholesterol-rich microdomains, or lipid rafts. Lipid rafts play a crucial role in neural development (Maldonado et al. 2007). Many myelin proteins involved

in cell signalling and adhesion are associated with these rafts. Moreover, the expression of PLP is regulated by the presence of GalCer, indicating a pivotal role for myelin galactolipids in the organisation of myelin proteins within lipid rafts (Jordans et al. 2022). This suggests that 2-hydroxy lipids may influence the composition of lipid rafts, thereby regulating the adhesion and migratory properties of OLs. Conversely, in the mouse model, the presence of 2-hydroxy fatty acids in the GlcCer of myelin from *FA2H*^{-/-} mice suggests a specific requirement for monoglycosylceramides with both non-hydroxy and 2-hydroxy fatty acids for optimal myelin function and stability (Jordans et al. 2022). Research on *FA2H* deficiency to date has shown that instability and the formation of compact myelin membranes are common neuropathological features in FAHN (Hama et al. 2010; Potter et al. 2011; Kruer et al. 2010; Lin Guo et al. 2012). In order to elucidate the diversity of myelin proteins, the current study will focus on the expression of myelin proteins and their colocalization in FAHN patient-specific iPSC-derived OLs and coculture.

1.3.2 Myelin composition and wrapping

It appears that OLs extensions initially surround the axons in a preliminary encircling action. The ensuing development of the myelin's outermost layers has been observed to correlate with the bilateral expansion of the axon's circumference, which is propelled by actin polymerization at the forefront of the OLs extension (Snidero et al. 2014). This progressive encasement involves the unwinding of the actin filaments and the simultaneous stretching of the myelin membrane, leading to a gradual decrease in the thickness of the myelin towards the more distal sections of the elongating sheaths (Refer to Figure 4).

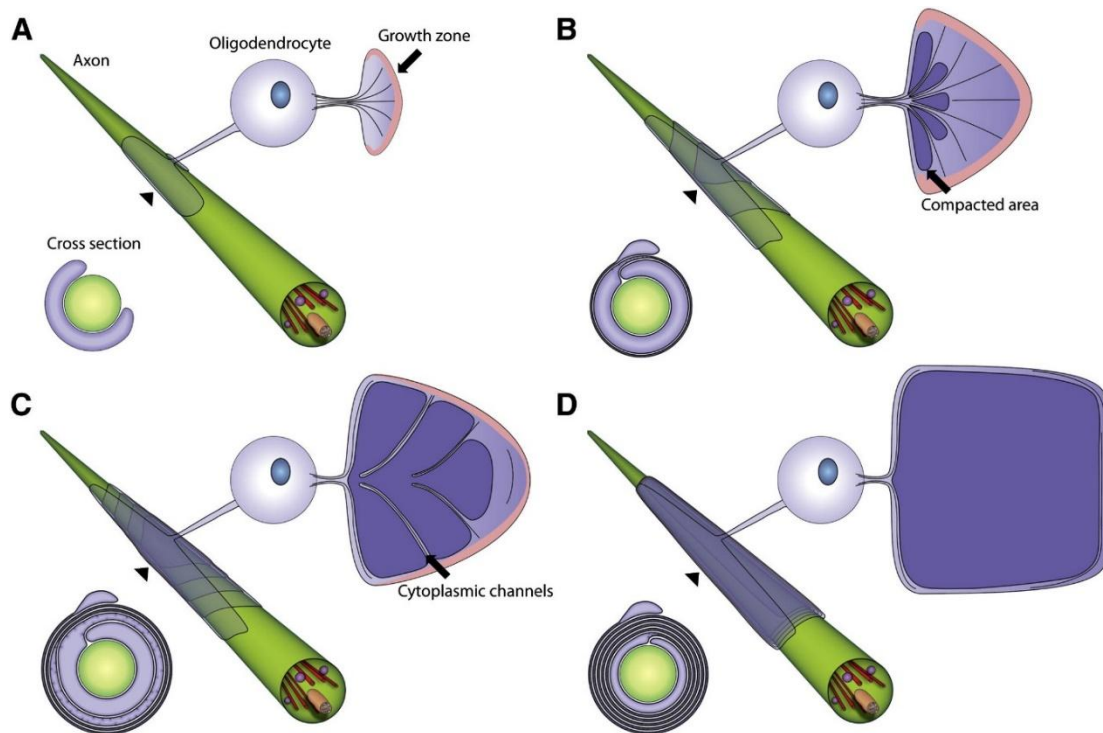


Figure 4: Myelin wrapping and compaction (A–D) Model illustrating the formation of a developing myelin sheath from various perspectives, including unwrapped, wrapped, and cross-sectional views. The unwrapped depiction highlights the structural intricacies and the emergence of cytoplasmic channels connecting the cell body to the growth zone within the inner tongue, with the growth zone distinguished in pink and the compacted myelin in dark violet. The wrapped representation provides insight into the layering position as it envelops the axon. Cross-sectional views offer a glimpse into the compaction process at different stages of myelin growth. Adopted from Nicolas Snaidero et al. 2014

The myelin sheath possesses a unique biochemical signature that sets it apart from the plasma membrane of the oligodendrocyte's cell body, and it is differentiated into regions of dense compaction and less dense non-compaction (Krämer et al. 2001). Analyzing the dry weight composition of myelin reveals that it is largely lipid-based, accounting for 70% of its makeup, with a significant presence of GalCer and cerebroside. Within the protein fraction, which constitutes the remaining 30%, two proteins, PLP and MBP, collectively represent 80% of this protein mass (Krämer et al. 2001). The targeted placement of elements like the CNP, MAG, and MOG, among others such as CLAUDIN-11 at junctures of dense and less dense myelin areas, is essential for the ordered production, selection, and movement of myelin elements.

Various routes have been implicated in the handling of the myelin membrane, which includes directed movement, the process of vesicles carrying new myelin merging with the existing myelin, and myelin assembly through interactions of lipids and proteins and transport by cytoplasmic adaptor proteins (Snidero et al. 2014; Krämer et al. 2001). The transport of PLP seems to be heavily reliant on myelin rafts (Simons et al. 2000). In contrast, *MBP* is localized

at the cell edges after *MBP* mRNA moves to myelin growth areas through microtubule-associated units. This indicates the possibility of myelin growth being managed on a localized scale. MBP, when newly formed and associated with active neuronal axon in experimental settings, shows an increase in the production of its mature form (Wake, Lee & Fields, 2011). MBP is a charged molecule that interacts with cell membranes without repelling negatively charged molecules. This interaction prompts a change in shape that leads to structured α -helices and β -sheets (Agrawal et al. 2011). In the process of myelin compaction, MBP is proposed to counter the negative charges on adjacent membranes, resulting in a 'zipper' mechanism that joins the myelin layers. This is observed in variations in myelin compaction in experimental models like *CNP*^{+/-} and *MBP*^{+/-} mice, demonstrating different timing in the compaction within the cell (Snidero & Simons, 2017). In aged *FA2H*^{-/-} mice lacking the enzyme that synthesises galactolipids, but which could produce myelin sheaths, a reduction in the expression of MBP in isolated myelin sheaths was observed (Silvia Jordans et al., 2022). Furthermore, the aforementioned research article indicated that myelin instability is observed, which led to the hypothesis that reduced MBP expression can cause impaired myelin membrane layer scaffolding, which in turn leads to instability of the myelin sheath and further to noncompact myelin (Silvia Jordans et al., 2022). Further analysis of these mice revealed that GalCer and sulfatide play a crucial role in the expression of MBP and PLP during myelination and axo-glial organization. The myelin of *CGT*-knockout mice is devoid of GalCer and sulfatide, and instead contains GlcCer, which is not found in normal myelin (M. Meixner et al. 2011). It is of significant importance to highlight that *FA2H* activity increases in the CNS during developmental myelination, providing precursors for the synthesis of myelin 2-hydroxy galactolipids. With regard to the function of FA2H, the protein was found to have increased activity in the early postnatal period and to play an important role in the myelinating process (M. Meixner et al. 2011; Silvia Jordans et al., 2022). However, the mechanism underlying this process in FAHN is not yet fully elucidated. Disrupted interactions between the protein and other components of the myelin sheath result in defects in the stability of the myelin intermembrane and the entire myelin sheath. It is hypothesised that impaired axonal myelination represents a pivotal pathological event in FAHN. Nevertheless, the precise mechanisms by which defects in myelination cause neurodegeneration remain under debate.

1.3.3 Protection of axon

Myelin serves as a protective sheath encasing the axon, delivering metabolic support, and enhancing the speed of axonal transmission without an increase in axon diameter. In

demyelinating diseases like FAHN and multiple sclerosis (MS) (Kruer et al. 2010; Bö et al. 1994), the absence of myelin renders the axon susceptible to damage. In MS, there is an upsurge in nitric oxide synthase enzyme activity at the demyelination site (Bö et al. 1994). Nitric oxide influences mitochondrial metabolism and adenosine triphosphate (ATP) synthesis; ATP, in turn, is indispensable for maintaining sodium-potassium homeostasis in the axon. When sodium ions accumulate and cannot be efficiently expelled, the calcium-sodium exchanger operates in reverse, permitting calcium influx into the axon, thereby triggering a cascade of enzymatic reactions leading to axonal damage. In an animal model of oligodendropathy, mature OLs are selectively eliminated through the cell-specific expression of diphtheria toxin (Traka et al. 2010). Remarkably, myelinated axons persist long after the demise of the oligodendrocyte soma, suggesting the sustained functionality of glycolytic enzymes and transporters for several days until macrophages clear the myelin debris (Saab et al. 2013).

1.3.4 Node formation

The functional efficiency of myelinated axons depends on two key adaptations: the densification of the myelin sheath to reduce electrical leakage along the axon, and the establishment of specialised domains for efficient impulse transmission. These specialised domains include the node of Ranvier (NoR), paranodal axoglial junctions (PNJ), juxtaparanodal junctions (JXP) and internodal processes, refer to Figure 5 (Lubetzki, C., et al. 2020; Keiichiro Susuki et al. 2008). The elaborate architecture of these regions represents a remarkable interplay between axonal and glial elements, requiring the involvement of extracellular matrix proteins, adhesion molecules, and structural support provided by the cytoskeleton (Keiichiro Susuki 2013, I. Lorena Arancibia-Cárcamo et al. 2014). Figure 5 shows a cross-section of a myelinated axon illustrating this specialised architecture, adapted from the work of Lubetzki, C., et al. 2020.

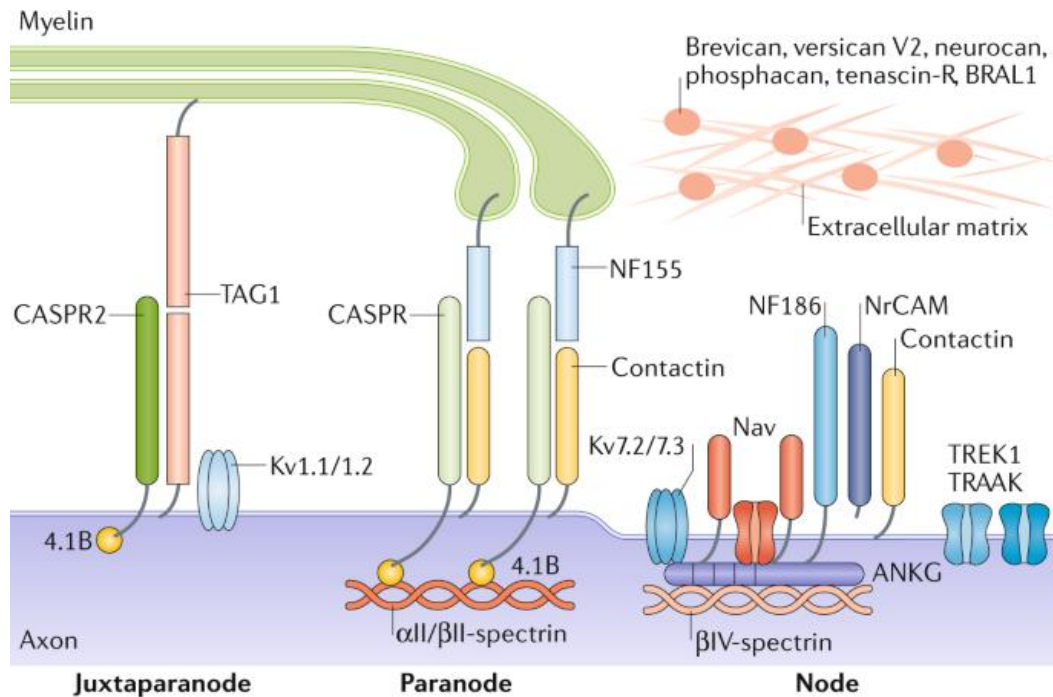


Figure 5: Organisation and molecular composition of myelinated axon sub-domains. The molecular layout of myelinated axon sub-domains, including the Ranvier Node, paranodal, and juxtaparanodal areas, is crucial for axonal functionality. At the heart of this configuration is the nodal complex, comprising voltage-gated sodium (Nav) channels and cell adhesion molecules, vital for the node's operation. Structural integrity of this complex is ensured through its anchorage to the cytoskeleton and its interaction with extracellular matrix proteins. The nodal area is also characterized by the inclusion of voltage-gated potassium channels Kv7.1 and Kv7.2. Flanking the nodal domain, the paranodal axoglial junction acts as a pivotal diffusion barrier, crucial for distinguishing the nodal from the juxtaparanodal domain. This separation is key to their distinct functionalities. Within the juxtaparanodal zone, there is a significant aggregation of potassium channels, with a particular emphasis on Kv channels. Adopted from Lubetzki, C., et al. 2020.

Ranvier nodes are comprised of a complex assortment of channels responsive to voltage changes, primarily sodium channels, which are integral for the transit of ions across the neural membrane. Alongside potassium channels, these components are critical in the modulation of nerve impulse propagation (Lubetzki, C., et al. 2020). Furthermore, the node of Ranvier is fortified with various scaffold proteins, indispensable for both its formation and ongoing structural integrity (I. Lorena Arancibia-Cárcamo et al. 2014; Yanqing Zhang et al. 2012; Rasband & Peles, 2015; Jose C Rios et al. 2020).

In close proximity to the node of Ranvier lies the PNJ, which fastens the myelin terminus to the axonal membrane through highly specialized contact regions resembling septa. The PNJ delineates a boundary that is instrumental in constraining the electrical impulses within the node of Ranvier, thus impeding the diffuse spread of axonal membrane proteins. Within the JXP region, a concentration of Kv1 potassium channels exists, believed to serve in the capacity of

potassium ion rectifiers that stabilize the resting membrane potential across the internodal length (Lubetzki, C., et al. 2020). The internodal sections are marked by a dense packing of myelin, discernible in cross-sectional views. The PNJ stands as a specialized junction between the axonal membrane and the terminal loops of the myelin lamellae. The extensive septate-like junctions present at these locations form the largest known cell-to-cell junctions within the vertebrate system (Jose C Rios et al. 2020). Galactosylceramides and sulfatides have important functions in the differentiation of oligodendrocytes and the establishment of stable paranodal junctions at the node of Ranvier (Uchida Y. et al., 2007, Uhlén, M. et al., 2015; Baba H. et al., 2019; Grasso S. et al., 2016; Suzuki M. et al., 2022). These are, however, apparently normal in *FA2H*^{-/-} mice. Thus, sulfatides and galactosylceramides do not have to be 2-hydroxylated to fulfill these functions or until now it's not known.

1.3.5 Demyelination in neurodegenerative disorders

Demyelination is a process that can disrupt vital processes when intact myelin is damaged by physical, chemical or biological insults (B. Etle et al. 2016). Injuries to the brain often precipitate OLs demise and subsequent loss of neurons. In contrast, inflammatory conditions can incrementally erode myelin, which may cause considerable neurological and cognitive impairments that worsen progressively. In both CNS and PNS, FA2H contents in galactolipids are very low at the onset of myelination and increase rapidly during developmental myelination. Recent studies have delved into myelin's involvement in neurodegenerative conditions, a topic that has garnered research interest (G. E. Parrilla et al. 2023). Comprehending the interactions between myelin and various neurodegenerative conditions whether it manages, aggravates, or contributes to them is a question that remains largely unresolved (S. Ravera et al. 2015; G. E. Parrilla et al. 2023).

FAHN as a neurodegenerative disorder that is impacted by demyelination in both the CNS and the PNS (Alderson et.al. 2005; Eckhardt et. al. 2005; Y. Uchida et. al. 2007; Hamaet al. 2008; Kruer et al. 2010; Potter et. al. 2011; Garone et al. 2011; Tonelli et al. 2012; Cao et al. 2013; Rupps et al. 2013; Donkervoort et al. 2014; Hashemi et al. 2023; German et al. 2023; Lidangzhi Mo et al. 2024). Research utilising a range of animal models has demonstrated that disturbances in myelin structure, along with demyelination, and are associated with either a partial or complete absence of the *FA2H* gene. Although HFA-sphingolipids appear to be non-essential for the formation of compact myelin, they are crucial for its long-term maintenance and may also support glial-dependent axonal functions (Alderson et.al. 2009; Kruer et. al. 2010; Potter et. al. 2011). In *FA2H*^{-/-} mice lacking GalCer, myelin is initially formed but

remains unstable, indicating a potential role for GalCer in sustaining myelin integrity observed in CNS (Potter et al. 2011). Further observations from the same study showed that *FA2H*^{-/-} mice developed thicker or swallowed myelin sheaths. The reason for the thicker myelin sheath in this mouse model is unclear. Notably, analyses by Zoller and colleagues in the PNS of *FA2H*^{-/-} mice at an older age (18 or 22 months) revealed demyelination processes associated with reduced sphingolipid expression, particularly of GalCer and sphingomyelin, and the appearance of unmyelinated axons, but didn't observe myelin thickness (Zoller et al. 2010). The instability of myelin structure and progressive demyelination, including symptoms such as hind limb paralysis, observed in both mice models, highlight the importance of the fatty acid composition of galactolipids for myelin stability in CNS and as well in PNS (Kruer et al. 2010).

1.4 Autophagy impairments and neurodegeneration

Autophagy is an extensively studied cellular process responsible for the degradation of cellular structures, including entire organelles, with the subsequent recycling of their components for the synthesis of new proteins and membranes (Tsuboi, Noda, and Ohsumi, 1992; Takeshige, Baba, and Ohsumi, 1994). This crucial mechanism ensures the turnover of misfolded, dysfunctional or 'aged' proteins and organelles and plays a key role in maintaining the abundance of functional proteins. The coordinated three-step process of autophagy involves the formation and elongation of a phagophore that engulfs organelles and cytosolic cargo before fusing with a lysosome for cargo degradation (Jaber, Zong et al. 2013; Xie, Klionsky et al. 2007). The conjugation of LC3, a ubiquitin-like protein, to phosphatidylethanolamine (PE) is a crucial step in autophagosome membrane growth, effectively anchoring LC3 to the autophagic vesicles. This lipidation process, which involves Atg7 and Atg3, is essential for the expansion and closure of the autophagosome (Fujita et al. 2008; Backer et al. 2008). The fully formed autophagosome, known as an autophagosome, captures and isolates cellular waste. The conversion of the LC3 precursor (Pro-LC3) to the cytosolic LC3-I and then to the autophagosome-associated LC3-II is catalysed by ATG7 and ATG3, leading to autophagosome expansion, (Kabeya et al. 2000). LC3-II plays a pivotal role by interacting with p62/SQSTM1, a protein that acts as a link between LC3 and ubiquitinated substrates, (Kocaturk et al. 2018; Glick, Barth, and Macleod et al. 2010), which regulates material uptake into the autophagosome through its interaction with LC3-BII (Pankiv et al. 2007). Once the cargo is fully engulfed, the phagophore, now called an autophagosome, closes. A defined amount of LC3BII is then removed from the membrane by ATG4B, recycled to LC3BI and released from the

autophagosome (Simonsen et al. 2009). Finally, the autophagosome fuses with lysosomes, where the low pH and internal proteases lead to degradation of the autophagosome cargo.

1.4.1 Autophagy in the neurodegenerative disease FAHN

The disruption of protein homeostasis and the aggregation of misfolded proteins are hallmark features of neurodegenerative conditions (Kumar et al. 2016). Given the crucial role of autophagy in the clearance of proteins, its dysfunction is often observed in neurodegenerative diseases. This dysfunction is particularly pronounced in tauopathies, which encompass Alzheimer's disease (AD), Parkinson's disease (PD), Huntington's disease (HD) (Guo et al. 2017; Hyungsun Park et al. 2020), and Creutzfeldt-Jakob/Prion diseases, with studies by Lee et al. in 2012 highlighting the resistance of aggregated proteins to autophagic degradation (Lee et al. 2012). These aggregates have cytotoxic effects that can disrupt cellular function (Bucciantini et al. 2002). Furthermore, models of autophagy impairment typically display neurodegenerative phenotypes, whereas enhanced autophagic processes are generally associated with neuroprotective outcomes, (Rubinsztein et al. 2011). Neurons, which are long-lived and contain complex structures such as synapses, rely heavily on autophagy for the clearance of proteins synthesized in the soma, which can accumulate and exert toxic effects if not efficiently degraded. The significance of autophagy in neurons has a critical role in neuronal health and function (Wang and Heisinger et al. 2012). Autophagy and mitochondrial dysregulation is evident in several types of NBIA (Arber et al. 2017) However, the autophagy processes and mitochondrial defects in FAHN are not well researched. Recently, Mandik and colleagues conducted autophagy investigations on *Drosophila* and FAHN patient fibroblasts. In a *Drosophila* model of FAHN, they observed that alterations in mitochondrial fission and fusion disrupted the mitochondrial network. This disruption was accompanied by increased levels of the autophagy marker LC3 and its activated, lipidated form LC3-II—similar observations were noted in FAHN patient fibroblasts (Mandik F. et al. 2022). In the same report, they highlighted that, besides the cytotoxic effects of protein aggregates, the requirement for functional proteins and organelles leads to disturbances in the cellular processes of FAHN. They further indicated that the severity of imbalanced proteostasis can significantly disrupt cellular functions. Autophagy is a central process that ensures a continuous supply of functional organelles and proteins. In the same study, it was found that the defect in autophagy in FAHN is characterized by a pronounced iron accumulation in the basal ganglia (Mandik F. et al. 2022). However, the mechanisms underlying how *FA2H* deficiency leads to iron accumulation in the brain remain unclear. It has been observed that fibroblasts from FAHN and other NBIA cases, when cultured

in the presence of high iron levels, show a more pronounced increase in intracellular iron compared to control fibroblasts (Mandik F. et al. 2022). However, the connection between this phenomenon and impaired autophagy machinery in FAHN remains unclear. This phenomenon is postulated to result from reduced lysosomal degradation and increased recycling of the transferrin receptor.

1.5 Human iPS cells as disease models

The history of deploying experimental models for disease stretches back to the 18th and 19th centuries, highlighted by Louis Pasteur's significant contributions. In the late 1800s, Pasteur demonstrated the germ theory of disease by exposing sheep to anthrax (Hau and Schapiro 2010). Contemporary animal models employed in medical research span a variety of species, such as rodents, zebrafish, fruit flies, and nematodes. These models offer a close approximation of the human physiological response throughout the development of specific illnesses. The application of such animal models is supported by the preservation of genetic material between species over the course of evolution (Hunter et al. 2008). The benefits of animal models are numerous, offering controllable sizes for easy handling, as well as prolific breeding capacities for research scalability (Barut and Zon et al. 2000; Robert L. Perlman et al. 2016). Models like the nematode and fruit fly, with their fully sequenced genomes, facilitate the simplification of genetic manipulation. Importantly, studying diseases within the *in vivo* setting of these organisms allows for the examination of both cell-autonomous and systemic factors influencing diseases (Merkle and Eggan et al. 2013). Various animal models have been created for FAHN disease, with mouse models that have compound heterozygous mutations being among the most utilized. These include also *Drosophila* models engineered with either a mutated or knockout *FA2H* gene that retains some functional capability, resulting in a less severe phenotype.

Nevertheless, there are intrinsic limitations within animal models. A significant shortcoming is their inability to fully represent the complexity of human diseases or biological processes (Barut and Zon et al. 2000). Even though species such as mice share close genetic ties with humans, the substantial differences in their genetic constitution present considerable challenges in directly translating findings from animal contexts to human applications. The translation of successful results from mouse studies to human trials has often been elusive (Merkle and Eggan et al. 2013). Mice possess a genetic variability that is not completely reflective of the vast genetic diversity found among humans. Moreover, a thorough analysis of the genome of the animals used in studies is crucial to ascertain whether the observed effects are exclusively due to the experimental conditions or if other variables play a role (Benavides and Guénet et al.

2001). Although animal models are instrumental for observing symptoms, they may fall short in accurately modeling the progression of internal dysfunctions, such as neuronal anomalies inherent to neurodegenerative diseases (Merkle and Eggan et al. 2013).

To bridge these gaps, a more fitting model that better represents the internal environment of human development and facilitates the observation of disease progression is the human pluripotent stem cell (hPSCs) model. These pluripotent cells, with their potential to morph into any cell type, present a valuable and ethically sound resource for laboratory culture. Their differentiation into specialized cells or tissues enables their use in diverse applications, such as disease simulation, regenerative therapies, and the screening of potential new medications for both effectiveness and safety (Ebert et al. 2012). In contrast to traditional models, hPSCs exhibit robust and extensive growth, enabling comprehensive genetic and chemical assessments (Merkle Eggan et a. 2013). This feature permits the swift observation of results. These *in vitro* models permit the exploration of genotype-phenotype correlations in a controlled environment, offering critical insights.

hPSCs are crafted by reprogramming mature somatic cells to revert to a state akin to embryonic stem cells (Takahashi and Yamanaka 2006). Yamanaka initially pioneered this reprogramming method with mouse fibroblasts in 2006 and later adapted it for human skin fibroblasts, a breakthrough that led to a Nobel Prize. In this process, dermal fibroblasts are induced with a quartet of transcription factors - OCT3/4, SOX2, c-MYC, and KLF4 - which are fundamental in maintaining the cells in an undifferentiated and renewable state. These induced pluripotent stem cells (iPSCs) are noted for their exceptional capacity to differentiate into cell types representative of all three germ layers, both in laboratory settings and in the formation of teratomas (Takahashi et al. 2007). The versatility of iPSCs derivation extends beyond dermal fibroblasts to include reprogramming of neuronal, haematopoietic, adipose and other cell types (Ebert et al. 2012). The focus of this study is on neuronal disease models using iPSCs, a methodology first demonstrated in 2008 (Dimos et al. 2008).

In this specific study, fibroblasts from FAHN patient were reprogrammed into iPSCs and subsequently differentiated into functional neurons and OLs. The generation of iPSC-derived OLs has emerged as an appealing method for investigating both normal and aberrant OLs development in various diseases. This approach serves multiple purposes, such as acting as a valuable tool for studying oligodendrogenesis in demyelinating disorders, screening potential chemical inducers of oligodendrogenesis, and exploring its potential as a cell-based therapeutic

intervention for childhood leukodystrophies and cerebral palsy (Billon et al. 2002; Goldman & Kuypers, 2015; Goldman et al. 2012).

Initially, the derivation of OLs commenced with embryonic stem cells from mice (Fraichard et al. 1995) and was later advanced using human embryonic stem cells (Zhang et al. 2001). This process was often accompanied by a mix of diverse neuronal cell types. With advancements in protocol refinement, the efficient generation of OLs from human embryonic stem cells was achieved (Kang et al. 2005) and further honed with induced pluripotent stem cells (Wang et al. 2013; Livesey et al. 2016; Douvaras et al. 2014; Leon et al. 2020). The success of these techniques hinged on emulating the developmental signaling milieu that neuroepithelial cells encounter during their maturation into OLs in a living organism. The optimized approach incorporated initial neural induction using retinoic acid, followed by the transfection with transcription factor *SOX10*, encouraging OPCs to develop via SHH pathways and fostering their growth through the administration of PDGF α . Additionally, the protocol included the application of insulin and thyroid hormone, providing support for the complex differentiation, viability, and maturation stages of OLs development.

2 Aim

The overarching goal of this study is to establish human-derived iPSCs that are pathophysiological characterized as models for FAHN disease. This initiative involves preliminary *in vitro* disease modeling using iPSCs, which represents a crucial step towards creating and examining myelinating systems associated with FAHN. Given FAHN's status as a rare neurodegenerative disorder primarily impacting brain function, leading to demyelination and instability of the myelin sheath, this research focuses on the investigation of iPSCs-based neurally differentiated cells, particularly neurons and oligodendrocytes. The established cell line and the resultant cell types are expected to significantly enhance the understanding of yet unknown pathophysiological aspects of FAHN. Additionally, the findings from these investigations are anticipated to enrich the current knowledge regarding myelin neuropathology in FAHN and underscore the significance of the analyzed cell types. By utilizing patient-specific iPSCs, it becomes possible to examine disease-related phenotypes under pathophysiological conditions without the necessity for overexpressing or knocking down *FA2H*.

This approach sets forth the following objectives for the study:

- Generation and characterization of iPSCs derived from patient-specific fibroblasts.
- Differentiation of iPSCs into neurally differentiated cells.
- Establishment of myelinating coculture systems.
- Detailed description of the pathophysiology in the utilized FAHN cell line.
 - Analysis of the protein expression of mutated FA2H proteins.
 - Investigation of the expression and subcellular localization of principal myelin-structuring proteins in FAHN
 - Detailed analysis of myelinated axon structures.
 - Examination of autophagy processes within the models.

These objectives aim to provide a comprehensive framework for better understanding of the mechanisms underlying FAHN and potentially paving the way for novel therapeutic strategies.

3 Materials and methods

3.1 Material

3.1.1 Instruments

Table 3.1: Instrument

NAME	COMPANY
Analytical Balance — CP225D-0CE	Satorius AG, Germany
Axiovert 200M with Apotome	Carl Zeiss, Germany
Balance SBA 52	Scaltec Instruments, Germany
CASY Cell Counter and Analyzer TT+	Innovatis Technologies Inc., USA
Centrifuge	Labnet international, USA
Centrifuge 5403	Eppendorf, Germany
Centrifuge Biofuge Pico	Thermo Fisher Scientific, USA
Centrifuge Biofuge Primo	Thermo Fisher Scientific, USA
Centrifuge Hermle Z 283 K	Hermle Labortechnik GmbH, Germany
Cooling box with rotor	Privileg, Germany
CO ₂ incubator CB150	Binder, Tuttlingen, DE
Electrophoresis Cell Criterion	Bio-Rad Laboratories, USA
Gel documentation Dunkelhaube D4	Biostep GmbH, Germany
Gel electrophoresis system E865	Consort, Belgium
Gel electrophoresis system PSU EPS600	Pfizer, New York, USA
Imager LAS3000	Fujifilm, Tokyo, Japan
Incubating orbital shaker 3500l	VWR International, USA
Incubator Heracell 150	Thermo Fisher Scientific, USA
Incubator Heracell 150i	Thermo Fisher Scientific, USA
Laminar flow hood Clean Wizard V 100	Kojair Tech Oy, Vilppula, Finland
Laminar flow hood Herasafe HS	Thermo Fisher Scientific, USA
Laser Scanning Confocal Microscope LSM 900 with Airyscan2	Carl Zeiss, Germany
Light Cycler Nano	Roche, Switzerland
Light Cycler 480II	Roche, Switzerland
Manual pipettes	Eppendorf, Germany
Microplate reader Sunrise	Tecan Group, Switzerland
Microplate reader Spark	Tecan Group, Switzerland
Multichannel pipette	Brand GmbH & Co. KG, Germany

Odyssey 9120 Fluorescent Imager	LI-COR Biosciences, USA
Odyssey XF Imager	LI-COR Biosciences, USA
Pipette 31lpha31p31bl, PIPETBOY	Integra Biosciences, Switzerland
Pipette set	Eppendorf, Germany
PCR cycler – Mastercycler gradient	Eppendorf, Germany
PowerPac Universal Power Supply	Bio-Rad Laboratories, USA
Real time PCR cycler MX3000P	Agilent, USA
RotaMax 150 Shaker	Heidolph, Germany
Shaking incubator 3032	GFL, Germany
Spark Multimode Microplate Reader	Tecan Group, Switzerland
Stereo preparation microscope Stemi DV4SteREO CL 1500 ECO	Carl Zeiss, Germany
Thermo shaker PST-60HL-4 Lab4You	Dewert Labortechnik, Germany
Thermomixer – Thermomixer 5436	Eppendorf, Germany
Thermomixer – Thermomixer Comfort	Eppendorf, Germany
Trans-Blot Turbo Transfer System	Bio-Rad Laboratories, USA
Transilluminator – BioView UST 30M-8R	Biostep GmbH, Germany
Water bath	Memmert GmbH & Co. KG, Germany
Water bath — Julambo SW22	JULAMBO Labortechnik GmbH, Germany

3.1.2 Chemicals and reagents

Table 3.2: Chemicals and reagents

NAME	COMPANY
4-15% Criterion TGX Precast midiproteins gels	Bio-Rad Laboratories, USA
40% solution Rhotiphorese gel 40	Carl Roth GmbH & Co. KG, Germany
autoMACS rinsing solution	Miltenyi Biotec GmbH, Bergisch-Gladbach, DE
Acetone	Carl Roth GmbH & Co KG, Karlsruhe,
Acetic Acid	Sigma-Aldrich, USA
Agarose	Biozym Biotech Trading GmbH, Germany
Ampicillin	Carl Roth GmbH & Co. KG, Germany
APS	Carl Roth GmbH & Co. KG, Germany

Materials and methods

BD FACS Flow™ Sheath Fluid	BD Biosciences, Heidelberg, DE
BD™ FACS Clean	BD Biosciences, Heidelberg, DE
BD™ FACS Rinse	BD Biosciences, Heidelberg, DE
BSA Fraction V	Thermo Fisher Scientific, USA
Bromophenol Blue	Sigma-Aldrich, USA
CaCl ₂	Merck KGaA, Darmstadt, DE
Complete Protease Inhibitor Cocktail Tablets	Sigma-Aldrich, USA
DAPI Fluoromount G	SouthernBiotech, USA
Dithiothreitol	Sigma-Aldrich, USA
DMSO	Sigma-Aldrich, USA
Doxycyclin Hyclate	Sigma-Aldrich, USA
dNTP Mix, 10 µM each	Thermo Fisher Scientific, USA
D-Sorbitol	Sigma-Aldrich, USA
EDTA	Thermo Fisher Scientific, USA
Ethanol	VWR International GmbH, Germany
Etoposide	Sigma-Aldrich, USA
Fluoromount	SouthernBiotech, USA
HEPES Buffer	Thermo Fischer Scientific, USA
Hydrogen peroxide 30% (w/w) in H ₂ O	Sigma-Aldrich, USA
Isopropanol	VWR International GmbH, Germany
Laminin	Sigma-Aldrich, USA
Matrigel Matrix	Corning Inc., USA
MACS BSA stock solution	Miltenyi Biotec GmbH, Bergisch-Gladbach, DE
NaCl	Merck Group, Germany
Paraformaldehyde 4% solution	Seipt, Klinikapotheke UKD, Germany
PCR Grade Water	Biotechrabbit, Germany
Phosphate Buffered Saline, pH 7.4	Thermo Fischer Scientific, USA
PhosSTOP Phosphatase Inhibitor Tablets	Sigma-Aldrich, USA
Pierce™ Protein-Free (PBS) Blocking Buffer	Thermo Fischer Scientific, USA
Ponceau S-Lösung	Sigma-Aldrich, USA
Poly-L-Ornithine	Sigma-Aldrich, USA
Precision Plus Protein Dual Xtra Prestained Protein Standard	Bio-Rad Laboratories, USA
RIPA Lysis and Extraction Buffer	Thermo Fischer Scientific, USA

Revert™ 700 Total Protein Stain Kits for Western Blot Normalization	Thermo Fisher Scientific, USA
Skim milk powder	Sigma-Aldrich, USA
Sodium Arsenite	Sigma-Aldrich, USA
Sodium Bicarbonate	Thermo Fischer Scientific, USA
Sodium Dodecyl Sulphate	Carl Roth GmbH & Co. KG, Germany
Sterile Rnase-free water	Thermo Fisher Scientific, USA
Tris-HCL	Carl Roth GmbH & Co. KG, Germany
TEMED	Carl Roth GmbH & Co. KG, Germany
TritonX-100	Thermo Fisher Scientific, USA
Tween 20	Serva Elektrophoresis GmbH, Germany

Table 3.3: Commercially available kits

NAME	COMPANY
Anti-PSA-NCAM MicroBead Kit	Miltenyi Biotec GmbH, Bergisch-Gladbach, DE
Anti-O4 MicroBeads, human, mouse and rat	Miltenyi Biotec GmbH, Bergisch-Gladbach, DE
CTS™ CytoTune™-iPS 2.1 Sendai Reprogramming Kit	Thermo Fischer Scientific, USA
ECL Prime Western Blotting Detection Reagent	GE Healthcare, USA
Expand High Fidelity PCR System	Sigma-Aldrich, Germany
miRNeasy Mini Kit	Qiagen, Germany
FastStart Universal SYBR Green Master Mix (ROX)	Roche, Switzerland
FTA Sample Collection Kit for Human Cell Authentication Service	American Type Culture Collection (ATCC), Manassas, VA, US
High-Capacity cDNA Reverse Transcription Kit	Thermo Fischer Scientific, USA
JC-10 mitochondrial membrane potential kit	AAT Bioquest, Sunnyvale, CA, USA
PCR Mycoplasma Test Kit I/C	PromoCell GmbH, Heidelberg, DE
Pierce BCA Protein Assay Kit	Thermo Fischer Scientific, USA
PrestoBlue Viability Assay	Thermo Fischer Scientific, USA
QuantiTect Reverse Transcription Kit	Qiagen, Germany
QuantiTect Syber Green PCR Kit	Qiagen, Germany
Quick-RNA Miniprep Kit	Zymo Research, USA
Trans-Blot Turbo Midi Nitrocellulose Transfer Packs	Bio-Rad Laboratories, USA
True-Nuclear™ Transcription Factor Buffer Set	Biolegend, San Diego, CA, US

ZR Plasmid Miniprep Kit	Zymo Research, USA
-------------------------	--------------------

3.1.3 Cell culture media and supplements

Table 3.4: Cell culture media and supplements

NAME	COMPANY
Accutase	Sigma-Aldrich, USA
B-27™ Supplement (50x)	Fisher Scientific GmbH, Schwerte, DE
B27 Supplement, w/o vitamin A	Thermo Fischer Scientific, USA
β-Mercaptoethanol	Thermo Fischer Scientific, USA
DMEM High Glucose Medium	Thermo Fischer Scientific, USA
DMEM/F12 Medium	Thermo Fischer Scientific, USA
Fetal Bovine Serum	Sigma-Aldrich, USA
Gelatin (pork skin type A; 0.1% dissolved in A. dest)	Sigma-Aldrich Chemie GmbH, Taufkirchen, DE
Gentle Cell Dissociation Reagent	Stemcell Technologies, Cologne, DE
Laminin I (mouse) 1 mg/ml (10 µg/ml in DMEM/F-12)	R&D Systems, Abingdon, UK
Knockout DMEM	Gibco, Thermo Fisher Scientific, Darmstadt, DE
Knockout Serum Replacement	Gibco, Thermo Fisher Scientific, Darmstadt, DE
mTeSR1 complete medium	Stemcell Technologies, Cologne, DE
MEM NEAA (100x) (Minimum Essential Medium Non-Essential Amino Acids)	Gibco, Thermo Fisher Scientific, Darmstadt, DE
Neurobasal Medium	Thermo Fischer Scientific, USA
PBS Dulbecco (PBS ^{-/-} , without calcium and magnesium)	PAN-Biotech GmbH, Aidenbach, DE
Penicillin-Streptomycin-Glutamine	Thermo Fischer Scientific, USA
PLO (poly-L-ornithine hydrobromide; 15 mg/ml dissolved in A. dest)	Sigma-Aldrich Chemie GmbH, Taufkirchen, DE
ReleSR™	Stemcell Technologies, Cologne, DE
Trypsin-EDTA 0.25% (1x)	Gibco, Thermo Fisher Scientific, Darmstadt, DE

Table 3.5: Growth factors and small molecules

NAME	COMPANY
3,3',5-Triiodo-L-thyronine	Sigma-Aldrich, USA
Activin A	Peptotech, USA
Ascorbic Acid	Sigma-Aldrich, USA
Biotin	Sigma-Aldrich, USA
Dibutyryl cAMP sodium salt	Sigma-Aldrich, USA
Doxycycline	Sigma-Aldrich, USA
EGF (epidermal growth factor),	Peptotech, Hamburg, DE
FGF2 (fibroblast growth factor),	Amsbio, Abingdon, UK
Human insulin solution	Sigma-Aldrich, USA
L-Ascorbic acid	Sigma-Aldrich, USA
Recombinant human insulin growth factor-1 (IGF1)	Peptotech, Hamburg, DE
Recombinant human hepatocyte growth factor (HGF)	Peptotech, Hamburg, DE
Recombinant human neurotrophin 3 (NT3)	Peptotech, Hamburg, DE
Recombinant human platelet-derived growth factor-AA (PDGF-AA)	Peptotech, Hamburg, DE
Retinoic Acid	Sigma-Aldrich, USA
Smoothened Agonist (SAG)	Sigma-Aldrich, USA
SB431542	Tocris Bioscience, UK
StemMACS LDN-193189	Miltenyi Biotec GmbH, Bergisch-Gladbach, DE
Y-27632, 10 mM in DMSO	Miltenyi Biotec GmbH, Bergisch-Gladbach, DE

Table 3.6: Composition of buffers and solutions

NAME	COMPOSITION	
1x SDS electrophoresis buffer	10x SDS electrophoresis buffer: Aqua distilled.	1:9
10x SDS electrophoresis buffer	TRIS Glycine SDS	250mM 2 m 0.1%
10x TBS	TRIS NaCl Adjust pH 7.5	200mM 1.37M
1x TBS	10x TBS: Aqua distilled.	1:9

Materials and methods

1x TBST	1x TBS Tween 20	0.1%
5x Laemmli buffers	TRIS Glycerol SDS β -Mercaptoethanol Bromophenol blue	125mM 20% 2% 5% 10%
5x TBE buffer	TRIS Boric acid 0.5 M EDTA (pH 8.3)	54g 27.5g 20ml
50x TAE buffers	TRIS Glacial vinegar 0.5 mM EDTA (pH 8.0) to 1 l with distilled water. fill up	242g 57.1ml 100ml
Antibody solution	1% BSA Triton X-100	0.1%
Antibody solution	Skimmed milk powder in 1x TBST	3%
Block solution	Skimmed milk powder in 1x TBST	5%
FACS block buffer	PBS FBS	10%
FACS buffer	PBS FBS	2%
Fixative solution for karyogram	Methanol: Glacial acetic acid	3:1
Immunofluorescence block buffer	PBS BSA	1%
Immunofluorescence block buffer	1% BSA Normal goat serum Triton X-100	10% 0.1%
Immunofluorescence wash buffer	PBS Tris-HCl (pH 8.5) NaCl Tween	20mM 0.15M 0.05%
KCl solution	Aqua distilled. KCl	0.075M
MACS buffer	PBS BSA	0.5%

Materials and methods

	EDTA	2mM
Paraformaldehyde	PBS PFA	4%
PBS+/+	PBS CaCl ₂ MgCl ₂	0.5mM 0.9mM
RIPA buffer	TRIS NaCl Sodium deoxycholate EDTA SDS Triton X-100 Glycerol Dissolve 1 cOmplete mini protease inhibitor tablet in 10 ml RIPA buffer	20mM 137mM 12mM 2mM 0.1% 1 % 10%
Triton buffer	SDSTriton X-100	1 % 0.1%

Table 3.7: Standards and dyes

NAME	COMPANY
GeneRuler™ 100 bp Plus DNA Ladder	Thermo Fisher Scientific, Waltham, MA, US
Precision Plus Protein™ Dual Xtra Prestained Protein Standard	Bio-Rad Laboratories, Feldkirchen, DE

3.1.4 Antibodies and primers

Table 3.8: Primary antibodies

NAME	HOST	DILUTION	COMPANY	REFERENCE NO.
ALPHA-FETOPROTEIN	Mouse, IgG	1:1000	Sigma-Aldrich, DE	A8452
BETA III TUBULIN		1:1000	Santa Cruz Heidelberg, DE	SC51670
FA2H	Rabbits IgG polyclonal	1:1000	Invitrogen	PA5-24728

Materials and methods

GAPDH	Mouse IgG monoclonal	1:10.000	Abcam, Cambridge, UK	AB8245
GFAP	Rabbits IgG polyclonal	1:1000	Agilent Technologies, Santa Clara, CA, US	Z0334
KCNQ2/KV7.2	Mouse IgG monoclonal	1:100	Abcam, Cambridge, UK	AB22897
LC3B(E5Q2K)	Mouse IgG	1:1000	Cell signaling	83506S
MAP2	Chicken IgY	1:2000	Abcam, Cambridge, UK	AB5392
MBP	Chicken IgY	1:100	Thermo Fisher Scientific, MA, US	AB9348
MBP aa 82–87	Rat IgG	1:75	EMD Millipore	MAB386
MUSCLE ACTIN	Mouse IgG monoclonal	1:1000	Agilent Technologies, Santa Clara, CA, US	M0635
NANOG	Rabbits IgG polyclonal	1:500	Stemgent, Cambridge, MA,US	09-0020
NESTIN	Rabbits IgG polyclonal	1:1000	Abcam, Cambridge, UK	AB92391
OLIG2		1:100	R&D Systems, Abingdon, UK	SC-19969
Oct4	Rabbits IgG polyclonal	1:1000	Stemgent, Cambridge, MA,US	09-0023
O4	Mouse, IgM	1:100	R&D Systems, Abingdon, UK	MAB1326
PAX6	Rabbits IgG polyclonal	1:1000	Abcam, Cambridge, UK	AB5790
PLP	Rabbit IgG polyclonal	1:100	Abcam, Cambridge, UK	AB_9311
SOX10	Rabbit IgG polyclonal	1:1000	R&D Systems, Abingdon, UK	AF1924
SOX2	Rabbits IgG monoclonal	1:1000	Abcam, Cambridge, UK	AB92494
SSEA4	Mouse IgG polyclonal	1:500	Stemgent, Cambridge, MA,US	09-0006

SQSTM1/p62	Rabbit IgG polyclonal	1:250	Abcam, Cambridge, UK	AB_109012
TRA-1-60	Mouse IgM monoclonal	1:1000	Stemgent, Cambridge, MA,US	09-0010
TRA-1-81	Mouse IgM monoclonal	1:1000	Stemgent, Cambridge, MA,US	09-0011
B-ACTIN	Mouse IgG monoclonal	1:10.000	Sigma-Aldrich	A5441

Table 3.9: Secondary antibodies

NAME	HOST	DILUTION	COMPANY	REFERENCE NO.
Alexa Fluor 488, 647	Goat anti-Chicken IgG (H+L)	1:500	Invitrogen/Thermo Fisher Scientific, Darmstadt, DE	A21449
Alexa Fluor 488	Goat anti-Rabbit IgG	1:500	Invitrogen/Thermo Fisher Scientific, Darmstadt, DE	A11034
Alexa Fluor 488, 568	Goat anti-Mouse IgG	1:500	Invitrogen/Thermo Fisher Scientific, Darmstadt, DE	A11031
Alexa Fluor 568	Goat anti-Rabbit IgG	1:500	Invitrogen/Thermo Fisher Scientific, Darmstadt, DE	A11036
Alexa Fluor 568, 647	Goat anti-Mouse IgM	1:500	Invitrogen/Thermo Fisher Scientific, Darmstadt, DE	A21043
Goat anti-Mouse IgG	DyLight 680	1:10 000	Rockland Immunochemicals Inc., Gilbertsville, PA, US	610-144-121
Goat anti-Mouse IgG	DyLight 800	1:10 000	Rockland Immunochemicals Inc., Gilbertsville, PA, US	610-145-003
Goat anti-Rabbit IgG	DyLight 800	1:10 000	Rockland Immunochemicals Inc., Gilbertsville, PA, US	611-145-122
Goat anti-Rabbit IgG	DyLight 680	1:10 000	Rockland Immunochemicals Inc., Gilbertsville, PA, US	611-144-002

Goat anti-Rat IgG	DyLight 680	1:10 000	Rockland Immunochemicals Inc., Gilbertsville, PA, US	612-144-002
Goat anti-Rat IgG	DyLight 800	1:10 000	Rockland Immunochemicals Inc., Gilbertsville, PA, US	612-145-002

Table 3.10: Conjugated primary antibodies for flow cytometry

NAME	HOST	DILUTION	COMPANY	REFERENCE NO.
Alexa Fluor [®] 647 anti-NANOG	Mouse IgG monoclonal	1:50	Biolegend, San Diego, CA, US	674210
Alexa Fluor [®] 647 anti-SSEA4	Mouse IgG monoclonal	1:500	Biolegend, San Diego, CA, US	330407
PE anti-human TRA- 1-60-R	Mouse IgG monoclonal	1:20	Biolegend, San Diego, CA, US	330609
Alexa Fluor [®] 488 anti-TRA-1-81	Mouse IgG monoclonal	1:20	Biolegend, San Diego, CA, US	330709
Alexa Fluor [®] 488 anti-OCT4	Mouse IgG monoclonal	1:20	Biolegend, San Diego, CA, US	653705

Table 3.11: Primers

NAME	Forward/Reverse Primer (5'-3')	Length	Annealing Temp Ta[°C]	Cycle Number
C-MYC	GCGTCCTGGGAAGGGAGATCCGGAGC/ TTGAGGGGCATCGTCGCGGGAGGCTG	325	66	30
ESG1	ATATCCCGCCGTGGGTGAAAGTTC/ ACTCAGCCATGGACTGGAGCATCC	176	57	35
FGF4	CAAGCTCTATGGCTCGCCCT/ TCTTCCATTCTTGCTCAGGG	131	57	40
GAPDH	CATGTTCCAATATGATTCCACCC/ GGGATCTCGCCTCCTGGAAGAT	112	57	40
hTERT	GAGCTGACGTGGAAGATGAGC/ CATCAGCCAGTGCAGGA ACTT	129	57	35

KLF4	ACGATCGTGGCCCCGGAAAAGGACC/ TGATTGTAGTGCTTTCTGGCTGGGCTC	397	65	35
NANOG	TGTGTTCTCTTCCACCCAGC/ ACCAGGTCTTCACCTGTTTGT	128	55	30
OCT4	GACAGGGGGAGGGGAGGAGCTAGG/ CTTCCCTCCAACCAGTTGCCCAAAC	144	66	30
SOX2	AGGGAGAGAAGTTTGAGCCC/ GCGAGGAAAATCAGGCGAAG	170	55	30
ZFP296	CTGGACCGACAAACACCCAG/ CTTCAGCTCCTCTCGTTCTGAG	157	57	35
SOX2_ pMIG/IRES	CATGTCCCAGCACTACCAGA/ GCATTCCTTTGGCGAGAG	257	60	30
KLF4_ pMIG/IRES	CCCACACAGGTGAGAAACCT/ GCATTCCTTTGGCGAGAG	366	60	30
C-MYC_ MSCV/IRES	AAGAGGACTTGTTGCGGAAA/ GCATTCCTTTGGCGAGAG	337	60	30
OCT4 pMIG/IRES	GTACTCCTCGGTCCCTTCC/ GCATTCCTTTGGCGAGAG	260	60	30

Table 3.12: Microorganism strain used

NAME	ORGANISM	GENOTYPE	COMPANY
XL10-Gold [®] Ultracompetent Cells	<i>Escherichia coli</i>	<i>TetrD(mcrA)I83</i> <i>D(mcrCB-hsdSMR- mrr)I73 endA1</i> <i>supE44 thi-1 recA1</i> <i>gyrA96 relA1 lac Hte</i> <i>[F' proAB</i> <i>lacIqZDM15 Tn10</i> <i>(Tetr) Amy Camr]</i>	Agilent Technologies, Santa Clara, CA, US

Table 3.13: Culture media for growing the micro-organism strain

NAME	COMPOSITION
LB _{Amp} Agar	40 g LB -agar (Roth) to 1:1 distilled water. → Autoclave for 20 minutes → Addition of ampicillin (100 µg/ml)

LB _{Amp} medium	25 g LB -Medium (Roth) to 1:1 distilled water. → Autoclave for 20 minutes → Addition of ampicillin (100 µg/ml)
--------------------------	--

Table 3.14: Consumables

NAME	COMPANY
Cell Culture Flasks 25ml, 75ml	Corning, USA
Cell Culture Plates (4-, 6-, 12-, 24-well)	Sarstedt, Germany; Thermo Fischer Scientific, USA; TPP Techno Plastic Products AG, Switzerland; Corning, USA
Cell Scraper	Carl Roth, Germany
Conical Bottom Centrifuge Tubes 15ml, 50ml	Greiner Bio-One, Austria
Costar® Stripette® 2-50ml	Corning, USA
Falcon® Round-Bottom Tubes with Cell Strainer Cap	STEMCELL Technologies, Canada
Glass Cover Slips	Thermo Fischer Scientific, USA
MicroAmp™ Reaction Tube, 0.2ml	Thermo Fischer Scientific, USA
Minisart® Syringe Filters 0.45µm, 0.2µm	Sartorius, Germany
Nalgene® Freezing Container	Sigma Aldrich, Germany
PVDF Syringe Filters, 0.45µm, 0.2µm	Sigma-Aldrich, USA
Superfrost® Microscope Slides	Thermo Fischer Scientific, USA
µ-Slide 8 Well Glass Bottom	Ibidi, Germany

Table 3.15: Plasmids

PLASMID	INSERT	BACKBONE	ORDER NO.	COMPANY
FUW-TetON-Sox10	9783	FUW TetON	115242	Addgene, MA, US
FUW-M2rtTA	9792	FUW (Lenti-Lox-Ubi)	20342	Addgene, MA, US
Envelope plasmid pMD2.G		pMD2.G	12259	Addgene, MA, US
Packaging plasmid psPAX2	10703	psPAX2	12260	Addgene, MA, US
pMD2.G	6363	VSV-G	8454	Addgene, MA, US

Table 3.16: Software

SOFTWARE	FUNCTION	SOURCE
Adobe Illustrator CC 2017 21.0	Graphics design	Adobe Systems, USA
BZ image analysis application	image analysis application	Keyence, Osaka, JP
BZ observation application	observation application	Keyence, Osaka, JP
Cell Quest Pro		BD, Heidelberg, DE
Citavi 6	Reference	Swiss Academic Software, Wädenswil, CH
CorelDRAW 2020	Figure design	Corel Corporation, Ottawa, CA
Empiria Studio Software	Western Blot quantification	LI-COR Bioesciences, USA
ImageJ	image analysis application	National Institutes of Health, Bethesda, MD, US
GraphPad Prism 8.0.1	quantification	GraphPad Prism 8.0.1
LightCycler Nano	qPCR data analysis	Roche, Switzerland
Microsoft Office		Microsoft Corporation, Redmond, WA, US
SNAPGENE	Primer design, analyzing	San Diego, California, USA
SparkControl™	DNA, RNA concentration measurement	Tecan Group Ltd., Männedorf, CH
ZEN imaging software	image analysis application	Carl Zeiss AG, Oberkochen, DE

3.1.5 Cell culture media

Table 3.17: Cell culture media used

NAME	AMOUNT	COMPOSITION
Basic medium	10%	DMEM
	1 %	FBS Penicillin/streptomycin
Basal medium	50%	DMEM/F12
	50%	neurobasal medium
	1x	N2 supplement
	1x	B27(with RA), GlutaMAX

Materials and methods

	0.5%	penicillin-streptomycin
Stem cell medium	20% 0.1mM 1 % 0.1mM 1 % 10ng/ml	DMEM-F12 Knockout Serum Replacement Non-essential amino acids GlutaMAX 2-Mercaptoethanol Penicillin/streptomycin FGF2
mTesR1 complete medium	400ml 100ml 0.25%	mTesR1 basal medium mTeSR1 Supplement Penicillin/streptomycin
EB medium	78% 20% 1 % 2mM 0.1mM 0.25%	Knockout DMEM FBS Non-essential amino acids GlutaMAX 2-Mercaptoethanol Penicillin/streptomycin
Proliferation medium	60% 40% 1x 0.5% 20ng/ml	DMEM DMEM-F12 B27 Penicillin/streptomycin FGF2 and EGF
Differentiation medium	60% 40% 1x 0.5%	DMEM DMEM-F12 B27 Penicillin/streptomycin
NIM medium		Basal medium 5 ng/ml FGF2, 20 μ M/ml SB-431542 and 1 Mm/ml LDN193189
OL differentiation medium		Basal medium 10 ng/ml PDGF-AA, 10 ng/ml IGF1, 5 ng/ml HGF, 10 ng/ml NT3, 100 ng/ml biotin, 1 μ M cAMP, 60 ng/ml T3 and 1 μ g/ml

		doxycycline
Co-culture medium		Basal medium 100 ng/ml biotin, 1 μ M cAMP, 25 μ g/ml insulin and 1 μ g/ml doxycycline
Cryopreserving medium		Medium 10% DMSO

3.1.6 Cell lines

The cell lines used in this study are shown in Table 3.18 and Table 3.19. The control cell line was obtained from our former colleague and this cell line was reprogrammed and characterised by Dr. Christin Völkner. The three FAHN patient fibroblast cell lines were obtained from the laboratory of collaborator Dr. Sunita Venkateswaran at the Children's Hospital of Eastern Ontario, Canada. All three FAHN cell lines were reprogrammed into iPSCs, characterised and published (Efendic et al., 2022; Efendic et al., 2023). For the sake of clarity, two cell lines, FAHN1 (AKOSi010-A) and Control (GM08398-1), were included in the study in Table 3.1 and all pathophysiological experiments were performed on these two cell lines.

Table 3.18 Control and FAHN cell lines used in the study

Name	Cell line clone	Mutation	Protein	Gender	Age of biopsy
FAHN1	AKOSi010-A	c.133G>A c. 956A>G	(p. Gly45Arg) 1 exon (p. His319Arg) 6 exon	Female	8 years old
Control	GM08398-1	-	-	Female	

Table 3.19 lists all cell lines used for the generation and cultivation of iPSC cells.

Table 3.19 Cell lines used

Cell type	Cell line	Purpose	Company
iPSCs	FAHN1	Pathophysiological examination	In house generated
iPSCs	Control	Pathophysiological examination	In house generated
Human embryonic kidney cells (HEK cells)	HEK293T	Virus generation	Invitrogen Technologies, Carlsbad, USA

3.2 Cultivation of the cell lines

All experiments were performed according to local and federal rules, including work in respective S1/S2 laboratories. The cells utilized in this research were cultivated in a humidified tissue culture incubator set at 37°C, while sustaining a consistent balance of 21% oxygen and 5% carbon dioxide. The cell culture methodologies outlined in this section were executed within a sterile biosafety cabinet. All solutions and media employed were pre-warmed in a 37°C water bath before usage, unless specified otherwise.

3.2.1 Cell culture medium

Working stocks of media supplements were stored in aliquots at -20°C to prevent multiple freeze-thaw cycles. Freshly prepared media aliquots were stored at 4°C unless otherwise specified by the manufacturer, to maintain their integrity. Growth factors were consistently added before the use of prewarmed media. The cell culture media employed throughout the study are detailed in Table 3.20.

Table 3.20 Cell culture media used

Name	Amount	Composition
Basic medium	10%	DMEM
	1 %	FBS
		Penicillin/streptomycin
Basal medium	50%	DMEM/F12
	50%	neurobasal medium
	1x	N2 supplement
	1x	B27(with RA),
	1x	GlutaMAX
	0.5%	penicillin-streptomycin
Stem cell medium	20%	DMEM-F12
	0.1mM	Knockout Serum Replacement
	1 %	Non-essential amino acids
	0.1mM	GlutaMAX
	1 %	2-Mercaptoethanol
	10ng/ml	Penicillin/streptomycin
		FGF2
mTesR1 complete medium	400ml	mTesR1 basal medium

	100ml 0.25%	mTeSR1 Supplement Penicillin/streptomycin
EB medium	78% 20% 1 % 2mM 0.1mM 0.25%	Knockout DMEM FBS Non-essential amino acids GlutaMAX 2-Mercaptoethanol Penicillin/streptomycin
Proliferation medium	60% 40% 1x 0.5% 20ng/ml	DMEM DMEM-F12 B27 Penicillin/streptomycin FGF2 and EGF
Differentiation medium	60% 40% 1x 0.5%	DMEM DMEM-F12 B27 Penicillin/streptomycin
NIM medium		Basal medium 5 ng/ml FGF2, 20 μ M/ml SB-431542 and 1 Mm/ml LDN193189
OL differentiation medium		Basal medium 10 ng/ml PDGF-AA, 10 ng/ml IGF1, 5 ng/ml HGF, 10 ng/ml NT3, 100 ng/ml biotin, 1 μ M cAMP, 60 ng/ml T3 and 1 μ g/ml doxycycline
Coculture medium		Basal medium 100 ng/ml biotin, 1 μ M cAMP, 25 μ g/ml insulin and 1 μ g/ml doxycycline
Cryopreserving medium		Medium 10% DMSO

3.2.2 Coatings

Various coatings were implemented to enhance cell adhesion and monolayer culture development. A volume of 700 μ l was standard for 6-well plate coating processes. This volume was proportionally increased for plates with 24, 12 and 4 wells, and for 10 cm diameter culture dishes, 4-8 ml of the coating solution was applied.

3.2.3 Matrigel coating

Matrigel matrix stored at -20°C was preconditioned overnight at 4°C on ice, then diluted 1:5 with DMEM/F12 and stored at -20°C. For application, the preconditioned gel was equilibrated to room temperature (RT) for 15 min and further diluted 1:20 with cold DMEM/F12. Plates were immediately coated with coating solution and incubated at 37°C for 45 minutes until ready for use. Plates coated with matrix gel could be stored at 4°C for a maximum of one week if not used immediately. Prior to cell seeding, coated plates were either brought to RT for at least 60 minutes or briefly warmed at 37°C for 30 minutes. The matrix gel was then removed and cells were seeded onto the treated culture vessels without further washing.

3.2.4 Poly-L-ornithine/ Laminin coating

Neural progenitor cells and other neural cultures were propagated together with neural cultures on surfaces treated with poly-L-ornithine (PLO)/laminin. The PLO solution was prepared by diluting the stock with DPBS to a concentration of dilution factor 1:1000, then the culture plates were coated with the solution according to the plate size (see Table 3.25) and incubated overnight at 37°C. The next day, after three washes with DPBS and without drying, the plates were incubated with a dilution of 1:100 laminin solution at 37°C overnight. If not used immediately, these prepared plates could be stored at 4°C in DPBS wrapped in paraffin to reduce drying for up to two weeks or used immediately.

3.2.5 Cell count

To verify that the cells were seeded at the required density, a cell count was performed. The cells were first washed with prewarm DMEM/F12 than to detach the cells from their culture vessels, an appropriate amount of prewarm Accutase was added and the cells were further harvested. The resulting cell pellet was then suspended in 1 ml of culture medium. For accurate cell counting, a dilution, typically 1:100, was prepared by mixing 1 μ l of cell suspension with 99 μ l of medium. Counting was performed using a CellDrop counter by adding 10 μ l of the

diluted cell suspension for counting. To adjust the concentration of a cell suspension for plating, the required dilution factor can be calculated using the formula:

$$\text{Dilution} = \frac{\text{Actual cell concentration}}{\text{Target cell concentration}}$$

This calculation will indicate how much the current cell suspension needs to be diluted in order to achieve the desired concentration for plating.

3.2.6 Freezing and thawing of cells

Cell types such as fibroblasts, iPSCs and NPCs, after detachment and aggregation according to the protocols described in sections 3.2.2 to 3.4.2, are suspended in a solution containing 10% DMSO and 1 μ M ROCKi for iPSCs. This suspension is then rapidly cooled to -80°C using a controlled rate freezer and then transferred to liquid nitrogen storage for extended preservation. Typically, an entire fully coated well of a six-well culture dish is used to accommodate six to eight cryovials of cell suspension. Thawing involves the preparation of 1 to 6 wells with matrix gel or PLO/laminin coatings as described above. iPSCs or NPCs are gently thawed at 37°C until crystals are dissolved, afterwards the cells were suspended in 5 ml of suitable cell culture medium, centrifuged at 300 rpm for 3 minutes, and the resulting cell pellet is resuspended in 1 ml of iPSCs medium containing ROCKi inhibitor to ensure uniform distribution within the well. After 24 hours of cell attachment and recovery, the cell medium was replaced with an appropriate medium without ROCKi inhibitor.

Table 3.21: Cryopreservation of cells

Cell type	Cell count	Cryopreservation medium
Human fibroblasts	2.0×10^6 -	Base medium + 10% DMSO
HEK293T cells	2.5×10^6 -	Base medium + 10% DMSO
iPSCs on E8	50 colony pieces	E8 medium + 10% DMSO
iPSCs on Matrigel	1/5 of a full 6-well	mTesR1 complete medium + 10% DMSO
Neural progenitor cells	2.0×10^6 -	Proliferation medium + 10% DMSO

3.2.7 Cultivation of human fibroblasts and HEK293T cells

Both human fibroblasts and HEK293FT cells were grown in T75 cell culture flasks in basal medium and passaged at approximately 95% confluence. For this purpose, the cell culture medium was aspirated and the cells were washed with 10 ml phosphate-buffered saline (DPBS). 2.5 ml of 0.25% trypsin-EDTA was then added per T75 cell culture flask and incubated at 37°C for 5 minutes. After the cells were detached from the bottom of the flask, the enzymatic reaction was stopped with 7.5 ml of basal medium. The cells were transferred to a centrifuge tube and centrifuged at $400 \times g$ for 5 minutes. After removal of the supernatant, the cells were resuspended in basal medium and the cell number was determined using the CellDrop cell counting system. For continuous culture, 2.0×10^6 fibroblasts or 2.5×10^6 HEK293FT cells were seeded per T75 cell culture flask.

3.3 Generation of iPSCs from Fibroblasts

The process of converting human fibroblasts into iPSCs was accomplished by transducing them with the transcription factors OCT4, SOX2, KLF4, and c-MYC, as described by Takahashi and Yamanaka in 2006. The CytoTune™-iPS 2.0 Sendai Reprogramming Kit (refer to table 3.3) includes three reprogramming vectors: KOS (Klf4, Oct3/4, and Sox2), hc-Myc, and hKlf4. These vectors were utilized to deliver and express the essential genetic factors required for reprogramming somatic cells into iPSCs. The CytoTune™-iPS 2.0 Reprogramming System employs vectors based on a modified, non-transmissible form of the respiratory virus, Sendai virus (SeV).

3.3.1 Reprogramming human fibroblasts into iPSCs

Two days prior to transduction, patient-specific fibroblast cells were seeded onto two wells of a 6-well plate at a density of 2×10^5 – 3×10^5 cells per well. The plate was then incubated at 37 °C, 5% CO₂, and 90% relative humidity. After two days, cells from one well were harvested and counted to estimate the cell number of the other well, which was used for transduction. The appropriate volume of the respective virus was added for optimal transduction efficiency (KOS MOI=5, hc-Myc MOI=5, hKlf4 MOI=3) and calculated according to the formula:

$$\text{Volume of virus } (\mu\text{L}) = \frac{\text{MOI (CIU/cell)} \times \text{number of cells}}{\text{titer of virus } \left(\frac{\text{CIU}}{\text{mL}}\right) \times 10^{-3} (\text{mL}/\mu\text{L})}$$

The volumes of each of the three CytoTune™ 2.0 Sendai tubes were calculated and added to 1 mL of pre-warmed (37°C) fibroblast medium. The remaining well was replaced with a

reprogramming virus mixture. After an incubation period of 24 hours, the transfection medium was replaced with fresh fibroblast medium. The cells were cultured in fibroblast basal medium for an additional six days with daily medium renewal. After seven days, the cells were passaged. For this purpose, the cells were washed twice with DPBS and then detached from the cell culture dish with 0.5 ml of 0.05% trypsin-EDTA (37°C, 5 min). The reaction was stopped with 1 ml of basic medium, and the cells were centrifuged for 5 min at 400 × g. The cell pellet was resuspended in 2 ml of fibroblast basal medium. The cell count was determined using the CellDrop cell counting system, and the cells were then seeded in base medium on Matrigel-coated plates. After incubating for 24 hours, the fibroblast basal medium was replaced with Essential 8™ medium. The medium was renewed daily for the next eighteen days, and the fibroblasts were examined for colony development. From around day 21 after transduction, colonies with a distinct morphology became visible. These colonies are round with smooth edges and have a brownish color. To detach the colonies from the cell culture dish, a glass hook was used, and they were then transferred to fresh feeder cells. For each patient-specific fibroblast cell line, approximately 10-20 colonies were individually expanded. Detailed characterization was performed on one clone at a time.

3.3.2 Expansion and maintenance of human iPSCs

Human iPSCs were expanded on a matrix gel and maintained in mTeSR medium without animal components. iPSCs line destined for other differentiation or reprogramming remained in mTeSR medium, while those for neural differentiation were maintained in mTeSR1 supplemented with essential growth elements or in a neural induction medium. Culturing was typically performed in 12-well or 6-well plates, while cells grown for immunofluorescence analysis were cultured on Matrigel matrix coated coverslips. mTeSR medium renewal was performed routinely, except during weekend double feeding periods. Sub-culturing was performed at 70-90% confluence and cells were generally split twice a week. During splitting, cells were diluted and seeded at ratios ranging from 1:5 to 1:20. Prior to subculturing, matrix-gel coated plates were prepared and a medium without ROCKi inhibitor was preheated. iPSCs were then separated using ReLeSR, with specific volumes for different well plates, and the plate was gently swirled, with ReLeSR removed after 1 min. After shaking, the iPSCs were incubated without ReLeSR for 3 min at 37°C. The cells were collected, followed by the addition of mTeSR medium containing the ROCKi inhibitor and seeded at the desired density. The next day, this medium was replaced with a medium without the inhibitor.

3.4 Characterization of iPSCs

3.4.1 Alkaline phosphatase staining

Alkaline phosphatase (AP) is commonly used as a stem cell marker due to its high expression in undifferentiated stem cells. The iPSCs colonies were washed with DPBS and then fixed with ice-cold 100% methanol at -20°C for 10 minutes. The methanol was then removed, the cells were washed with PBS and the staining solution (75% distilled water, 10% NaCl 1M, 10% Tris pH 9.8, 5% MgCl₂ 1M and 1:50 5-bromo-4-chlorine-3-indolyl-phosphate/nitro blue tetrazolium (BCIP/NBT)) was added. The cells were incubated for 20 minutes at room temperature in the dark. Finally, the cells were washed with PBS and the staining was documented using a Nikon Eclipse TS100 inverted phase contrast microscope and NIS-Elements F 2.20 software.

3.4.2 Sample preparation for karyotyping

To rule out the possibility of chromosomal aberrations in the iPSCs during the reprogramming process, a karyogram was prepared for each stem cell line generated. The cells were first cultured on Matrigel. At 60-80% confluence, mitotic cell division was stopped by treating the cells with the spindle inhibitor Colcemid (0.15 µg/ml in mTeSR1 complete medium) for 90 minutes. The cells were then detached with Accutase (5 min, 37°C) and the reaction was stopped with basal medium. After a centrifugation step (300 x g, 5 min), the cell pellet was resuspended in a 0.075 M KCl solution, incubated at 37 °C for 30 min and centrifuged again. Finally, the fixative solution (methanol: glacial acetic acid 3:1) was added dropwise. The cells were pelleted by centrifugation at 300 × g for 5 min, the supernatant was discarded and this procedure was repeated three times. Finally, the cells were added to 200 µl of fixative solution and stored at -20 °C until further use. Chromosome analysis was performed using G-banding from WiCell. A minimum of 20 metaphases per line were determined. Twelve metaphases were completely karyotyped with a resolution of 300-550 bands per haploid chromosome set.

3.4.3 Differentiation of human iPSCs into three germ layers

Human iPSCs were induced to differentiate into the three primary germ layers using embryoid body (EB) formation techniques. The iPSCs were expanded under normal conditions until they reached a confluence of 70-90%. At this stage, the colonies were rinsed with DPBS and then treated with a dispase solution diluted in iPSC-specific medium for 30-45 minutes. Cell detachment was monitored at ten-minute intervals. Collected colonies were then centrifuged and handled gently to maintain their integrity. After centrifugation, the cells were rinsed twice

in DMEM to remove any remaining dispase and resuspended in fresh medium. The cells were then centrifuged again to remove any remaining medium and debris, after which the cells were plated on appropriate dishes in mTeSR1 medium containing a ROCK inhibitor. The next day, half of the mTeSR medium was replaced with medium supplemented with ROCK inhibitor. After 2 days, the EBs were centrifuged and transferred to differentiation-specific medium. The medium was refreshed biweekly over a period of two weeks. After two weeks, the cells were washed with DPBS, fixed and permeabilized in preparation for immunofluorescence assays.

3.4.4 Sample preparation for short tandem repeat analysis

Short tandem repeat (STR) analysis was performed by American Type Culture Collection (ATCC, Manassas, VA, US). The *FTA Sample Collection Kit For Human Cell Authentication Service* was used for this purpose. In preparation, 1.0×10^6 fibroblasts or iPSCs were harvested enzymatically and pipetted dropwise onto the Whatman[®] FTA[®] cards according to the manufacturer's instructions. 18 loci were analyzed by ATCC per sample (D5S818, D13S317, D7S820, D16S539, vWA, TH01, AMEL, TPOX and CSF1PO).

3.4.5 Flow cytometry

For the quantitative detection of pluripotency-associated proteins, flow cytometric analyses were performed using the FACS Calibur instrument and CellQuest Pro software. First, iPSCs were enzymatically detached from the cell culture plates and 1.0×10^6 cells/sample were transferred into a 1.5 ml reaction vessel. To detect the intracellular transcription factors OCT4 and NANOG, the cells were treated with the True-Nuclear Transcription Factor Buffer Set. Cells were incubated for 1 hour in 1 ml of fixative, washed with 1 ml of the permeabilization buffer provided in the set and finally resuspended in 100 μ l of permeabilization buffer. After adding the appropriate conjugated primary antibody at the appropriate dilution (see Table A.10), cells were incubated in the dark for 30 min and then collected in 300 μ l of FACS buffer. For detection of extracellular markers (SSEA4, Tra-1-60 and Tra-1-81), cells were incubated in 1 ml block buffer for 30 min at 4°C. The cells were then washed in FACS buffer and collected in 100 μ l of FACS buffer. After addition of the conjugated secondary antibody (see Table A.10), the cells were incubated for 90 min at 4 °C in the dark and then collected in 300 μ l of FACS buffer. 50,000 cells/sample were measured on the flow cytometer, with an unstained negative control included in each case. Using forward and side scattered light, events of very small size and granularity were identified as cell debris and were not included in the analysis.

Analysis and presentation were performed using FCSalyzer software. The proportion of positively stained cells was expressed as a percentage.

3.4.6 Sample preparation for targeted sequencing

To perform targeted sequencing of FA2H in the generated iPSCs line or original cells, genomic DNA was isolated from the fibroblasts using the Quick-DNA™ Miniprep Kit (Zymo Research Europe GmbH, Freiburg, DE) following the manufacturer's instructions. The sequencing was performed by employees of the Department of Hematology, Oncology and Palliative Medicine at Rostock University Medical Center, led by PD Dr. Hugo Murua Escobar using 10 ng of genomic DNA.

3.4.7 Immunofluorescence staining of iPSCs and EBs

The iPSCs or EBs were washed with 500 µl of washing buffer (20 mM Tris-HCl (pH 8.5); 0.15 M NaCl; 0.05% Tween 20 in DPBS) and then incubated for 45 minutes in a 300 µl blocking solution containing 10% normal goat serum and 0.1% Triton X-100 in 1% bovine serum albumin (BSA) dissolved in DPBS. After two washes with 500 µl wash buffer, the primary antibodies were applied using the antibody solution (0.1% Triton X-100 in 1% BSA/DPBS) and pipetted onto the cells. The cells were then incubated overnight at 4°C. Table A.8 lists the antibodies used and their corresponding dilutions. The next day, the cells on the coverslips were washed three times with wash buffer. The secondary antibodies (see Table A.9) were then added and incubated for two hours at room temperature in the dark. After three washes, the cells were treated with 4',6-diamidino-2-phenylindole (DAPI), a DNA dye, at a concentration of 250 ng/ml. The cells were incubated for five minutes at room temperature in the absence of light. After incubation, the cells were washed three times with DPBS and mounted on slides with Fluoromount-G®. The staining was analysed using a Keyence Biozero 8000 fluorescence microscope and evaluated using the supplied BZ observation application software.

3.4.8 qRNA isolation, reverse transcription and quantitative polymerase chain reaction

3.4.8.1 RNA isolation and reverse transcription

RNA isolation was performed using the Quick-RNA Miniprep Kit (see Table A.3) according to the manufacturer's instructions. RNA concentration was measured using either a Qubit fluorometer or a microplate reader with a NanoQuant plate. The High Capacity cDNA Synthesis Kit (see Table A.3) was used for reverse transcription. The reaction was prepared by mixing 1

μg RNA with 2 μl 10X RT buffer, 0.8 μl 25X dNTP mix (100 mM), 2 μl 10X random primers and 1 μl reverse transcriptase. The mixture was then filled with RNase-free PCR grade water to give a final reaction volume of 20 μL . The reaction was carried out using the thermal profile shown in Table 3.23.

Table 3.22: Thermal Profile of the Reverse Transcription Reaction

Temperature	Time
25°C	10 minutes
37°C	120 minutes
85°C	5 minutes
4°C	hold

3.4.8.2 Isolation of genomic DNA

To isolate genomic DNA (gDNA), cells were grown in a 1w/6w format. After washing the cells once with DPBS, 1 ml of fresh DPBS was added to the cells. The cells were then scraped off the plate with a cell scraper and transferred to a 1.5 ml tube. Finally, the cells were centrifuged. After centrifugation, the supernatant was removed. The cell pellet was either used immediately for gDNA isolation or stored at -20°C for later extraction. The DNeasy Blood & Tissue Kit (see Table A.3) was used for gDNA isolation according to the manufacturer's instructions.

3.4.8.3 Quantitative polymerase chain reaction

The FastStart SYBR Green Kit was used for quantitative polymerase chain reaction (qPCR) (see Table 3.3). The master mix was prepared by combining 15 μl of FastStart SYBR Green Master, 1.5 μl of 10 μM Primer Forward (final concentration 300 nM), 1.5 μl of 10 μM Primer Reverse (final concentration 300 nM), and 7 μl of PCR Grade Water. Next, 5 μl of cDNA, synthesized as described in section 3.4.8, was pipetted into a MicroAmp™ Reaction Tube, and 25 μl of an appropriate master mix was added. The reaction was carried out using LightCycler Nano or LightCycler 480II with the thermal profile specified in the table 3.23.

Table 3.23: Program for qPCR

Step	Temp	Time
Initial Denaturation	94°C	1 min
	94°C	30 sec
30x cycles	64°C	30 sec

	68°C	30 sec
Final Extension	68°C	5 min
Hold	4°C	

3.4.9 Agarose gel electrophoresis

The PCR products were analysed by agarose gel electrophoresis. To prepare a 1% (w/v) gel, 0.5 g of agarose was dissolved in 50 ml of 1xTAE buffer in a conical flask and then heated in a microwave until completely dissolved. After a short cooling period, 3 μ L of SYBERSAFE was added and gently swirled to ensure uniform distribution. The gel solution was carefully poured into a chamber fitted with a 1.5 mm comb and allowed to polymerise at room temperature, ensuring the absence of air bubbles. Once solidified, the gel was placed in an electrophoresis chamber and immersed in 1 x TAE buffer. Subsequently, 10 μ L of sample mixed with 3 μ L of 6 x loading buffer was loaded into the wells of the gel. Gel electrophoresis was performed at 75 mAmps and 100 V. Finally, the bands were visualised and recorded using a UV transilluminator and LYCOR software for analysis.

3.4.10 Immunofluorescence Staining

For immunofluorescence (IF) staining, cells were seeded onto PLO/laminin-coated μ -Slide 8-well chamber slides or coverlips at a density of 50,000 cells per cm^2 . The cells were washed with DPBS and fixed with 4% paraformaldehyde solution for 15 minutes at room temperature. After washing the cells three times with DPBS, the cell membrane was permeabilized by incubating the cells with 0.2% (v/v) TritonX-100 in DPBS for 10 minutes at room temperature. The cells were incubated with Pierce™ Protein-Free Blocking Buffer (see Table 3.3) for 1 hour at room temperature to block non-specific binding sites. The primary antibodies were then added to the blocking buffer at an appropriate dilution and the cells were incubated with this solution at 4°C overnight. The next day, the cells were washed three times for five minutes with DPBS. Finally, secondary antibodies were diluted in blocking buffer and added to the cells. The cells were incubated for one hour at room temperature in the dark. The cells were washed with DPBS three times for five minutes each. After staining, the samples were mounted with DAPI Fluoromount G and stored at 4°C until further use. Staining was analysed using an LSM900 laser scanning microscope and evaluated using the supplied ZEN application software for observation.

3.5 Differentiation of iPSCs into neural progenitor cells (NPCs)

3.5.1 Cultivation of neural progenitor cells

Neural progenitor cells (NPCs) were cultured in proliferation medium on PLO/laminin-coated cell culture plates and passaged twice a week. Prior to passage, cells were washed with 1 ml of Hank's buffered salt solution (HBSS) per well of a 6-well plate. The cells were then detached from the plate surface by adding 0.7 mL of Accutase and incubated at 37°C for 5 minutes. The enzymatic reaction was stopped by adding 1 mL of proliferation medium, the cells were transferred to a centrifuge tube and centrifuged at $300 \times g$ for 5 minutes. The supernatant was then removed, the cells were resuspended in proliferation medium and the cell number was determined using the CellDrop cell counting system. For permanent culture, 1.0×10^6 cells were added to each of the six wells of a plate containing 1.5 ml growth medium.

3.5.2 Cultivation of neural differentiated cells

For differentiation into neural differentiated cells (NDCs), NPCs were seeded at a lower density than when cultured in differentiation medium. The number of cells used per cell culture vessel is summarised in the table 3.24. The differentiation medium was changed twice a week for six weeks.

Table 3. 24: Seeding parameters of neural differentiated cells

culture vessel	Cell count	Volume medium (ml)
6-well	4.0×10^5	1.5
12-well	1.5×10^5	1
24-well on coverslips	9.0×10^4	0.5

3.5.3 Differentiation of iPSCs into neural progenitor cells (NPCs)

The neural cell model, consisting of a mixed culture of neurons and glial cells, was generated from the iPSCs via the intermediate stage of NPCs. The iPSCs were cultured on PLO/laminin-coated plates in Neural induction medium supplemented with 5 ng/ml FGF2, 20 μ M SB-431542 and 1 μ M LDN193189 for two weeks to achieve density-induced differentiation leading to the formation of neural rosettes containing NPCs. After two weeks these cells were then separated using the neural surface marker PSA-NCAM (polysialic acid neural cell adhesion molecule). The undifferentiated stem cells were mechanically extracted using a glass hook, while the neural rosettes were rinsed with 1ml HBSS and later isolated with 1ml Accutase. The enzymatic reaction was stopped after 10 minutes by the addition of proliferation medium, followed by

centrifugation of the cells at $300 \times g$ for 5 minutes. Cells were suspended in 10 mL of proliferation medium and their number was counted using the CASY cell counter. NPCs were purified using the Anti-PSA-NCAM MicroBead Kit (Miltenyi Biotec GmbH, Bergisch Gladbach, DE) according to the manufacturer's instructions. The method uses anti-PSA-NCAM antibodies attached to magnetic beads that bind to this surface marker on NPCs. The NPCs are suspended in the magnetic column and can be eluted later. The cells were first resuspended in MACS buffer (60 μ l). The cell suspension was then incubated for 10 min at 4°C, after which FcR blocking reagent (20 μ l) was added. This was followed by a further incubation at 4°C for 15 min, after which anti-PSA-NCAM microbeads (20 μ l) were added. The cells were washed with 2 ml buffer, centrifuged at $300 \times rpm$ for 5 min and then resuspended in 1 ml buffer. Magnetic separation was performed by inserting the MS column into the MACS Multi Stand and equilibrating with 500 μ l of buffer solution. The cell mixture was introduced into the column and as it passed through, the PSA-NCAM + cells were selectively bound. The unlabelled PSA-NCAM cells were then washed three times with 500 μ l of buffer. The PSA-NCAM + cells were harvested by removing the column from the magnet and transferring it to a centrifuge tube. After adding 1 ml of proliferation medium and quickly placing the tube on the column, the cells were suspended and collected. Finally, the number of cells in the PSA-NCAM + fraction was calculated and seeded in proliferation medium at a concentration of 1.0×10^6 cells per well of a six-well plate. PSA-NCAM + NPCs were cultured and cryopreserved. Neural differentiation was achieved by plating NPCs at a low density of 0.4×10^5 cells/cm² and allowed to progress for six weeks.

3.6 Differentiation of iPSCs into Oligodendrocyte progenitor cell (OPCs)

3.6.1 Cultivation of oligodendrocyte progenitor cells and Oligodendrocyte

The iPSCs were seeded onto Matrigel matrix coated plates and the mTeSR medium was replaced by Neural Induction Medium (NIM) supplemented with SB431542 and LDN193189. After five days in the medium, RA and a sonic hedgehog agonist (SAG) were added. The cells were then cultured for a further four days, with the medium changed daily. On the ninth day of neural induction, the cells were passaged with Accutase and seeded onto Matrigel-coated plates. After transfection with lentivirus, the OPCs were cultured in OLs differentiation medium supplemented with the growth factors listed in Table 3.5. The medium was changed every other day for ten days.

3.6.2 Differentiation of iPSCs into Oligodendrocyte progenitor cell (OPCs)

Oligodendrocytes were generated from iPSCs using SOX10 TF (transcription factor)-mediated differentiation supported by signaling molecules and growth factors (Juan Garcia Leon et al., 2020). TF-mediated differentiation improved the efficiency and time required to generate functional OLs from iPSCs. The protocol was developed in several steps: generation of inducible lentiviral plasmids containing SOX10, differentiation into OLIG2⁺ precursors and finally functional OL from iPSCs (Figure 6).

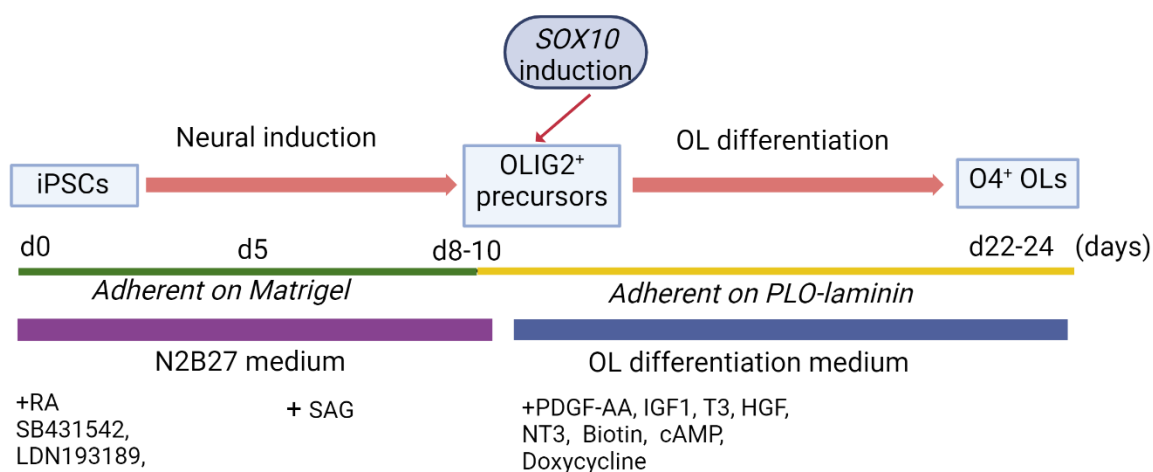


Figure 6: Timeline of O4⁺ oligodendrocyte generation

3.6.3 Reproduction of lentivirus vectors

The genetic material (plasmid DNA) was replicated using bacteria. First, the plasmid was introduced into competent *E. coli* cells by bacterial transformation. Second, the amplified plasmids were obtained by isolating them from the transformed bacterial cells during plasmid preparation. To transform the plasmid DNA into chemically competent *E. coli* bacteria, 50 μ l of *E. coli* cells were thawed on ice. Then 1 μ l of plasmid DNA at a concentration of 50 ng/ μ l was added to the cells. The mixture was incubated for 20 minutes on ice. The plasmid DNA was introduced by a heat shock process at 42°C for 40 seconds. This method briefly rendered the bacterial cell wall permeable. The bacterial suspension was then incubated again on ice for five minutes. The bacterial suspension was then incubated in 500 μ l of LB medium for one hour. Then 50 μ l of the bacterial suspension was plated onto a pre-warmed 10 cm cell culture dish containing LB agar and ampicillin (100 μ g/ml) and incubated overnight at 37°C. Plasmids carrying ampicillin resistance allowed bacteria that had taken up the plasmid to resist ampicillin and therefore be selected. Three bacterial colonies were selected for preculture and transferred

to test tubes containing LB Amp medium, followed by incubation at 37°C for 10 hours. On completion, the precultures were completely transferred to 100 ml of LB Amp medium, resulting in the main cultures. After incubation at 37°C for 18 hours, bacterial cells were pelleted at 300× rpm at 4°C for 15 minutes and then stored at -20°C until further use. Plasmid isolation from transformed bacteria was performed using the Qiagen Plasmid Maxi Prep Kit according to the manufacturer's guidelines. Cell lysis was performed first, followed by precipitation and centrifugation of genomic DNA. After these steps, the resulting supernatant containing the plasmid DNA was collected. This supernatant was then purified by filtration using a supplied column and eluted. The plasmid DNA obtained was precipitated with isopropanol and then centrifuged (1500x rpm, 30 min, 4°C), followed by washing with 70% ethanol and another round of centrifugation (1500 x rpm, 10 min, 4°C). The resulting pellet was air dried at room temperature and dissolved in 100 µl Tris-EDTA (TE) buffer. The concentration was determined by measuring the absorbance using a microvolume spectrophotometer (TECAN Spark) at 260 nm. For this procedure, 2 µl of sample material was pipetted onto a NanoQuant™ plate and measured. The absorbance at 280 nm was also determined and the ratio 260 nm/280 nm was calculated. Plasmid DNA with a purity of 260 nm/280 nm < 2.0 was used. The viral vectors were stored in 50 µl aliquots at -20 °C until further use.

3.6.4 Lentivirus virus generation

Virus vectors, viral proteins and enzymes (vesicular stomatitis virus glycoprotein G (VSV-G) and packaging plasmid (psPAX2) were used for virus production. For this purpose, 3.0 x 10⁶ HEK293T cells were seeded on two 10 cm cell culture dishes in basal medium without penicillin/streptomycin, cultured overnight at 37 °C, 5 % CO₂ and 90 % relative humidity, and then transfected. In two separate 1.5 ml tubes, 180 µl of optiMEM Reduced Serum Medium was mixed with 20 µl of Lipofectamine 2000 and incubated for 5 minutes at room temperature. In a 1.5 ml Eppendorf tube, 1.8 µg packaging plasmid (psPAX2), 0.2 µg envelope plasmid (VSV-G) and 2 µg SOX10 vector were mixed, while for mtFUW vector production, the same procedure was repeated in another 1.5 ml Eppendorf tube, but instead of SOX10 vector, 2 µg mtFUW vector was mixed with packaging and envelope plasmids. After incubation for 5 minutes, Lipofectamine 2000 in optiMEM was added to the mixture of 2 µg viral vector DNA SOX10 and 2 µg viral vector DNA mtFUW and incubated for a further 20 minutes at room temperature. The transfection mixture was then added dropwise to HEK293T cells seeded on two dishes and incubated in an incubator at 37°C for 18 h. The medium was then replaced with

10 ml of basal medium without penicillin/streptomycin and incubated for a further 48 h. The viruses were then harvested from the supernatant. For this purpose, the cell supernatant was filtered sterile (pore size of the filter 0.45 μm) and stored in centrifuge tubes at 80 °C.

3.6.5 Titer determination

Successful programming requires optimal transduction efficiency. Therefore, the titre was determined separately for each virus. The percentage of transfected cells could be determined based on the GFP-positive cells and by flow cytometry to calculate the transduction efficiency. For this purpose, 1.0×10^5 HEK293T cells were seeded per well of a 12-well plate in 1 ml base medium. Different volumes of virus (0.5 ml - 3.5 ml) were added to determine the volume for optimal transduction efficiency. After 48 hours of incubation, the supernatant was removed and the cells were lysed by adding 200 μl of 0.05% trypsin EDTA per well and incubating at 37°C for 5 minutes. The enzymatic reaction was stopped with 1 ml of base medium, the cells were transferred to a centrifuge tube and centrifuged at 300 rpm g for 5 min. The supernatant was aspirated and the cells were fixed by shaking in 200 μl 2% PFA for 15 min. The cells were then centrifuged again (3,000 x g, 5 min) and the pellet was resuspended in 500 μl wash buffer. Using the FACS Calibur flow cytometer, transduction efficiency was determined for each virus dose based on the proportion of GFP-positive cells in the total cell count measured and calculated using MOI-1 as following. The titration and calculation were performed for rtTA, respectively. Evaluation was performed using CellQuest Pro software.

Table 3.5: Calculate the required amount of viral vector

FUW-SOX10		
μL virus per mL	% GFP+ cells	Dilution (1:5)
20	82.21	0
4	42.63	-1
0.8	11.28	-2
0.16	3.78	-3
0.032	0.66	-4

MOI of 1 = 9.71 μL

3.6.6 Differentiation of iPSCs into OLIG2+ precursors

The first step in the primary process is to induce neural differentiation in iPSCs. To achieve this, iPSCs were dissociated into single cells using Accutase and then plated at a density of 20,000 cells/cm² on Matrigel coated plates in mTESR1 medium supplemented with ROCKi.

After two days, when the cell culture had reached 70% confluence, it was supplemented with N2B27 medium containing two small molecule inhibitors of the SMAD pathway (SB431542 and LDN193189) in addition to low concentrations of RA (100 nM). This results in the efficient production of neurons that form rosettes. On day 5, a sonic hedgehog agonist (also known as smoothed agonist or SAG) was added. The addition of SAG resulted in a significant proportion of OLIG2⁺ cells after only 8 days of neural induction. The cells were then dissociated into single units using Accutase and plated on PLP/laminin-coated plates at a density of 50-75,000 cells/cm² in N2B27 medium supplemented with ROCKi.

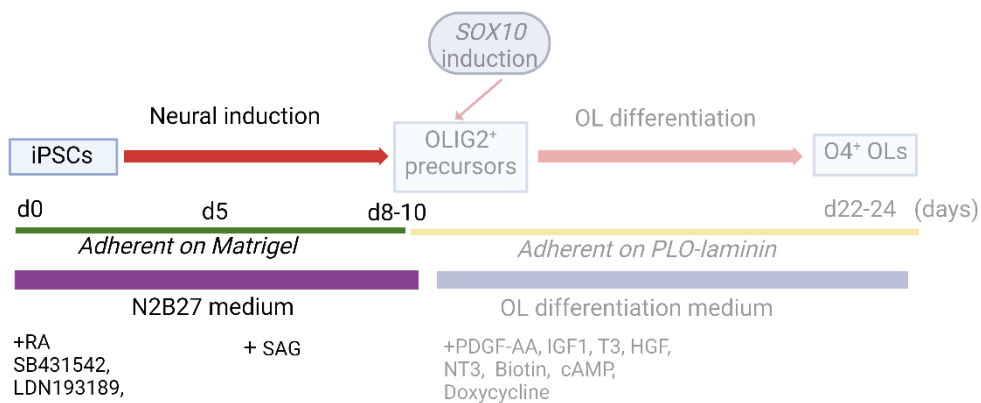


Figure 7: Timeline of O4⁺ oligodendrocyte generation. Neural induction of OLIG2⁺ precursors.

3.6.7 Derivation of OPCs from iPSCs

After 8 days of neural induction, the cells were treated with an N2B27 lentiviral vector encoding the SOX10 coding sequence described previously at 3.5 section. The cells were then transduced by adding the viral vectors FUW-SOX10 and rtTA at a MOI of 1 using a diluted and calculated volume. The viral vector was added to fresh medium identical in composition to the previous step. The old medium was then replaced with the diluted fresh medium containing viral vectors and added to the cells. After 24 hours of viral transduction, the cells were washed with RT-PBS and the lentivirus-containing medium was removed. The cells were cultured in OL differentiation media supplemented with 1 µg/ml doxycycline to induce SOX10 expression. The complete medium was replaced on alternate days for a period of 10 days. After 10 days of differentiation, the cells were either purified for coculture or collected for further experiments. After total 24 days of OL generation, the cells exhibited a mature OL phenotype. The O4⁺ markers were present in 55-70% of the cell population and an additional 20% of these cells expressed mature OL myelin proteins.

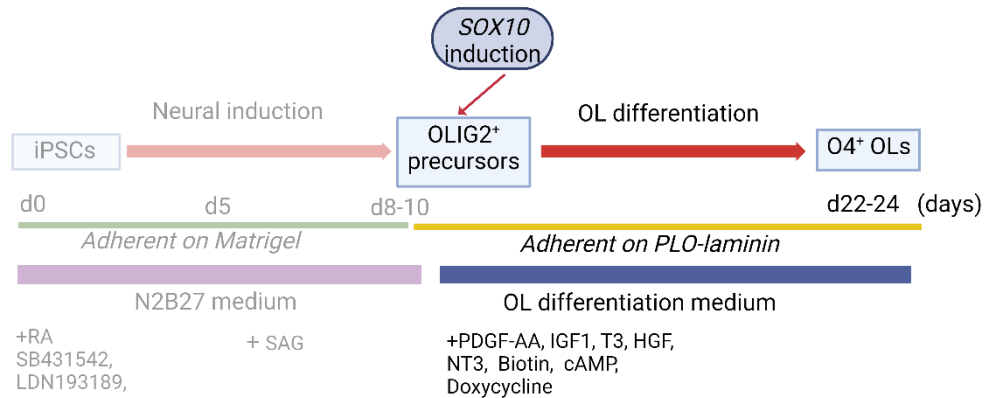


Figure 8: Timeline of O4+ oligodendrocyte generation. OLIG2+ precursor cells were transduced with a lentiviral vector encoding the SOX10 coding sequence and cells were cultured in OL differentiation media supplemented with 1 $\mu\text{g/ml}$ doxycycline with full media changes every other day for period of 10 days.

3.6.8 O4-based purification

To obtain purified OLs or O4+ cells, the differentiated OLs were purified. Anti-O4 microbeads (see Table A.3) were used to purify the cells, according to the manuscript recommendations, the old medium was removed and set aside, and 1 ml of pre-warmed Accutase was added to one well of a six-well plate and the plates were incubated for 10-15 min until most of the cells were detached. To stop the enzymatic reaction, the previous medium was added and the cell clumps were disrupted into a single cell suspension by pipetting up and down four to five times with a 1 ml pipette. The cells were collected in a Falcon tube and centrifuged at 300g for 5 minutes at RT. The cell pellet was then resuspended in 90 μl of ice-cold MACS buffer per 1×10^7 . To the cell suspension, 10 μl of O4 microbeads were added, mixed well and incubated for 15 min at 4°C in the refrigerator. The cell suspension was washed by adding 5 ml of cold MACS buffer and centrifuged at 300 g for 5 min. After centrifugation, the cell pellet was resuspended in 1 ml of cold MACS buffer. The cell suspension was filtered through a 40 μm pre-wetted nylon filter to eliminate cell clumps that could interfere with the cell separation process. Simultaneously, the LS column was placed in a MACS separator and rinsed with 3 ml of cold MACS buffer to ensure optimal flow and separation. Once all the buffer had passed through the column, the filtered cell suspension was introduced and allowed to pass through the entire column. The washing process was repeated three times using 3 ml of MACS buffer each time, allowing the column reservoir to empty after each step. After washing, the column was removed from the separator and placed in a sterile 15 ml Falcon tube. 5 ml of MACS buffer was added to the column and the magnetically labelled cells were immediately washed out by firmly pressing the plunger into the column. The eluted cells represent the O4+ enriched cell population. The cells were centrifuged at 300g for 5 minutes. The cell pellet was then resuspended in 1 ml OL induction medium or coculture medium as required.

3.6.9 Checking the purity of O4 expression in a small fraction of the O4+ cells by FACS

To check the purity of O4 expression by FACS, a small aliquot of cells (50,000–100,000 cells) was taken. To assess O4 purity and determine cell count (collected O4+ cells are typically ~10% of the starting population), the cell pellet was resuspended in 1 ml of OL induction medium with ROCK inhibitor. First, the cell aliquot was resuspended in 95 μ l of ice-cold MACS buffer, then 5 μ l of O4-APC antibody was added and incubated for 15 minutes in the refrigerator. The cells were washed with 2 ml of MACS buffer, centrifuged, resuspended in 200 μ l of MACS buffer, and then analyzed on a flow cytometer. Appropriate isotype or unstained control samples were used to define gate thresholds.

3.7 Coculture of maturing iPSCs-derived neurons and O4+ OLs

3.7.1 Cultivation of Coculture

Coculture of OLs and neurons was executed by merging neurons, produced as delineated in section 3.4, with OLs, generated per the instructions outlined in section 3.5, in a six-, twelve-, or 24-well plate utilizing coculture medium enriched with doxycycline for a duration of four days. Following this period, the doxycycline was withdrawn, and the medium was refreshed every two weeks for an additional four to six weeks. Subsequently, the cells were utilized for testing purposes.

3.7.2 Coculture of maturing iPSCs-derived neurons and O4+ OLs

To establish a coculture of neurons and OLs, it was necessary to use purified O4+ OLs and mature neurons (Figure 9). It was necessary to obtain mature neurons and OLs expressing myelin proteins at the same time in order to obtain the myelination process. Therefore, NDC differentiation was initiated several weeks earlier. When both cell types were obtained, the old NDCs medium was replaced with coculture medium supplemented with 1 μ g/ml doxycycline, 1 \times ROCKi and 10 μ g/ml laminin. The cells were then seeded on mature neurons at 50,000 O4+ cells/cm². The cells were incubated at 37°C for four days without disturbance. Doxycycline was then removed from the coculture medium. The cells were cultured for a further 20-25 days, with partial medium replacement two or three times a week by gently replacing half the medium with fresh medium. Laminin at a concentration of 10 μ g/mL was added during the medium changes to prevent cell detachment. At the end of the coculture period, the medium was discarded and the cells were rinsed with PBS. The cells were then fixed with 4% (wt/vol) PFA for 10 minutes at room temperature.

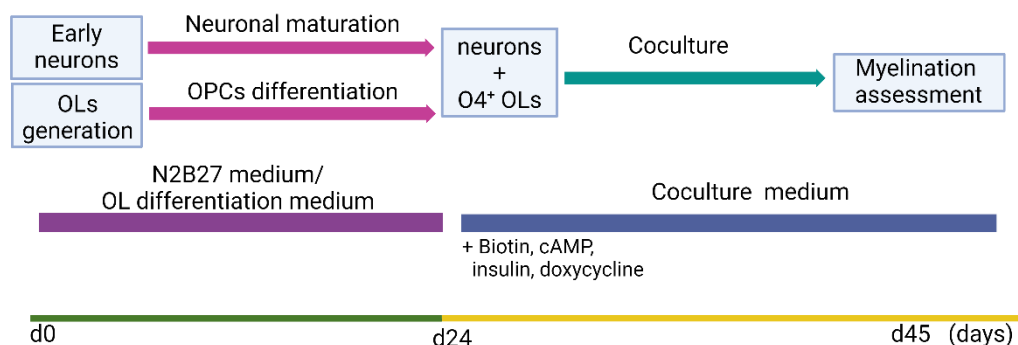


Figure 9: Timeline of coculture generation. Coculture between OLs and neurons to quantify the effect of candidate compounds on myelin production

3.8 Protein Isolation and Western Blot

3.8.1 Protein isolation

To harvest the total protein fraction, cells grown in a 6-well plate were washed once with PBS, then PBS was removed and 90-200ul of cold activated RIPA buffer supplemented with complete Protease Inhibitor Cocktail tablets and PhosSTOP Phosphatase Inhibitor tablets was added (Table 3.2). Cells were scraped from the surface of the dish with a scraper and incubated on ice with RIPA buffer on a shaker for 20 minutes. The cell suspension was then centrifuged at 13,000 x g for 15 minutes at 4°C. The protein-containing supernatant was transferred to a fresh tube and stored at -80°C. Alternatively, cells were collected in pellets by centrifugation and frozen at -80°C, then these pellets were suspended in 90-200ul of activated RIPA buffer and incubated on ice with shaking for 40-60 minutes. The samples were then centrifuged at 13,000 x g for 15 minutes at 4°C. The supernatant was collected and stored at -80°C.

3.8.2 Protein concentration measurement

To measure the protein concentration in the prepared samples, the Pierce BCA Protein Assay Kit (Table 3.3) was used according to the manufacturer's instructions. First, samples for the standard curve were prepared by diluting 2 mg/ml BSA stock solution with water to the concentration range between 0 and 10 µg/ml. Next, the protein samples were diluted 5 times with water. Then 10 µL of protein samples and standard curve samples were pipetted in triplicate into a 96-well plate and 200 µL of BCA reagent was added to each well. A blank was prepared by mixing 10 µl RIPA buffer and 200 µl BCA reagent. The plate was then incubated for 30 minutes in the dark at 37°C with shaking at 300 rpm. Colorimetric measurement was performed using a microplate reader at a wavelength of 570 nm. The protein concentration was calculated using the standard curve method.

3.8.3 Gel preparation

For Western blot gels, the glass plates for the mini-gel were inserted into the gel frame - both thick and thin glass. The frame was secured to prevent liquid spillage. The components listed in Table 3 were used to prepare the 15% gel according to the following protocol: 1.5M Tris, pH 8.8, 10% SDS, 10% APS and 40% Rhotiphorese Gel 40 solution were added to ultrapure water. The solution was vortexed briefly before the addition of TEMED to thicken the gel. After a short vortex, the mixed solution for the 15% polyacrylamide-SDS running gel was loaded between the glass plates for the mini-gel. Then 1 mL of isopropanol was added to the 15% polyacrylamide-SDS solution to remove bubbles and flatten the gel. The gel was then allowed to solidify for 15 minutes at room temperature. Meanwhile, the reagents for the 4% polyacrylamide-SDS stacking gel were prepared as indicated in Table 3. Finally, TEMED was added to the mixture. When the gel had set, the isopropanol was removed and the 4% polyacrylamide-SDS stacking gel was placed on top of the 10% polyacrylamide-SDS running gel. The composition was immersed in the liquid 4% polyacrylamide-SDS solution and incubated for 20 minutes at room temperature. The gel was then gently removed from the frame and used immediately or stored in 1% electrophoresis buffer at 4°C for one week.

Table 3.26 4% polyacrylamide-SDS stacking gel

Name	Amount
VE water	1.3 mL
40% solution Rhotiphorese gel 40	0.2 mL
0.5 M Tris, pH 6.8	0.5 mL
10% SDS	20 µL
TEMED	2 µl
10% APS	20 uL

Table 3.27 15% polyacrylamide-SDS stacking gel

Name	Amount
VE water	1.723 mL
40% solution Rhotiphorese gel 40	1.875 mL
1.5 M Tris, pH 8.8	1.3 mL
10% SDS	50 µL
TEMED	2 µL

10% APS	50 μ L
---------	------------

3.8.4 Western Blot

To prepare Western blot samples, the volume of protein sample containing 20 μ g of total protein was mixed with 6 μ l of 5X SDS loading buffer (0.25% bromophenol blue, 0.5M dithiothreitol, 50% glycerol, 10% SDS and 0.25M Tris-HCl pH 6.8) and made up with water to a final volume of 30 μ l. The 15% polyacrylamide gel was loaded into a Criterion Electrophoresis Cell and the cell was filled with SDS running buffer (25 mM Tris, 0.2 M glycine, 0.01% SDS). The samples and the Protein Plus Marker (Table 3.7) were pipetted onto the gel and electrophoresis was performed at 100 V for 10 minutes and then at 200 V for 45 minutes. The gel was then removed from the cast and a transfer stack was built using Trans-Blot Turbo Midi Nitrocellulose Transfer Packs (Table 3.1) according to the manufacturer's instructions. The stack was placed in the Trans-Blot Turbo Transfer System and the transfer was performed for 7 minutes at 25 V and 1.3 A. Once the transfer was complete, the membrane was dried for 1 hour to allow the protein to bind tightly to the membrane and prevent potential signal loss. The membrane was then incubated in blocking buffer (5% skimmed-milk powder in TBS-T buffer: 20 mM Tris, 137 mM NaCl, 0.1% Tween 20, pH 7.5) for 1 hour at room temperature with gentle shaking. The appropriate primary antibody dilution was prepared in 3% skimmed milk in TBS-T buffer and, after the blocking step, the membrane was incubated with this solution overnight at 4°C with gentle shaking. The next day, the membrane was washed 3 times for 5 minutes with TBS-T buffer. The membrane was then incubated with an appropriate dilution of secondary antibody prepared in 3% skimmed milk in TBS-T for 1 hour at room temperature with gentle shaking in the dark. The membrane was then washed three times for 5 minutes with TBS-T buffer and once for 5 minutes with TBS buffer without Tween 20. Depending on the secondary antibodies and detection system used, the membrane was either allowed to dry and then immunofluorescence was detected using the Odyssey 9120 Fluorescence Imager. The immunofluorescence images were analysed and quantified using Image Studio Lite software.

3.9 Quantifications and Statistics

The statistical evaluation of the gathered data was meticulously performed using GraphPad Prism, version 8.0.1. We meticulously present all findings as the mean \pm standard deviation (SD), ensuring each is derived from a minimum of three separate experiments to guarantee robustness and reliability. To verify the normal distribution of our datasets, the Shapiro-Wilk test was employed as a rigorous measure of normality. For the analysis involving the

comparison of two distinct means, the unpaired Student's t-test was judiciously selected. In scenarios necessitating the examination of more than two means, a one-way ANOVA was conducted. Should significant disparities emerge, the Dunnett post hoc test was systematically applied for detailed pairwise comparisons, ensuring a comprehensive understanding of the data. In cases where datasets did not adhere to a normal distribution, the nonparametric Kruskal-Wallis test was utilized, a testament to our adaptive approach to statistical analysis. Dunn's post hoc test served as the subsequent step for comparisons, embodying our commitment to thorough and precise statistical examination.

Statistical significance was determined with a stringent threshold: a p-value of ≤ 0.05 . We denote levels of significance as follows to ensure clarity and ease of interpretation: $p \leq 0.05$ is indicated by */#, $p \leq 0.01$ by **/##, and $p \leq 0.001$ by ***/###. This nuanced approach underscores our dedication to rigorous scientific standards and the importance we place on the accuracy and significance of our findings.

3.9.1 Colocalization Analyses

Visual inspection and recording of stained cells for colocalisation analyses was performed on the LSM 900 using ZEN imaging software. Ten randomly selected image sections were recorded per coverslip, i.e. per independent experiment. Colocalisation was evaluated using ImageJ and the JaCOP (*JustanotherColocalisationPlugin*) application. Pearson's correlation coefficient (PCC), which indicates the strength of a linear relationship between two fluorescence intensities from the superimposition of two images, was determined for this purpose. The PCC can take values between -1 (100% inverse colocalisation) and 1 (100% positive colocalisation). Values close to zero reflect distributions of samples that are not correlated. The PCC can be mathematically formulated as follows (Dunn et al. 2011):

$$\text{PCC} = \frac{\sum_i (R_i - \bar{R}) \times (G_i - \bar{G})}{\sqrt{\sum_i (R_i - \bar{R})^2 \times \sum_i (G_i - \bar{G})^2}}$$

where R_i and G_i are the red and green channel intensities of pixel i , respectively; and \bar{R} and \bar{G} are the arithmetic mean of all red and green channel intensities in the entire image.

4 Results

4.1 Generation and characterization of iPSC line

The main objective of this thesis was to establish a FAHN iPSCs cell model to analyse the disease-related pathologies within neurons and OLs that are specifically affected in FAHN, respectively. The starting material for the generation of iPSCs were patient-derived fibroblast cells. The iPSCs control cell line was generated and characterized by Dr. Christin Volkner (work group “Cellular Neurophysiology”) (Völkner et al. 2019). To generate the control neuron and astrocyte cell lines, iPSCs were differentiated into NPCs using the modified protocol published by Peter et al. (Peter et al. 2017).

In addition to the existing control iPSC line, we generated and characterised one further iPSC line. This cell line is a female *FA2H*-deficient cell line from a patient with the combined heterozygous *FA2H* mutation (c.133G>A and c. 956A>G, see Table 3.1), and it was described in detail by Efendic et al. (Efendic et al. 2022). The iPSCs were generated by transduction of patient-specific fibroblasts with the transcription factors *KOS* (*KLF*, *SOX2* and *OCT4*), *KLF4*, and *c-MYC* using a non-integrating Sendai respiratory virus approach. The fibroblasts underwent morphological changes approximately one to two weeks after transduction. These changes resulted in the formation of elongated cell bodies, as shown in Figure 6, and an increase in the number of smaller, rounded cells (Figure 10 B). The cells subsequently formed larger colonies with clearly defined edges (Figure 10 C). The colonies consisted of densely packed cells with a high nuclear-to-cytoplasm ratio (Figure 10 C, *). The cells were initially expanded individually on feeder cells and subsequently on Matrigel (Figure 6 D).

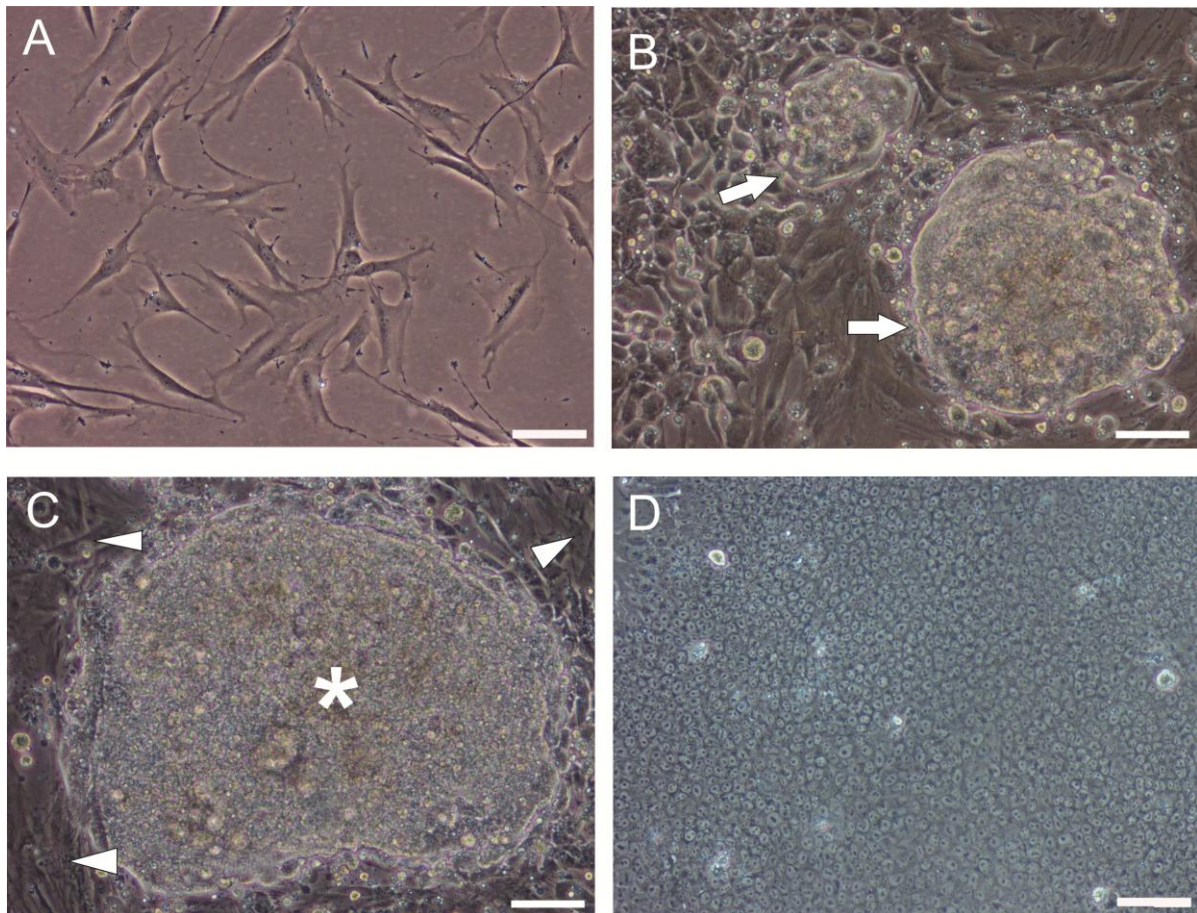


Figure 10: Reprogramming of fibroblasts into iPSCs via Sendai virus. (A) Initial state of fibroblasts before transduction, showing their standard morphology. (B) Approximately one week after transduction, fibroblasts show altered characteristics with more compact and rounded cell bodies, indicated by arrows. (C) At 18 days post-transduction, a round iPSC colony (*) is observed surrounded by fibroblasts that are either non-reprogrammed or incompletely reprogrammed. A fully reprogrammed iPSC colony (*) is shown. (D) iPSCs are maintained and expanded in the mTeSR medium on Matrigel coated plates. Scale bar is 100 μ m.

4.1.1 Evidence of pluripotency

After the establishment phase of stable iPSC line, pluripotency was assessed. Qualitative detection of AP was performed by staining. The presence of AP activity was indicated by the characteristic dark purple colouring of the iPSCs colonies, while the surrounding differentiated feeder cells appeared colourless (Figure 11). In addition, pluripotency-associated proteins were analysed by immunohistochemical staining. These included the transcription factor octamer binding transcription factor 4 (OCT4) and the divergent homeodomain protein NANOG, as well as the stage-specific embryonic antigen 4 (SSEA4) and the keratan sulphate proteoglycans tumour rejection antigen (TRA-1-60 and TRA-1-81), which are expressed on the surface of pluripotent stem cells. Immunofluorescence staining revealed that the iPSCs were positive for

the pluripotency markers NANOG and SSEA4 (Figure 11), as well as OCT4, TRA-1-60 and TRA-1-81 (Appendix, Figure 32). The transcription factors *OCT4* and *NANOG* are stained and localised in the nucleus, whereas the surface markers *SSEA4*, *TRA-1-60* and *TRA-1-81* are detected in the cell membrane (see Figure 11 and 32 respectively).

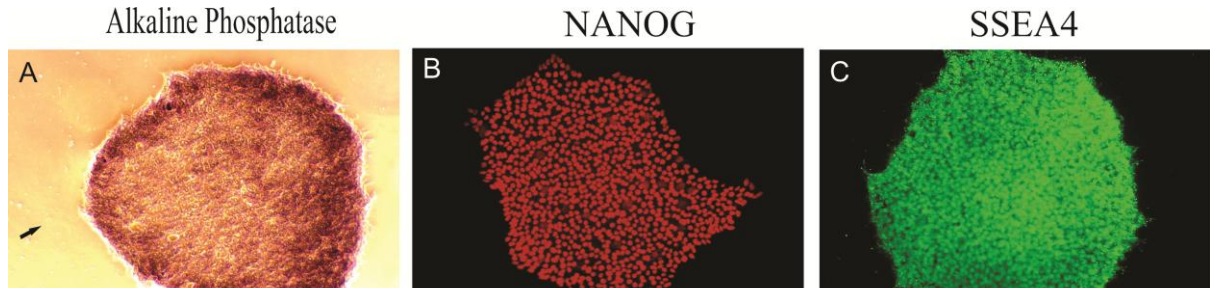


Figure 11: Detection of pluripotency markers in the established iPSC line. (A) The iPSC colonies show a dark purple colour, indicating AP activity in undifferentiated stem cells. In contrast, the surrounding feeder cells appear colourless (indicated by arrows). **(B and C)** Immunofluorescence detection of the pluripotency markers NANOG (red) and SSEA4 (green) is also visible. Scale bar is 100 μm .

To quantitatively analyze the same pluripotency-associated proteins, we used flow cytometry with corresponding fluorescence-coupled primary antibodies. Figure 8 displays histograms of an intracellular marker (NANOG) and an extracellular pluripotency marker (SSEA4) for iPSC line (Figure 12). The representation of the pluripotency markers OCT4, TRA-1-60, and TRA-1-81 can be found in the appendix (Figure 33). The quantification revealed that nearly all cells of the iPSC line expressed the respective pluripotency markers (A: NANOG 98.0%; OCT4 94%; SSEA4 97%, TRA-1-60 94%; TRA-1-81 93%).

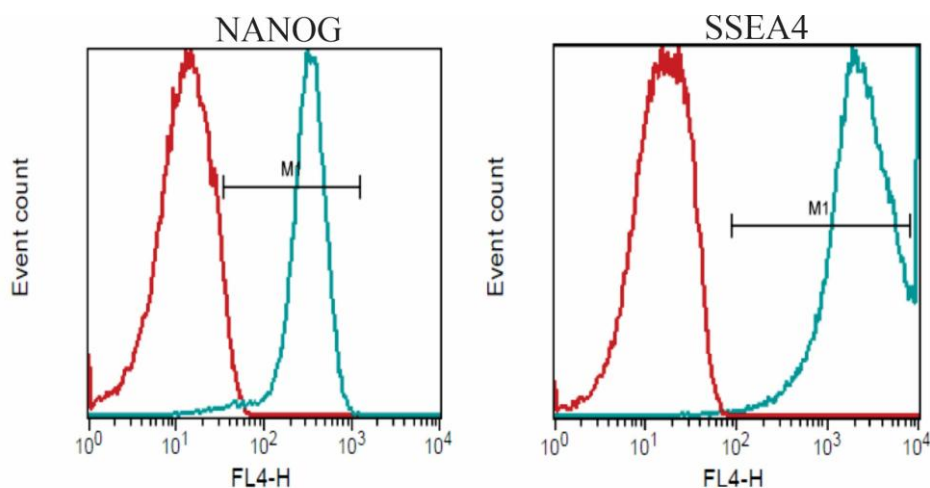


Figure 12: Analysis of pluripotency-related proteins via flow cytometry. The histograms showcase the relative fluorescence intensities of NANOG and SSEA4 proteins within the FAHN iPSC line, juxtaposed with the event count. The baseline, represented by an unstained control, is illustrated in red, while the fluorescence increase post-primary antibody staining is highlighted in blue.

Semiquantitative RT-PCR was used to detect the expression of endogenous pluripotency-associated genes. The following marker genes were analysed *OCT4*, *NANOG*, *SOX2*, *KLF4*, *c-MYC*, *hTERT*, *ZFP296*, *FGF4* and *ESG1*. The primers were designed to specifically detect only the endogenous transcripts. Figure 9 shows that all endogenous pluripotency markers were detected in the FAHN iPSC line, whereas the original fibroblast cells were mostly negative. An exception is the presence of strong endogenous expression of the genes *KLF4*, *c-MYC* and *ZFP296* in fibroblasts, especially for *KLF4* and *c-MYC*. This has been demonstrated in several other studies (Takahashi et al, 2007) and suggests that these markers are not specific.

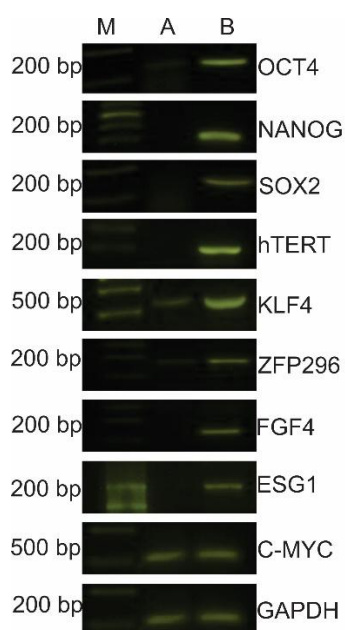


Figure 13: Detection of pluripotency-associated genes using RT-PCR. The comparison between the expression of pluripotency-associated genes in fibroblasts (A) and FAHN iPSCs (B) reveals that the iPSCs expressed all tested pluripotency markers, while the fibroblasts were mostly negative. The housekeeping gene *GAPDH* was used as a reference. The size of the amplified PCR products can be determined using the marker (M) (see Table A.7).

4.1.2 Analysis of transgene expression using RT-PCR.

Another feature of fully reprogrammed iPSCs characterisation is the inactivation of transgenes after the activation of endogenous pluripotency-associated genes (see Figure 10), a process also known as 'gene silencing'. Semi-quantitative RT-PCR was used to examine the transcripts of the transgenic reprogramming factors *KOS* (*KLF*, *SOX2* and *OCT4*), *KLF4*, and *c-MYC* and Sev viral DNA in the FAHN iPSC line at passage 7 and passage 12. The study found that transgenic reprogramming factors were detected at passage 7, but by passage 12, no transgenic reprogramming factors and Sev viral DNA were present in the iPSCs, indicating complete reprogramming of the iPSCs (see Figure 14).

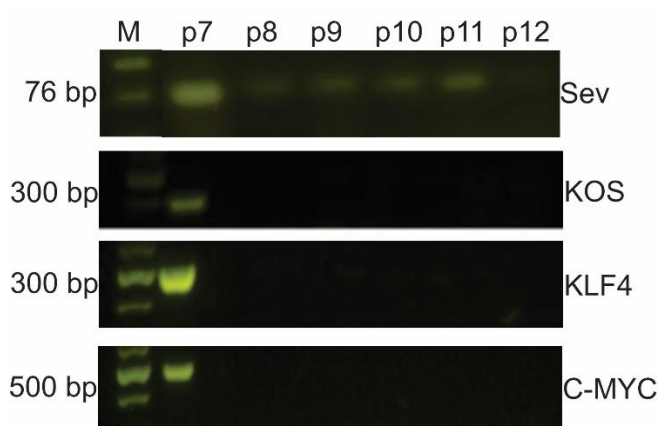


Figure 14: Results of the RT-PCR expression analysis of the transgenes. At passage 12 (P12), the FAHN iPSC line did not express the *KOS*, *KLF4* and *c-MYC* transgenes and there is no trace of viral DNA fragments. Passage 7 (p7) was used as a positive control. The size of the amplified PCR products can be determined using the marker (M) (see Table A.7)

4.1.3 *In vitro* trilineage differentiation potential of iPSCs

Next, EBs were generated from iPSC clones. These EBs then underwent spontaneous differentiation into the three germ layers: endoderm, mesoderm, and ectoderm, over a period of

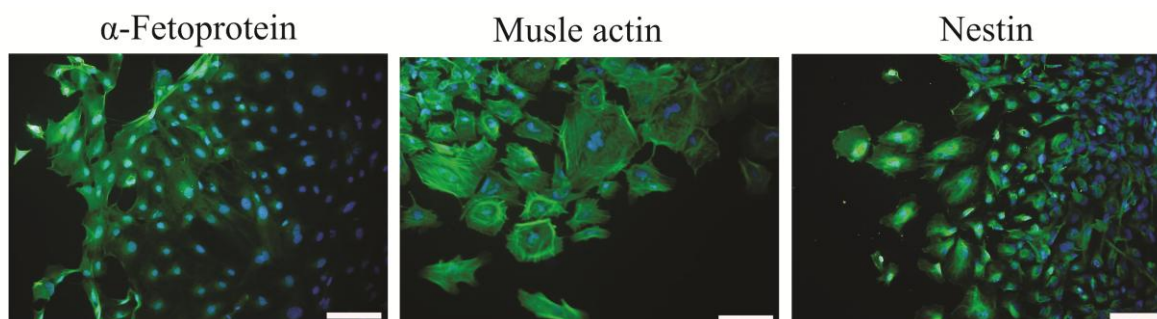


Figure 15: The iPSCs clones spontaneously differentiated into cell types representative of the three germ layers, serving as a confirmation of the pluripotent state of the gene-edited iPSCs. Both clones demonstrated positive staining for α -Fetoprotein, a marker of the endoderm; Muscle actin, indicative of the mesoderm; and Nestin, characteristic of the ectoderm. Additionally, the nuclei were counterstained with DAPI, emitting a blue fluorescence. Scale bars 100 μ m.

two weeks (refer to section 3.4.3 for more details). Immunofluorescence assays were utilized to detect the expression of specific markers indicative of differentiation into each of the three germ layers within the FAHN iPSC line. The EBs displayed positive immunoreactivity towards antibodies specific to α -Fetoprotein (for the endoderm), Muscle actin (for the mesoderm), and Nestin (for the ectoderm) as shown in Figure 15. This confirmed their capability to differentiate into cell types representative of all three germ layers.

4.1.4 Analysis of Genetic Stability

A karyogram was prepared for the generated iPSC line, an essential step due to the potential for chromosomal alterations during the reprogramming process, (I. May Vaz et al. 2021; Mayshar et al. 2010). The karyogram data was provided by WiCell company (for more details see 3.4.2 section). This analysis of the iPSC line's metaphases showcased the typical human complement of 22 pairs of autosomes and two sex chromosomes, affirming the integrity of the cell line's chromosomal structure. The examination revealed no deviations from the expected human female karyotype (46, XX), underscoring the genetic stability of the iPSCs (refer to Figure 16 for details).

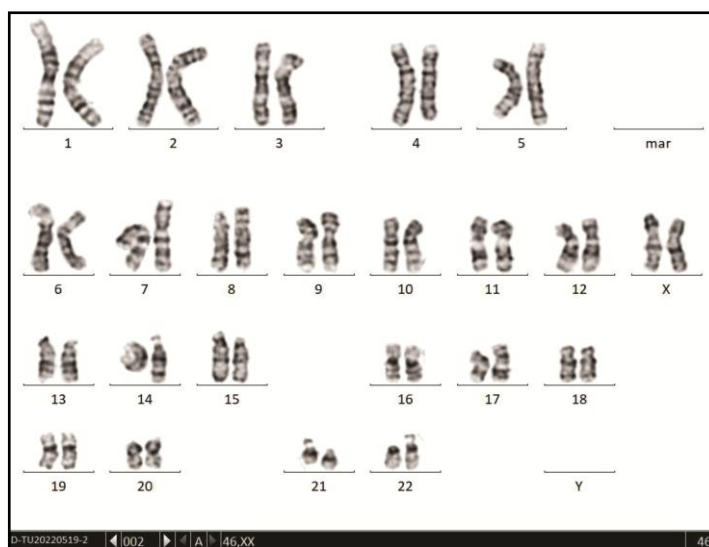


Figure 16: The karyogram of the established FAHN iPSC line. The karyotype is presented to evaluate the cell line's chromosomal composition, including the 22 pairs of autosomes and the XX sex chromosomes, for the determination of its karyotype. This analysis confirms that the FAHN cell line maintains chromosomal integrity, with no chromosomal aberrations observed.

4.1.5 Short tandem repeat analysis

To verify the identity of the cell lines, short tandem repeat (STR) analysis was performed on both the iPSC line and the original fibroblast cells. Identical polymorphisms were observed in the fibroblasts and the derived FAHN iPSC line across 18 genomic loci (refer to Table 4.1).

The analysis detailed the number of nucleotide sequence repetitions on both alleles, as represented by the numeric values. The complete concordance of STR profiles provides unequivocal evidence that the iPSC line was indeed derived from the donor's corresponding fibroblast cell line.

Table 4.1: STR Analysis of FAHN cell line

Sample	D5S81 8	D13S31 7	D7S82 0	D16S53 9	vWA	TH01	AME L	TPO X	CSF1P O
Fibroblast	10.12	11.12	11.20	11	15.17	6.93	X	8,9	10.12
iPSCs	10.12	11.12	11.20	11	15.17	6.93	X	8,9	10.12

4.1.6 FA2H Variants Analysis

The analysis of FA2H variants was conducted by PD Dr. rer. nat. Hugo Murua Escobar, Department of Medicine, Clinic Hematology, Oncology, Palliative Medicine, University Medical Centre Rostock through a mutation analysis utilizing targeted Next Generation Sequencing (NGS) of the *FA2H* gene. This examination uncovered the presence of two mutations, p. Gly45Arg and p. His319Arg, in both fibroblasts and iPSCs of the FAHN cell line, each mutation displaying an allele frequency of about 50% (refer to Table 4.2). Hence, this pattern represents a compound heterozygous mutation.

Table 4.2: Result of mutation analysis

Cell line	Cell type	Amino acid change	Allele ratio	Frequency
FAHN	Fibroblaste	p.His319Arg	T=0.513 C=0.487	48.70 %
		p.Gly45Arg	C=0.4827 T=0.5173	51.73 %
	iPS Cells	p.His319Arg	T=0.504 C=0.496	49.60 %
		p.Gly45Arg	C=0.5111; G=0.4889	50.88 %

In summary, FAHN clone is shown to be a bona fide iPSCs and thus can be used for any further disease-related experiments.

4.2 Generation and Characterisation of Neural Progenitor Cells

Neuronal cell differentiation was conducted using a small molecule-based approach following the protocol outlined in Section 3.5. The FAHN iPSC colonies (Figure 17 A) were individually seeded and supplemented with small molecules FGF2, SB-431542, and LDN193189 for two weeks, resulting in the formation of neural rosettes (Figure 17, arrow). Neural rosettes first appeared on days 11-13, gradually increased in quantity, matured, expanded the size of their lumens, and then spontaneously regressed by day 14. The neural rosette serves as the

developmental signature of neuroprogenitors in cultures of differentiating stem cells. Rosettes are radial arrangements of columnar cells that express several proteins found in neuroepithelial cells of the neural tube. These neural rosettes are comprised of NPCs that express the surface marker PSA-NCAM (polysialic acid neural cell adhesion molecule). These NPCs were isolated using anti-PSA-NCAM antibodies attached to magnetic beads (refer to Figure 17). After cell sorting, the PSA-NCAM-positive NPCs were highly homogeneous and exhibited a spindle shape, which is the typical morphology of NPCs. Notably, these cells reassembled into a rosette-like structure at high density. The NPCs were characterized by immunofluorescence staining for the neural progenitor cell markers Nestin, PAX6, SOX2, and SOX1. While characterizing the expanded NPCs through Immunofluorescence analysis, the obtained results showed an extensively strong signal for PAX6 (Figure 17, D, F) and SOX2 (E, F). In addition to PAX6 and SOX2, the other neural marker, such as Nestin (Figure 17 G, I) was strongly expressed in the neural rosettes with pronounced expression of SOX1 (Figure 17 H, I), a tight junction protein in the central lumens of neural stem cell rosettes. Nestin, an intermediate filament protein, is predominantly expressed in nerve cells. PAX6 plays a crucial role in establishing the pallial-subpallial boundary, which delineates the dorsal (future cerebral cortex).

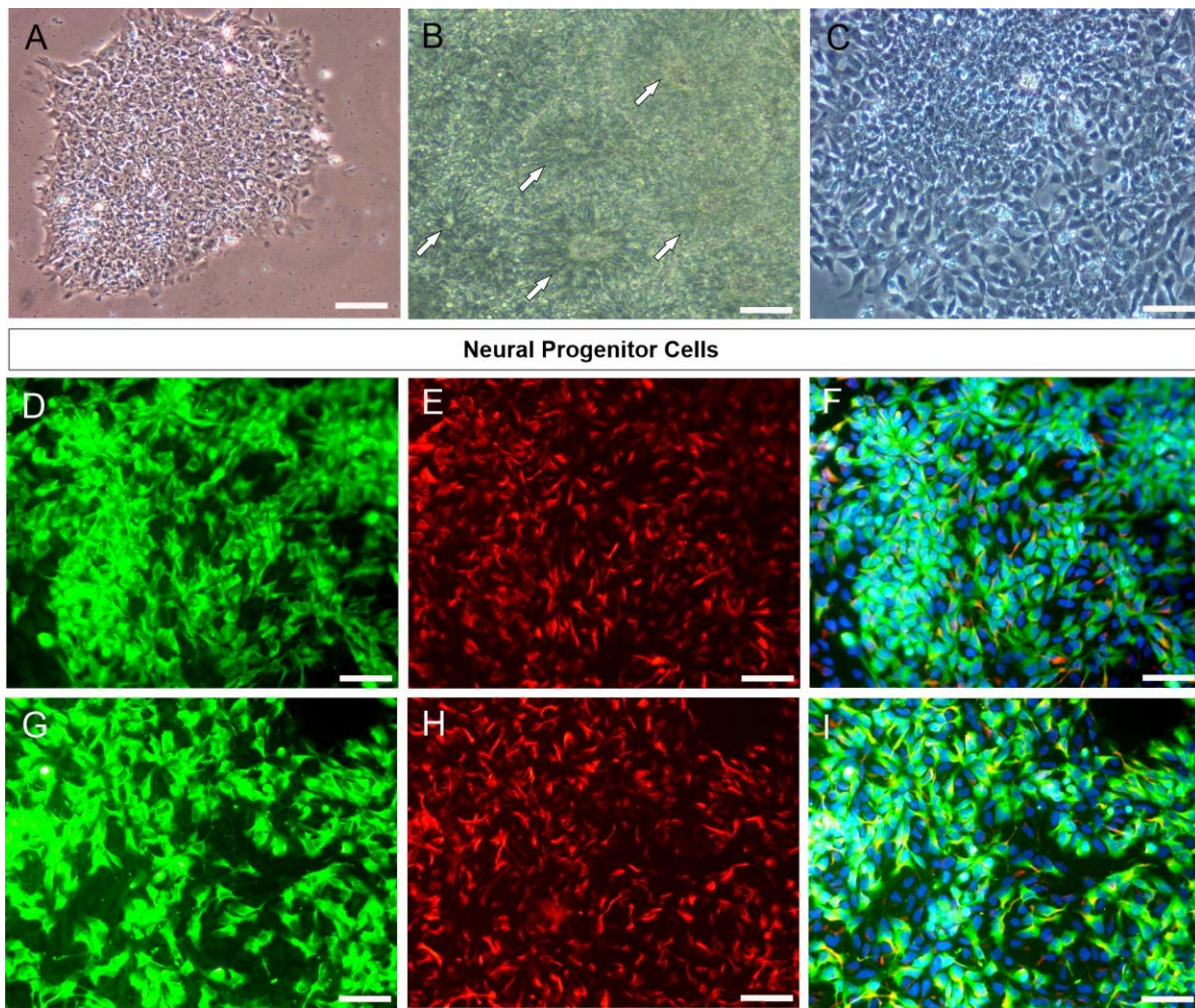


Figure 17: Generation of Neural Progenitor Cells (A) In the neural cell model, iPSCs were cultured as colonies on a Matrigel substrate enriched with a proprietary cocktail of small molecules. **(B)** This protocol facilitated the generation of neural rosettes, structures composed of PSA-NCAM⁺ neural precursor cells **(C)**. These progenitors were then selectively separated by magnetic purification, using bead-coupled antibodies for specificity. Further characterisation of the FAHN NPC cell line was performed using immunofluorescence staining, which showed positive expression of the neuronal markers PAX6 **(D, F)**, SOX2 **(E, F)**, Nestin **(G, I)** and SOX1 **(H, I)**. The nuclei of these cells were clearly labelled with DAPI staining (blue; **F, I**) for enhanced visualisation. N = 18, n = 3 independent differentiations per line. Scale bars 100 μm

4.3 Generation and Characterization of a Neural Differentiated Cells

To assess whether the iPSC-derived NPC subset is functional and capable of differentiating into neural cells, we performed differentiation into Neural Differentiated Cells (NDCs). The NPCs from both the FAHN and CTRL cell lines were differentiated into NDCs through spontaneous differentiation over a period of six weeks, as depicted in Figure 18. Figure 18 illustrates the ability of both control and FAHN NPCs to differentiate into neurons and astrocytes. The

detailed protocol for this process is described under Section 3.5. This was assessed by seeding NPCs at the desired dilution and facilitating spontaneous differentiation by renewing the medium twice per week (Figure 18, A). Over several weeks, the NPCs began to differentiate, with cells developing dendritic branches with spines, forming the somatic area of the neuronal cells, and exhibiting an increase in neurite length. By the end of the maturation period, neurons had developed a high number of long axons and an increased number of dendritic branches (Figure 18 B). The generated neurons and other glial cells were analyzed using immunofluorescence staining. After differentiation process of 6 weeks NDCs were fixed in 4 % PFA and immediately stained for β -III-tubulin and glial fibrillary acidic protein (GFAP), OLIG2, O4, SO10 and MBP. The resulting NDCs were found to comprise a mixture of neurons that were positive for β -III-tubulin and glial cells that were positive for GFAP. However, the cells did not express any of the oligodendrocyte markers OLIG2, O4, SOX10 and MBP, which are used for detecting OPCs. The β -III-tubulin, a microtubule element predominantly expressed in neurons, plays a crucial role in neurogenesis, neuronal proliferation, axon guidance, and maintenance. GFAP, an intermediate filament protein, is integral to the astroglial cytoskeleton. The quantification of β -III-tubulin for neurons and GFAP for astrocyte cells (Figure 18 I and J) demonstrates that there is no statistically significant difference in fluorescence intensity for these two markers between the CTRL and FAHN cell lines. These results confirm that NDCs do not exhibit any differences during the differentiation process.

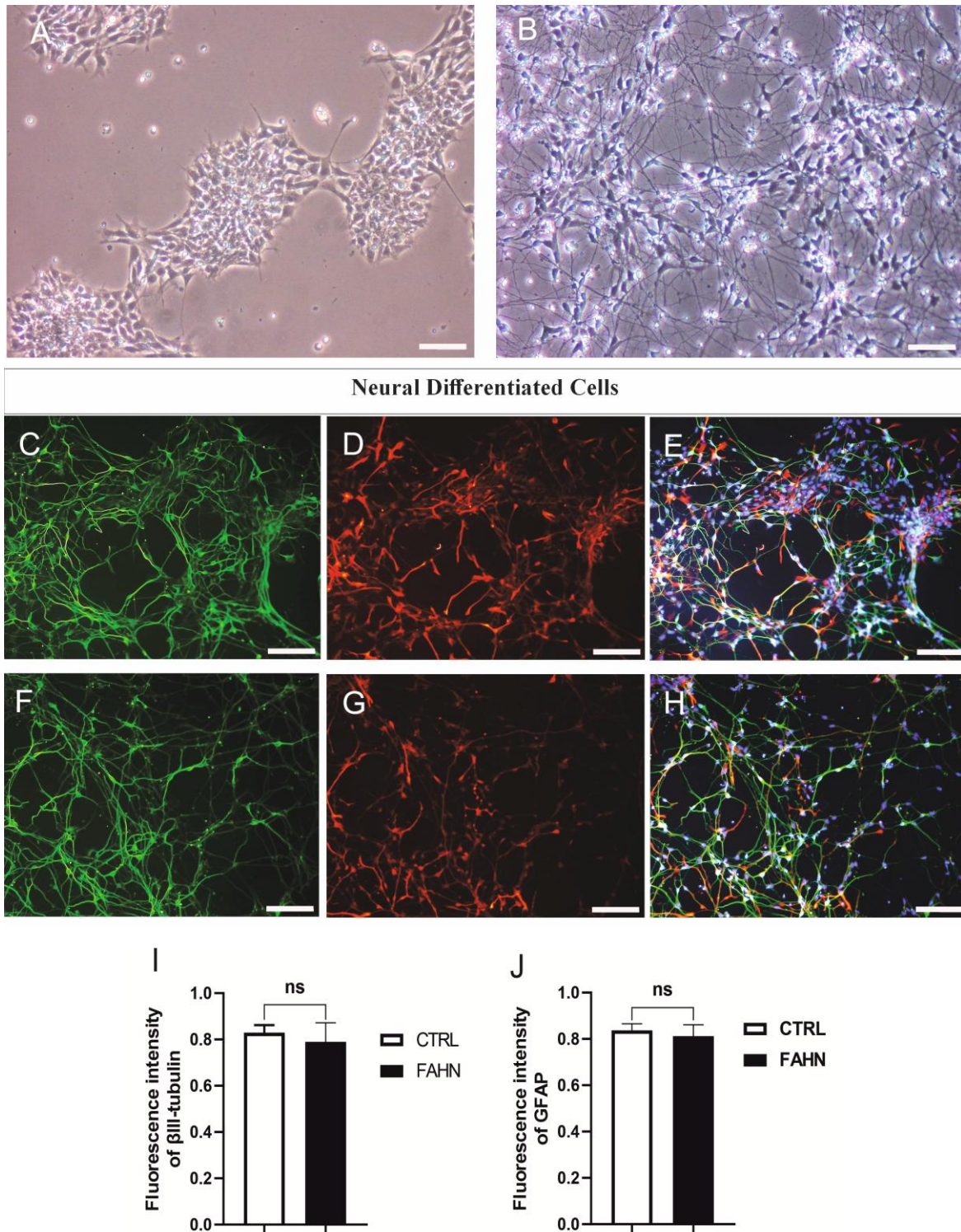


Figure 18: Generation of Neural Differentiated Cells. NPCs (A) were expanded and differentiated into NDCs over a period of six weeks (B). The NDCs of the control cell line (C, D, E) and the FAHN cell line (F, G, H) show positive staining for the neuronal marker β III-tubulin (green; C and F) or the glial marker GFAP (red; D and G). (I) The quantification of fluorescence intensity for β III-tubulin, (J) and the for GFAP shows no significant difference between CTRL and FAHN cell line. Thus, NDCs are a mixed culture of neurons and glial cells. Nuclei were stained with DAPI (blue; E and H). N = 20 n = 9 independent differentiations per line. Scale 100 μ m.

4.4 Generation of iPSC-derived oligodendrocytes

For the generation of OLs from iPSCs, a protocol and main strategy have been detailed in Section 3.6. Following the implementation of minor modifications, the protocol was previously established and published by Juan Garcia Leon and colleagues (Juan Garcia Leon et al., 2020). The protocol has been refined and enhanced, incorporating a primary procedure for neural induction of iPSCs and directing neuroepithelial cells towards the primary motor neuron precursor domain of the developing spinal cord. The entire process of OLs generation is illustrated under (Figure 19, Figure 20 in bright field and Figure 21). The induction of OLIG2 precursors takes 8 days and involves the use of four small molecules: SB431542, SAG, RA and LDN193189. These molecules work together to inhibit the SMAD signaling pathway, which is essential for the development of OLs *in vivo* (Figures 19, 20 and 21). Following an eight-day induction period, Figures 19 and figure 20 demonstrate that cells starts to change morphologically due to neural induction with SMAD molecules. In order to enhance the yield and stimulate the differentiation of OPCs, OLIG2 precursors were transduced with a lentiviral vector encoding the *SOX10* coding sequence, cells morphology start to change and cells appear to have morphology of pre-OPCs (Figure 19, 20 and Figure 21). The presence of *SOX10* in neural precursors is crucial for the efficient generation of OLs capable of engrafting and synthesising myelin both *ex vivo* and *in vitro*. Figure 19 D and Figure 20 D in bright represents cells visually showing the morphology of OLS, cells have enlarged roundish nucleus and long external branch and dendrites. Additional to this In this protocol during the differentiation process GFAP⁺ astrocytes and MAP2 or TUJ1 neurons are not present during the induction phase, but GFAP⁺ expressing cells appear during the coculture with iPSC-derived neurons.

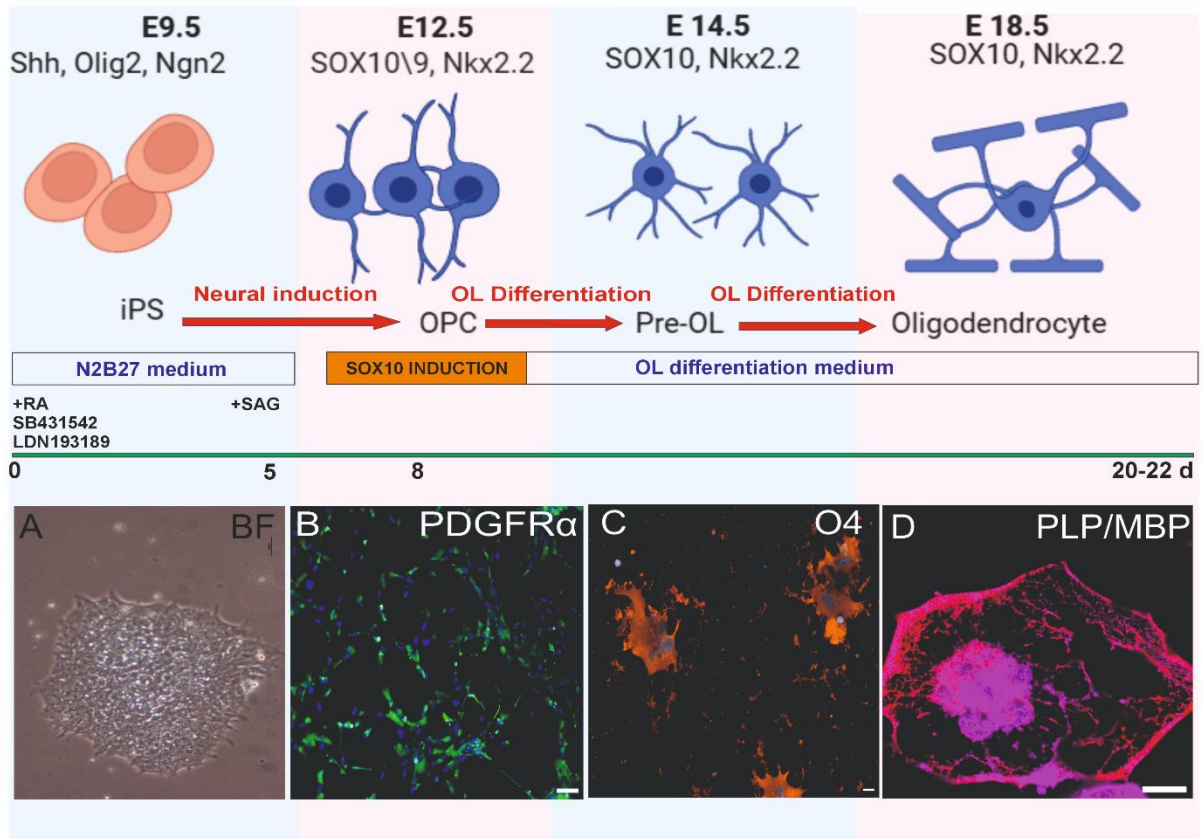


Figure 19: Representative images of the main stages of the protocol for the generation of OLs using the lentiviral-based methodologies. A–D, Characterization of the different stages of the protocol. A, Bright field image of iPS colonies on day 0 before neural induction. B, Immunofluorescence staining for PDGFR α as a marker for positive pre-OPC after 5 d of SOX10-mediated OL induction. C, Immunostaining for surface antigen O4 (O4) as a marker for late OPCs after 10 d of SOX10-mediated OL induction. D, Immunostaining for MBP as a marker for mature OLs after 10 d of SOX10-mediated OL induction, n = 21 independent differentiations per line.

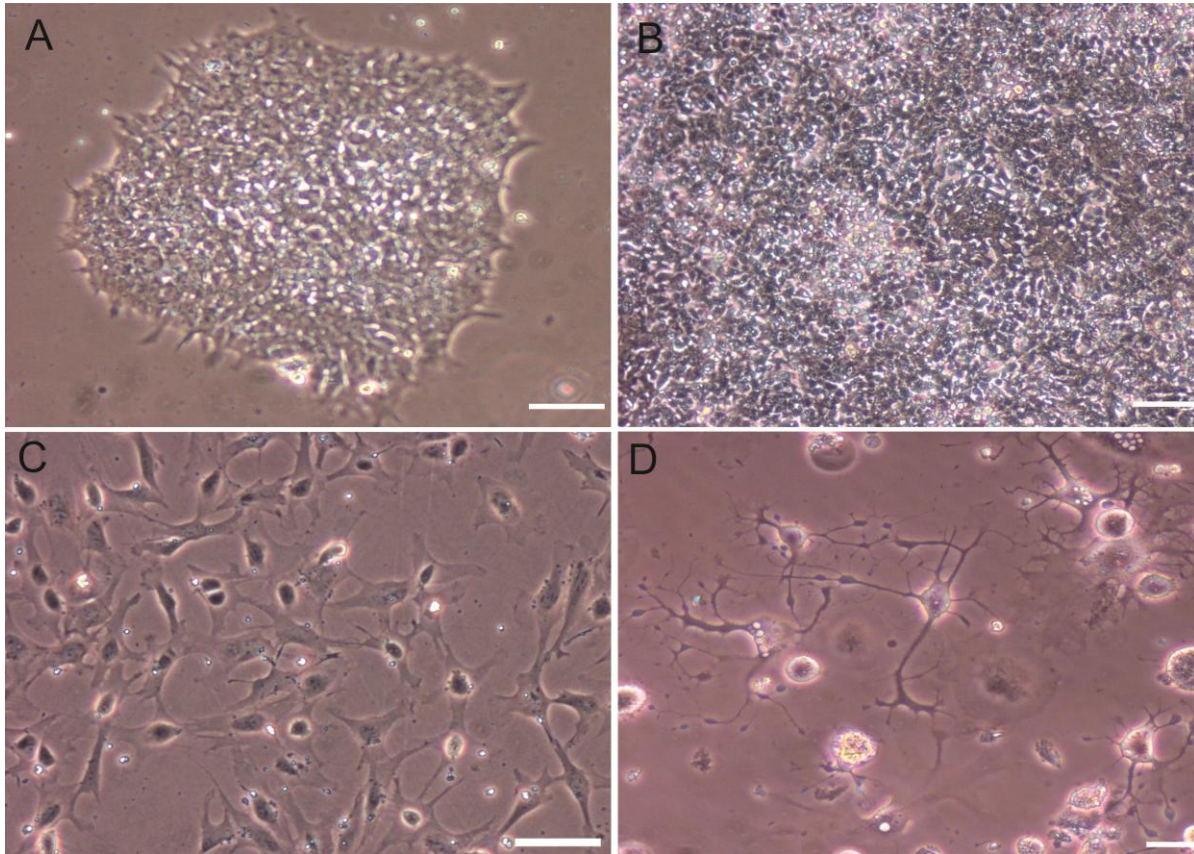


Figure 20: Oligodendrocyte precursor cells generating from iPSCs. (A) Initially, iPSC colonies were grown on matrigel-coated plates and treated with SMAD inhibitors for eight days to induce *Olig2* precursors (B). Following this, the *OLIG2* precursors were transfected with the *SOX10* transcription factor to promote oligodendrocyte differentiation. The cells were then cultured for an additional 10 days. (C) Depicts the OPCs five days post-transfection. (D) After 10 days of culturing, mature myelinating oligodendrocytes were visible, characterised by their morphology with long, wide branches. $n = 20$ independent differentiations per line. The scale bars for Figures 15A and 15B were set at $100\ \mu\text{m}$, while those for Figures 15C and 15D were $50\ \mu\text{m}$.

Twenty-four hours after transfection, pre-OPCs were stained with *SOX10* and *PDGFR- α* markers (Figure 21). CTRL is represented under Figure 21 A, C, D, E, F while Figure 21 B, G, H, I, J is representing FAHN cell line. Figures 21 C and G illustrate the fluorescence staining for the *PDGFR- α* marker in both cell lines (stained in green). The signal was found to be concentrated near the nucleus, with very little present in the cytoplasmic area. *PDGFR- α* plays a role in the maintenance and growth of OPCs in the CNS, with its signalling downregulated prior to the differentiation of OPCs into mature OLs. In both cell lines, *SOX10* was primarily located around the nucleus (stained in red), with a minimal amount of the marker distributed between the nucleus and cytoplasm (Figure 21 D, H). To cultivate mature OLs and myelinating OL cells, the culture of OPCs was maintained for an additional 10 days in a medium supplemented with small molecules and growth factors crucial for OLs differentiation (see section 3.6). This method yielded highly enriched oligodendrocyte cultures. Figure 21 E and I

shows cells from both cell lines stained for the oligodendrocyte progenitor surface marker O4, which belongs to the sulfatide class of glycosphingolipids. In both cell lines, a strong signal was present along the entire surface of the OPCs. After 10 days of differentiation, the mature and myelinated oligodendroglial populations were stained for MBP. As the second most abundant protein in CNS myelin, MBP, expressed in mature and myelinating OLs, shows a strong signal stained in red, mostly located through the whole cell, however a stronger signal is still present in OLs extensions showing its crucial role for the adhesion of the cytosolic surfaces of multilayered compact myelin (Figure 21 F and J). Both cell line's mature OLs were found to express the MBP marker, (Figure 21 F and J). The quantification of SOX10-positive cells demonstrates that there is no discernible difference in the expression and differentiation of OPCs in FAHN (Figure 21). This quantification corroborates the assertion that FAHN cell lines are capable of differentiation and expression of the requisite factors. Figure 21 depicts the quantification for the O4+ marker, which is expressed in OPCs. The analysis of this marker corroborates the visual data, confirming that FAHN cell lines are capable of expressing and differentiating into pre-OPCs and OPCs, as well as mature OLs. Therefore, it can be concluded that FAHN cell lines do not exhibit any differentiation or maturation issues.

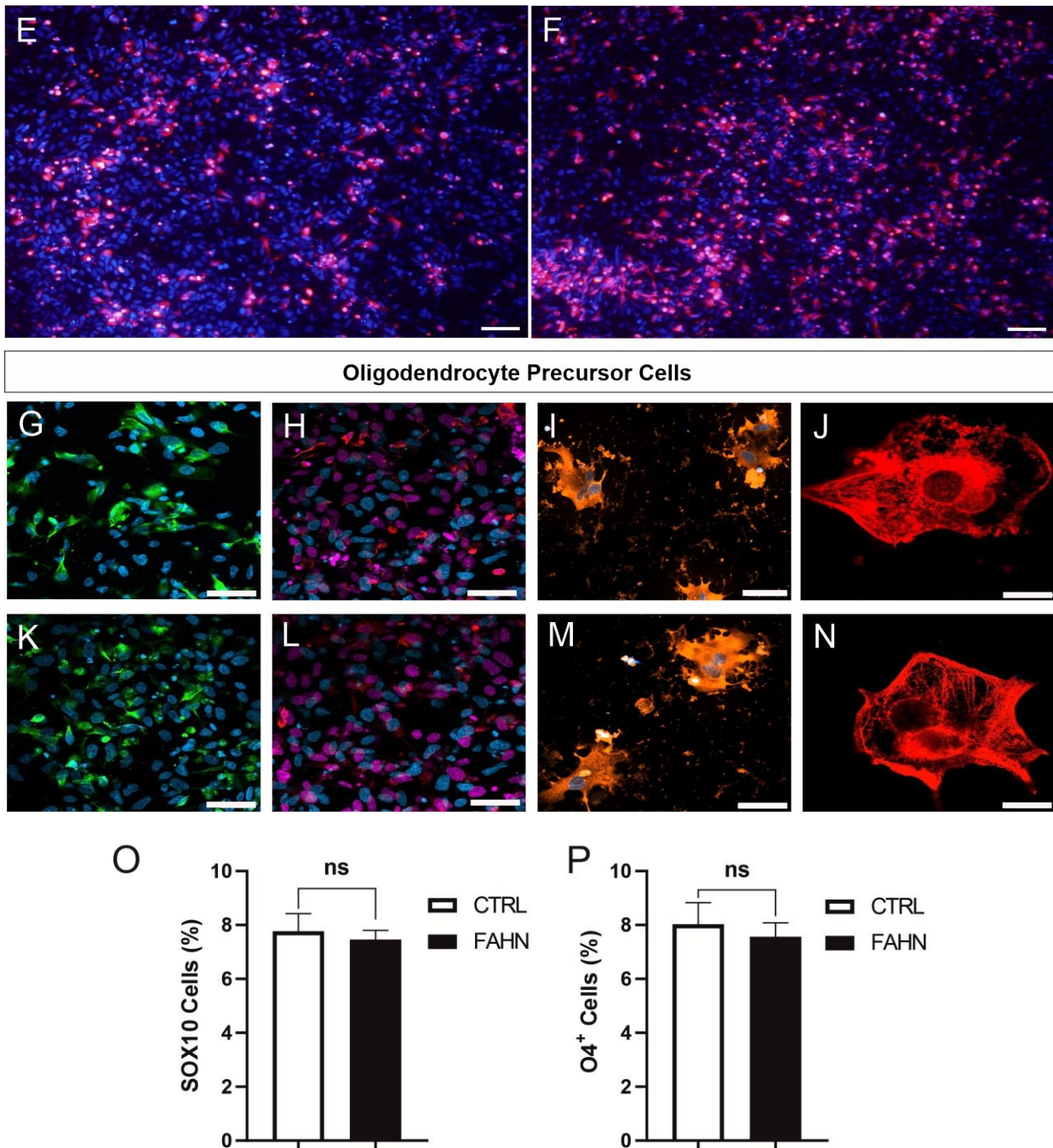


Figure 21: Oligodendrocyte precursor cells differentiation process. This figure illustrates the stages of the differentiation process, as confirmed by immunofluorescence staining of the control cell line (A, C, D, E, F) and the FAHN cell line (B, G, H, I, J). The image A, B represents staining for the OLIG2 marker (red). (C, G) 24 hours after transfection with *SOX10*-mediated gene OPCs were stained for PDGFR- α (green). (D, H) Both cell lines expressed SOX10 marker (red) 24 hours after transfection. (E, I) Cells of both cell lines were positive for O4 marker, indicating differentiation to the oligodendrocyte stage. (F, J) OLs in both cell lines were positive for the MBP marker, indicating that cells can express myelination markers. The quantification analysis of SOX10 (O) and O4⁺ (P) shows no significant difference between CTRL and FAHN cell line. Nuclei were stained with DAPI (A, B, C, D, E, G, H and I). (A, B) Scale bars 150 μ m, (C, D, G, H) Scale bars 100 μ m, (E, I) Scale bars 50 μ m, (F, J) Scale bars 20 μ m. N=10 per differentiation, n = 20 independent differentiations per line.

Following the differentiation of OPCs, the O4+ expressing cells were purified using anti-O4 microbeads. To confirm the purity of O4 expression, the O4+ cells were sorted using FACS. A small aliquot of 50,000 to 100,000 cells was labelled with O4 APC antibody and incubated for 15 minutes prior to analysis. A control sample that had not been stained was used to define the gate threshold. Figure 22 presents plots from the FACS analysis for the CTRL (Figure 22 A, C) and FAHN cell lines (Figure 22 B, D). Subsequently, the samples were reanalysed after gating for live, single cells. Figure 22 A demonstrates that in the CTRL cell line, 89.6% of cells were positive for the O4+ marker, while Figure 21B indicates that in the FAHN cell line, 87.7% of purified cells were positively expressing the O4+ marker.

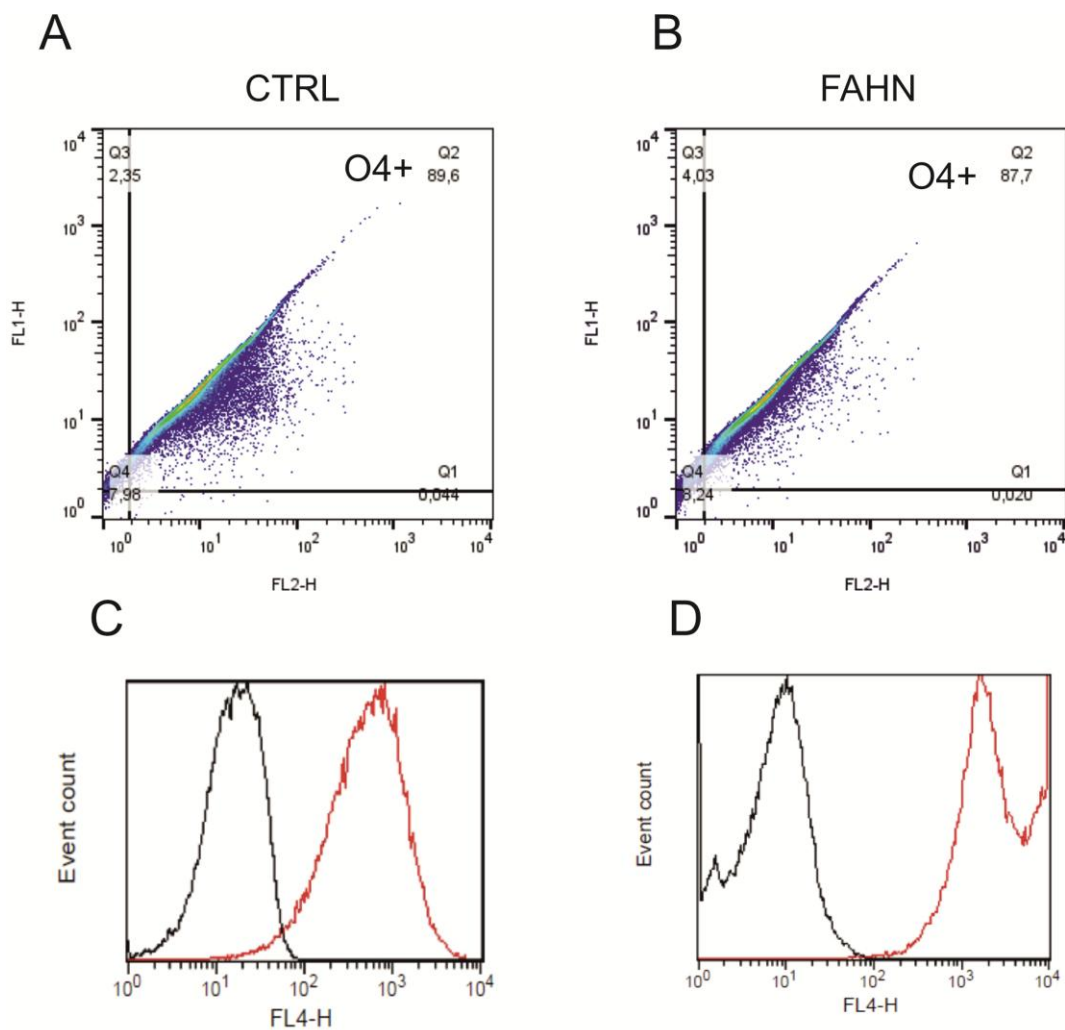


Figure 22. Example of a FACS dot plot for the number of O4+ cells within the culture after 10 d of SOX10 induction. Cells were distinguished from debris by forward and side scatter then singlet cells were gated. Live cells were gated by dead cell exclusion, and Oligodendroglial cells were defined by positive staining O4+ marker. Panels A and B represent the CTRL and FAHN cell lines, respectively. Panels C and D quantify the number of O4+ cells determined by FACS during the days of SOX10 induction. The flow cytometry results were analyzed using Flow Jo (FlowJo, LLC, USA) software. n=2

4.5 Coculture of iPSC-derived oligodendrocytes and neurons

In order to ascertain whether iPSC-derived OLs are capable of networking with neurons and forming myelin *in vitro*, a series of coculture experiments were conducted utilising a range of neuronal substrates. In a separate cell culture dish, neurons were generated in accordance with the methodology outlined in section 3.5, while OLs were generated in accordance with the methodology outlined in section 3.6. Upon reaching a mature stage of differentiation, the OLs were collected (see 3.7) and placed on a plate containing neurons and astroglial cells. After 24 hours, it was observed that the majority of cells had successfully adhered to the plate surface, with the OLs in the control and FAHN cell lines exhibiting clear adherence (Figure 23). After several days in mix culture, the cells began to create a network and wrap around neuronal axons (Figure 23 A). Figure 23 A, B shows representative image of coculture in brightfield, including a magnified bright field image of myelinating OLs after one week of coculture shown in Figure 23 B. Figure 23 C represent staining of MAP2 and MBP 5 days after of coculture of neurons and OLs. As our objective was to develop and establish a fully human culture system, we extended the culture of myelinating OLs and neurons for additional six weeks to achieve a compact myelin sheath produced *in vitro*. The method yielded a highly oligodendrocyte-neuronal myelinating coculture, which was confirmed by immunostaining (Figure 23 C, D, E stained for CTRL; F, G, H belongs to FAHN). To confirm the presence of myelin, antibodies against MBP were used to stain myelin (C, F, E, H) and antibodies against MAP2 were used to stain neurons (D, G, E, H). In both cell lines, the MBP signal was robust, and both cell lines exhibited positive staining.

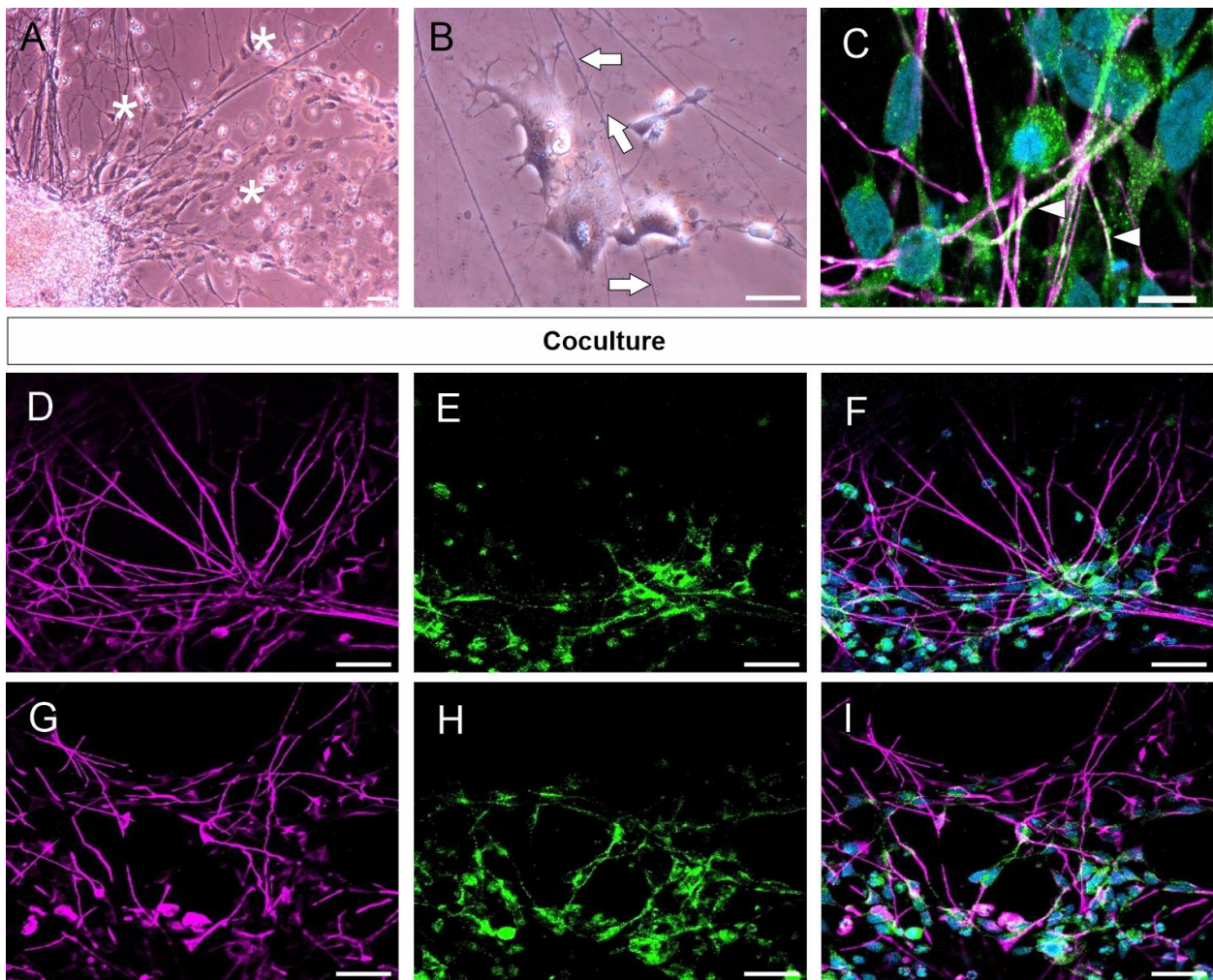


Figure 23: Coculture generation. A coculture comprising mature neurons and mature OLs was generated and cultured for six weeks. At 24 hours, OLs had successfully attached to neurons (indicated by *). (A, B) After four days of culturing, OLs began to create connections and wrap around axons (indicated by arrows). (C) the results of MAP2 and MBP staining conducted 4 days after the coculture of neurons and OLs, as indicated by the triangular symbol. After six weeks, the cultures were evaluated by immunostaining for CTRL cell line (D, E, F) and FAHN (G, H, I), respectively. The myelinating oligodendrocytes were stained for the MBP marker (E, H), while the neurons were positive for the MAP2 antibody (D, G). The nuclei were stained with DAPI (Blue). All images are presented at a scale of 50 μm , with the exception of B and C which is presented at a scale of 20 μm . N=13 n = 9 independent differentiations per line.

4.6 Pathophysiological characterizations of FAHN disease

4.6.1 FA2H protein expression in FA2H-deficient cells

To investigate the effect of the mutation on FA2H protein expression, both control and FAHN lines were employed, specifically in NDCs and OPCs. This analysis was conducted using Western blotting techniques. The WB data presented in Figure 24 shows the NDCs of each cell line. In this blot, the undigested cell lysates exhibit a moderately intense band of approximately 50 kDa, corresponding to the total FA2H protein present. The GAPDH protein, with a molecular weight of 37 kDa, was employed to normalise the signal. In the CTRL cell line, samples were positioned in the first and second lanes, representing different samples or passages from the same cell line. In contrast, samples from the FAHN cell line were placed in the third and fourth lanes, with no replicates (Figure 24 A). The FA2H protein displays a more pronounced and stable expression in the CTRL samples, whereas in the FAHN cell line, this protein expression appears reduced and weaker. The results of the WB experiments are quantified in Figure 24 B, which corroborates these observations. There is a significant reduction in FA2H expression in the FAHN cell line compared to the CTRL. In particular, FA2H protein levels in the FAHN cell line are reduced by 42% in comparison to the CTRL, which indicates a substantial reduction in the FAHN NDC cell line.

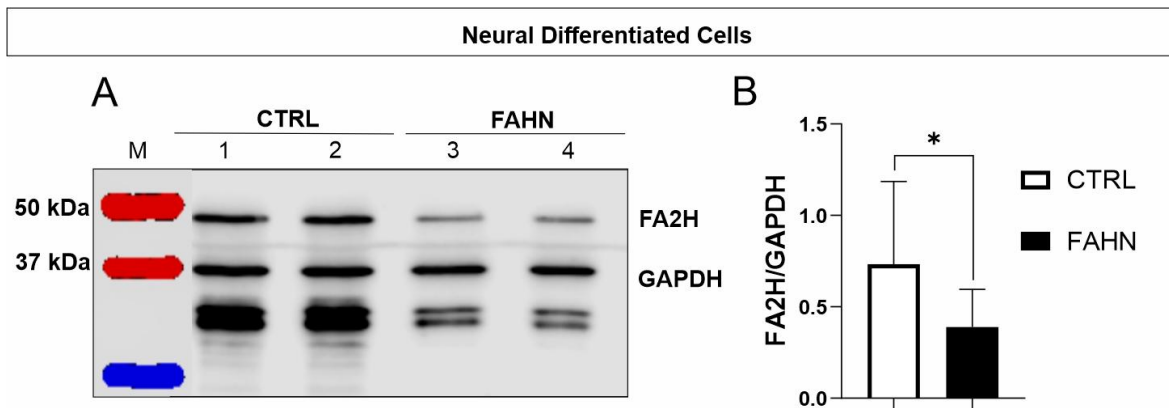


Figure 24: FA2H protein analysis in Neural Differentiated Cells. Part A of the figure shows WB results where NDC cell lysates were analysed for FA2H protein expression. A distinct band visible at approximately 50 kDa corresponds to the total amount of FA2H protein in samples labelled 1, 2, 3 and 4. GAPDH, with a molecular weight of 37 kDa, was used as a reference protein for normalisation and a marker is indicated by 'M'. Part B of the figure details the analysis of the total amount of FA2H protein, showing a significant reduction in the FAHN cell line compared to the CTRL cell line, with a p-value of less than 0.0101. Statistical data presented are mean \pm SD for a sample size of N=16. Significance levels are indicated as follows: '*' for $p < 0.05$ when compared to CTRL.

Similar results were observed in the WB data obtained from OPCs. The OPC cell lysate was collected from cells generated at section 3.6, during the maturation stage. In the control cell line, FA2H protein exhibited a stable expression, indicated by a distinct band at approximately 50 kDa. In FA2H-deficient OPC cells, there is a significant reduction in the total amount of FA2H protein, which is visibly apparent on the blot in Figure 25 A. The quantification shown in the graph indicates a significant reduction in FA2H protein levels in the FAHN cell line compared to the CTRL cell line, with a p-value of <0.0263 . Furthermore, the data revealed that the amount of FA2H protein was higher in OPC cells across both cell lines, whereas in NDCs there was a reduction of FA2H protein in both the CTRL and FAHN cell lines. The collective results of the analysis indicated a significant decrease in total FA2H protein levels in both NDCs and OPCs of the FAHN cell line. This reduction is particularly pronounced in the NDC and OPC compartments when compared to their respective control cell line counterparts in both NDC and OPC.

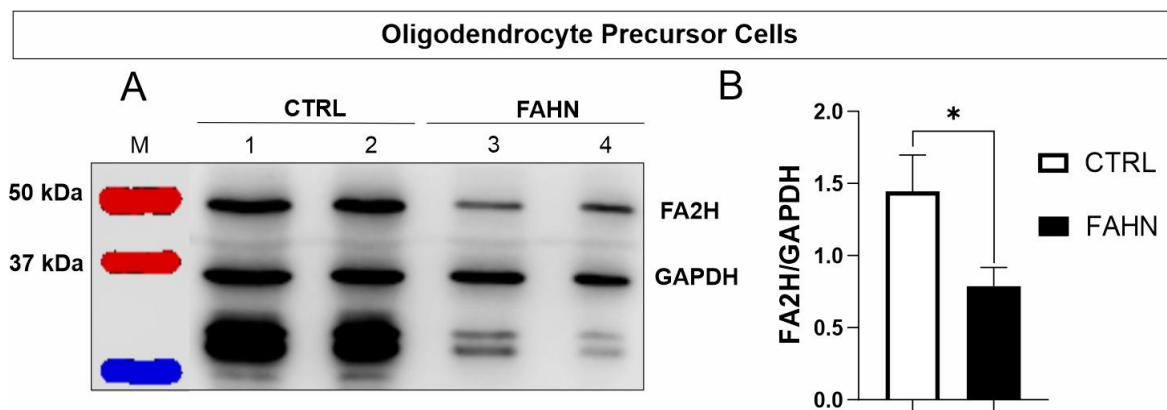


Figure 25: FA2H protein analysis in Oligodendrocyte Precursor Cells. (A) OPC lysates were analysed for protein expression by WB. The distinct band at approximately 50 kDa corresponds to the total amount of FA2H protein in samples 1, 2, 3 and 4. The 37-kDa GAPDH protein was used as a reference protein for normalisation. (B) The FA2H protein amount in the FAHN cell line was significantly reduced compared to the CTRL cell line ($p < 0.0263$). (Mean \pm SD; N=16; * $p < 0.05$ when compared to CTRL).

4.6.2 Subcellular localization of the FA2H protein

To analyse the subcellular localisation of FA2H protein, Immunofluorescence staining followed by quantification analysis of FA2H was performed (Figure 26). NDCs from both cell lines were generated as described in section 3.5. Briefly, NPCs from both cell lines were seeded onto PLO-laminin-coated coverslips and cultured for six weeks until the cells spontaneously differentiated into neurons and other glial cells. Immunofluorescence staining for the FA2H marker was then performed. The results from the CTRL line showed that FA2H signal (FA2H stained in red) was visible in the regions of somata and dendrites (indicated by star), with a significant amount

of protein also found in the axon regions (processes) of the NDCs (Figure 20A indicated by arrows). In contrast, the FA2H fluorescence signal in the FAHN cell line was very weak and showed a diffuse distribution pattern (Figure 26 B). Meanwhile, in the FAHN cell line, FA2H significantly shifted its position from somata to axonal sites, with a very low protein distribution in intracellular regions. By comparing fluorescence intensity (FI), it was observed that the mean value of FI for FA2H in the FAHN cell line was slightly decreased in NDCs. Conversely, the FA2H level in the CTRL cell line is significantly increased. The FI of the FA2H of the FAHN cell line is significantly reduced, with measurements showing CTRL NDCs at 13.06 ± 0.3526 and FAHN NPCs at 6.769 ± 0.036 (Figure 26 C). (Mean \pm SD; N=20; *** = $p < 0.001$ to CTRL).

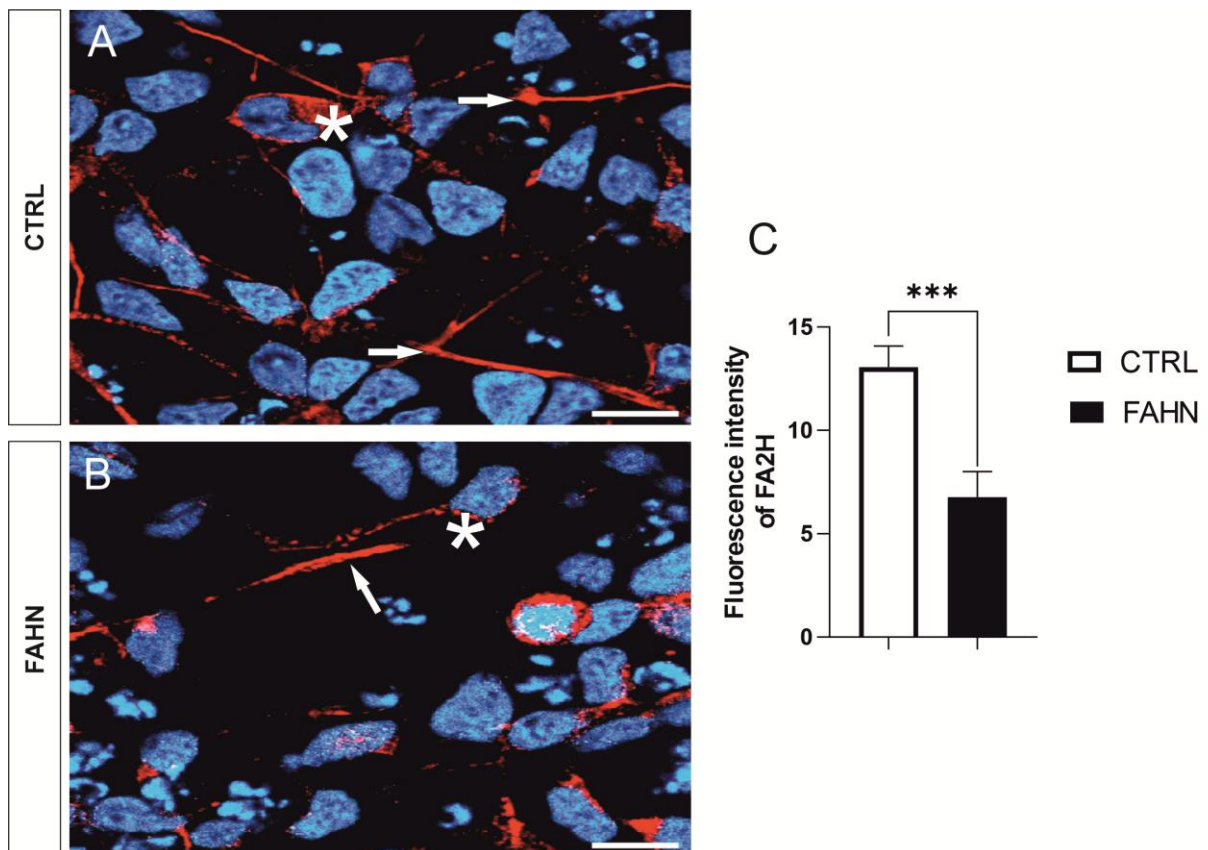


Figure 26: Fluorescence intensity of FA2H protein in Neural Differentiated Cells. (A, B) The FA2H protein (red) was visualised by immunofluorescence staining. The nuclei were stained with DAPI (blue). In the control, FA2H is visible in the somata (indicated by *) and projections of NDCs (indicated by arrow), with a strong fluorescent signal. In the FAHN, the FA2H signal was markedly reduced in intensity and diffusely distributed. (C) Quantitative analysis of fluorescence per area was significantly reduced in the FAHN cell line compared to the CTRL cell line (mean \pm SD; N=20; *** $p < 0.001$ for CTRL). Scale bars 20 μ m.

Similar results were observed using immunofluorescence staining in OPCs (Figure 27) in the CTRL cell line, the FA2H protein showed a strong signal, appearing predominantly as cytoplasmic dots around the nucleus, suggesting that the FA2H protein was largely localised in cytoplasmic regions (Figure 27 A). While the results indicated that the FA2H distribution in the FAHN cell line was similar to that observed in the CTRL cell line. The quantification of OPCs staining's showed a significant reduced signal and intensity in FAHN (Figure 27 B). In addition, the analyses FI in OPCs shows that FAHN OPCs has significantly reduced fluorescence intensity (23.78 ± 0.042) when compared to CTRL OPCs (48.35 ± 0.054).

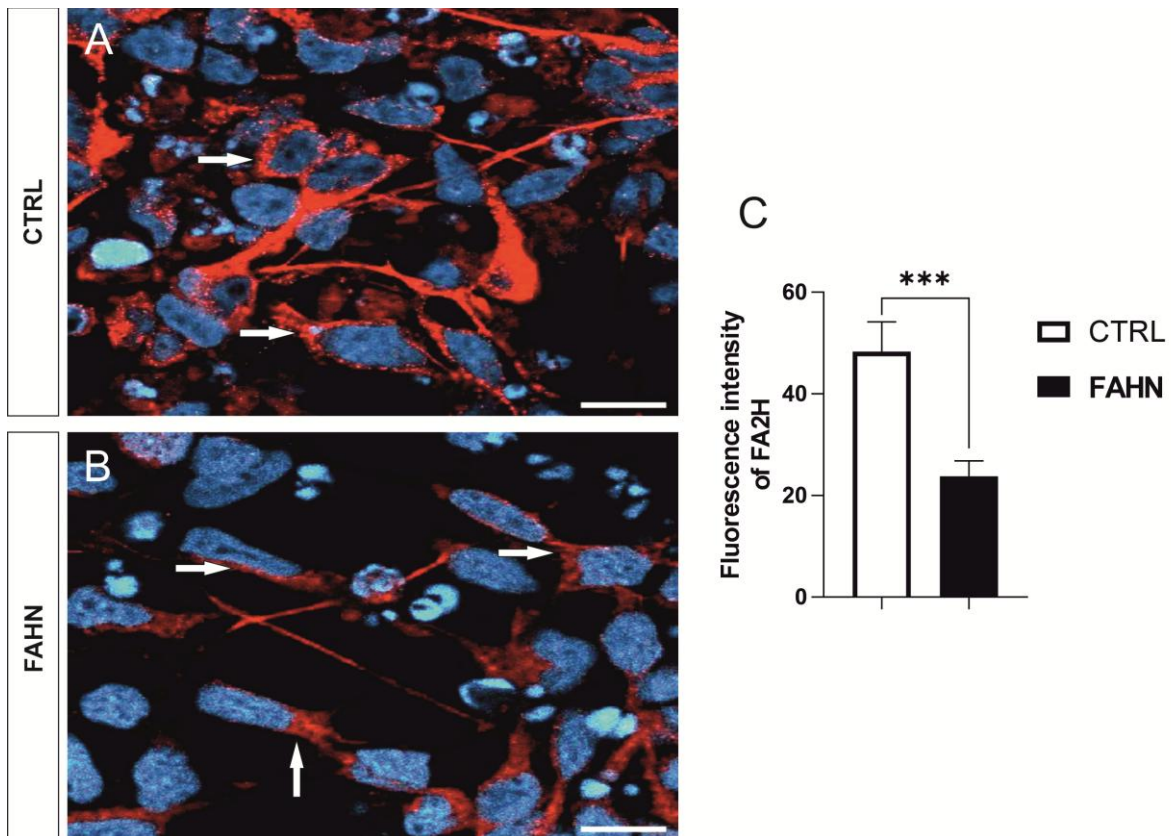


Figure 27: Fluorescence intensity of FA2H protein Oligodendrocyte Precursor Cells. (A, B) Immunofluorescence staining shows that the fluorescence signal of FA2H (red) is visible as cytoplasmic dots around the nucleus of OPCs (arrows). DAPI was used to stain the nuclei (blue). (C) Quantification of fluorescence intensity shows a significantly reduced signal of FA2H in the FAHN cell line compared to the control cell line. (Mean \pm SD; N=20; *** p < 0.001 to CTRL). Scale 20 μ m.

A summary of the findings from immunofluorescence staining revealed that FA2H protein levels were visible slightly reduced in the FAHN cell line. Furthermore, in NDCs, this ER protein exhibited a broader distribution within the cells, though the protein levels were generally less expressed in this cell type across both cell lines. Conversely, in OPCs, the FA2H protein was primarily localized in the cytoplasm, showing an enhanced signal in both cell lines. However, the fluorescence intensity was significantly lower in FAHN.

4.6.3 Characterization of the Oligodendrocyte and Coculture

Following the generation and thorough characterisation of OLs, the investigation delves into the intricacies of their differentiation process. WB and immunofluorescence stainings were employed to study OPCs and coculture cells. The objective of this phase of analysis was to elucidate the dynamics of two key proteins involved in the organisation of the lipid membrane domain, PLP and MBP. In particular, PLP plays a critical role in the early stages of OLs differentiation, while MBP is the second most abundant protein in myelin in the CNS. The objective was to examine the colocalisation of these proteins within OPCs and in coculture using immunofluorescence staining. This approach enables the identification of the spatial relationships between PLP and MBP, as well as the colocalisation of these two proteins with the axonal protein MAP2. This provides insight into their potential interactions and implications. In order to gain a deeper understanding of the role of these proteins in the context of FAHN disease, which is associated with myelin destruction, we conducted further investigations. In addition to PLP and MBP, we focused our attention on another key protein to gain insight into the structural aspects and length of myelin, as well as the Ranvier nodes on myelinated axons. This comprehensive analysis aims to elucidate the intricate interplay between oligodendrocyte-specific proteins and their influence on neurons and the structural integrity of the myelin sheath.

4.6.3.1 Evaluation of MBP and PLP protein in FA2H-deficient cells

To investigate the effect of the major myelin proteins, MBP and PLP, on the dynamics and lateral membrane organisation of these myelin-specific proteins, we performed WB analyses on OPCs and coculture of both cell lines. These cells represent mature OLs, which are responsible for the production of lipid proteins essential for myelin formation. WB analysis of MBP protein in the CTRL cell line revealed a distinct, bright band at approximately 20-13 kDa, indicating robust expression of the target protein (Figure 28 A). This inner leaflet-associated peripheral membrane protein, MBP, was found to integrate into CHAPS-resistant microdomains, appearing as insoluble fractions of 20-13 kDa in size (see Figure 28 A). For the purpose of normalisation and reference, the GAPDH protein was employed, exhibiting a molecular weight of approximately 37 kDa. For the optimal formation of the myelin membrane and effective wrapping around axons, OLs must produce sufficient and comparable amounts of MBP protein. However, this equilibrium is disrupted in coculture with the FAHN cell line, as evidenced by a significant reduction in MBP protein levels in WB analysis, whereas there is significant difference between the control cell line and FAHN in OPCs (see Figure 28 B). In

the CTRL in OPCs, a visible strong signal was observed, while in FAHN, the band appeared to be less bright and thinner. Interestingly, at the right side of the WB membrane where the coculture samples were located, the signal in the CTRL and FAHN cell lines appeared to be stronger and the bands thicker. The amount of protein in the FAHN coculture was significantly decreased compared to the CTRL cell line (Figure 28 B). In general, the expression of the MBP protein in the coculture samples of both cell lines was higher than in the OPCs samples of both cell lines. However, this increase was not statistically significant (Figure 28 B).

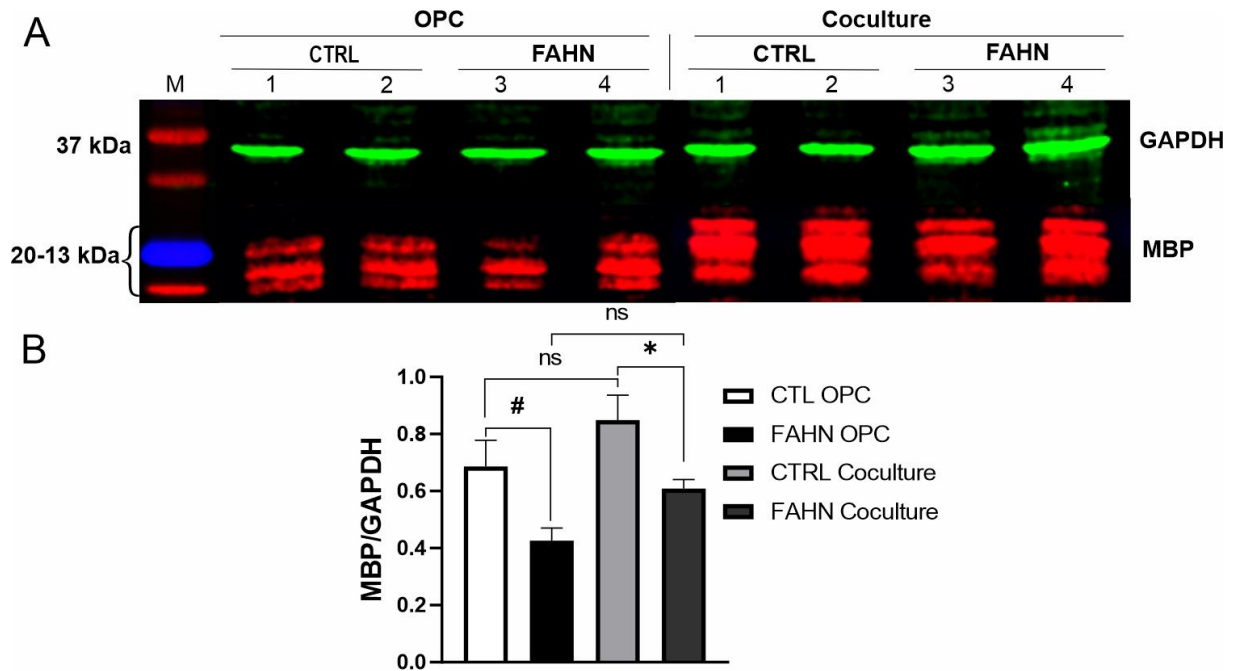


Figure 28: Analysis of myelin protein MBP in Oligodendrocyte Precursor Cells and coculture. (A) Cell lysates were examined for the expression of MBP by WB. The MBP protein was detected in the samples OPC (1, 2, 3, 4) and Coculture (1, 2, 3, 4) with a molecular weight of approximately 20-13 kDa. The letter M indicates the presence of a protein marker. The 37 kDa GAPDH protein was employed as a reference standard. The OPC in both cell lines exhibited a lower signal expression. In contrast, the coculture exhibited increased signal expression, and the control exhibited a stronger signal compared to the FAHN cell line. (B) The quantification of WB data in OPCs revealed no significant difference in MBP levels between the control and FAHN groups. However, in the coculture group, the level of MBP protein was significantly higher (mean \pm SD; N=14-16; *# = $p < 0,05$ for Coculture CTRL).

In accordance with the findings of the MBP analysis in FAHN, the WB analysis of PLP protein from FAHN demonstrated a significant reduction in the coculture samples (Figure 29A). The molecular weight of PLP protein is 20 kDa. In both cell lines, a very small quantity of PLP protein is present in OPCs. However, the total PLP protein in both the CTRL and FAHN cell lines shows a significant increase in coculture samples where OLs are cultured with neurons for a period of six weeks. In the CTRL cell line, the increase in PLP protein is approximately 62%, whereas in the FAHN cell line it is increased for 28%. This difference is statistically significant in both cell lines (Figure 29B). Moreover, the expression of PLP is significantly

diminished in the FAHN coculture in comparison to the CTRL cell line coculture samples ($p < 0.001$).

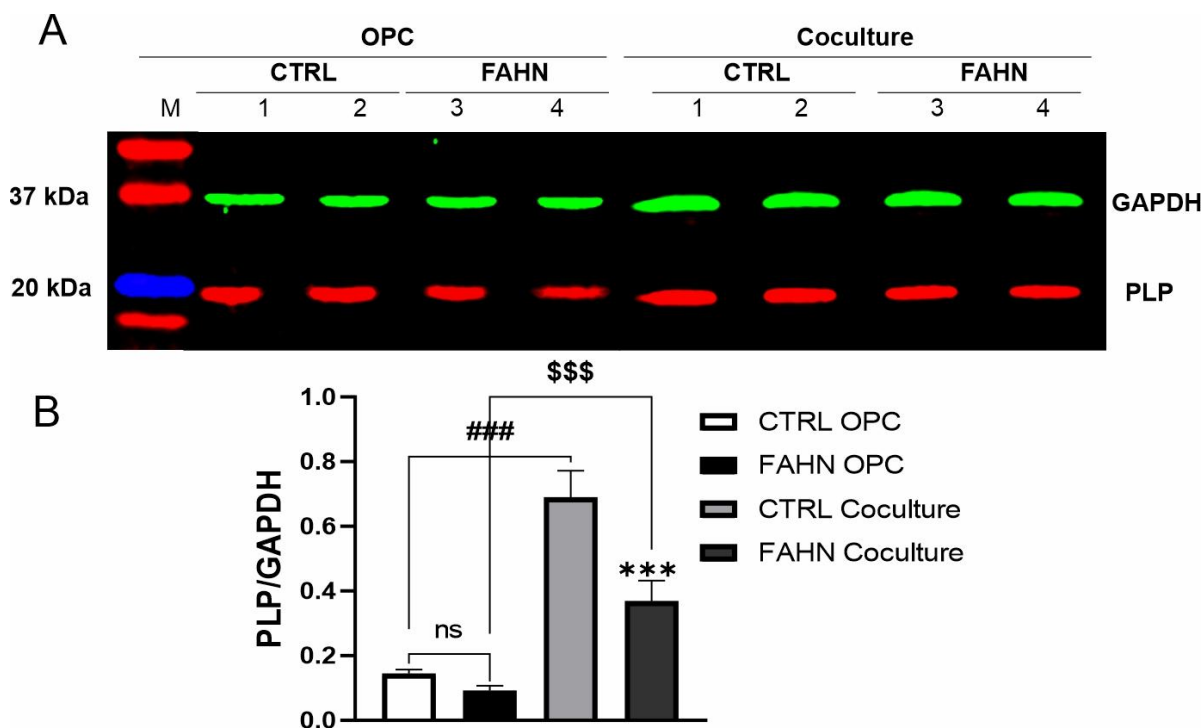


Figure 29: Analysis of myelin PLP protein in Oligodendrocyte Precursor Cells and coculture. (A) WB analysis of PLP protein levels in control and FAHN cell lines. The major band in OPC and coculture samples in both cell lines can be observed at 20 kDa. GAPDH 37 kDa was used for normalisation. The CTRL cell line shows a stronger signal in both cell types compared to FAHN. (B) The quantification of PLP protein in OPC revealed no significant difference. In contrast, the coculture demonstrated a significant increase in protein levels in both cell lines compared to OPC. A significant reduction of PLP protein was observed in FAHN coculture (mean \pm SD; N=14-16; *** = $p < 0.001$ for CTRL OPC vs. CTRL coculture, ### = $p < 0.001$ CTRL coculture vs. FAHN coculture, FAHN OPC vs. FAHN coculture \$\$\$ = $p < 0.001$).

4.6.3.2 Immunofluorescence staining of MBP and PLP in a FA2H-deficient cell line

The expression of myelin lipid proteins PLP and MBP in the same cell type was validated by immunofluorescence detection, which was used to visually examine the WB results. In order to gain insight into the localisation and interaction between MBP and PLP in OPC and in myelinating cells, colocalisation analysis was conducted. The colocalisation will provide us with valuable insights into the spatial compartmentalisation of MBP and PLP in OLs and their associated cellular structures. . The coculture of neurons and OLs was established by extending the culture period of these two cell types, as detailed in the corresponding section. The sublocalisation of MBP and PLP proteins was examined through immunofluorescence staining, followed by a colocalisation analysis of these two proteins (Figure 30). Visually, in the CTRL cell line, there is a notable overlap of the fluorescence signals from PLP and MBP, observed as pinkish staining indicative of colocalisation around the perinuclear area of the OLs and in their

early processes. Most OLs displayed extensive plasma membrane sheets. Furthermore, colocalisation was evident in cellular processes and myelin extensions of CTRL cell line (Figure 30 A, B, C). Conversely, in mature OLs from the FAHN cell line, as visually seen colocalisation of PLP and MBP staining was predominantly observed in cell processes and myelin extensions (Figure 930 D, E, F).

A quantitative assessment of this colocalisation was conducted using the Pearson correlation coefficient, which confirmed the visual observations. The CTRL cell line exhibited a Pearson correlation coefficient (CTRL: 0.3156 ± 0.066). In contrast, the Pearson correlation coefficient was significantly lower in the FA2H-deficient cell lines (FAHN: 0.2759 ± 0.044) (Figure 30 G). However, the morphology of the OL cells remained consistent across both cell lines.

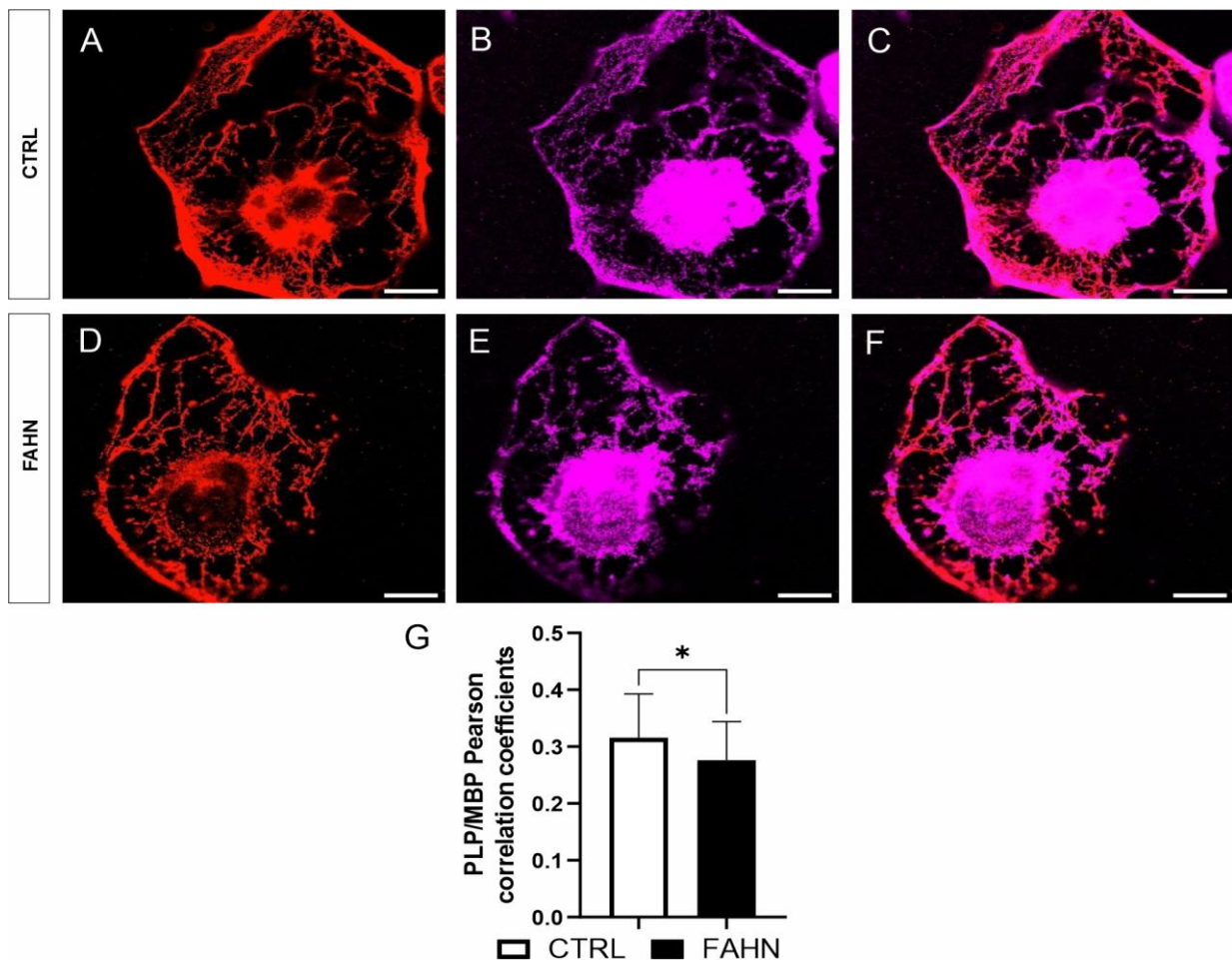


Figure 30: Colocalisation analysis of PLP-MBP in Oligodendrocyte Precursor Cells. Panels A to F show confocal microscopy images of the colocalisation of PLP in red and the myelin marker MBP in purple within OPCs. Panel G shows a quantitative analysis of PLP and MBP colocalisation. This analysis demonstrates a significantly reduced Pearson correlation coefficient in the FA2H-deficient FAHN cell line in comparison to the CTRL cell line. Data are expressed as mean \pm standard deviation with a sample size of N=38. Statistical significance is indicated (*= $p < 0.05$). Scale bars 20 μ m.

To investigate the level of colocalisation in the coculture of neurons and OLs, double immunostaining for PLP and MBP was conducted (Figure 31). In both cell lines, OLs exhibited a well-developed network of branching processes with neurons, indicative of successful myelination. The analysis of fluorescence signals for PLP and MBP in the coculture demonstrated a similar pattern to that previously observed in OLs. In the CTRL cell line, there was a robust expression of PLP and MBP, evidenced by the intense fluorescence signals in the axons and neuronal processes (Figure 31 A, B, C). Conversely, the FAHN cell line exhibited significantly weaker and more diffusely distributed fluorescence signals for PLP and MBP (31 D, E, F). Quantitative analysis indicated that the colocalisation of PLP and MBP as a total myelin content in the CTRL cell line was significantly higher than in the FAHN cell line (Figure 31 G). Furthermore, the percentage of PLP-MBP colocalisation was significantly greater in the CTRL cell line compared to the FAHN cell line (Figure 31 G). The FAHN cell line displayed low Pearson correlation coefficients. The low localization of PLP-MBP protein was significantly reduced compared to the CTRL cell line (CTRL: 0.6118 ± 0.02058 ; FAHN: 0.4866 ± 0.08426). Despite the reduction, the data still clearly indicate localization in the axons, confirming the presence of myelin formation.

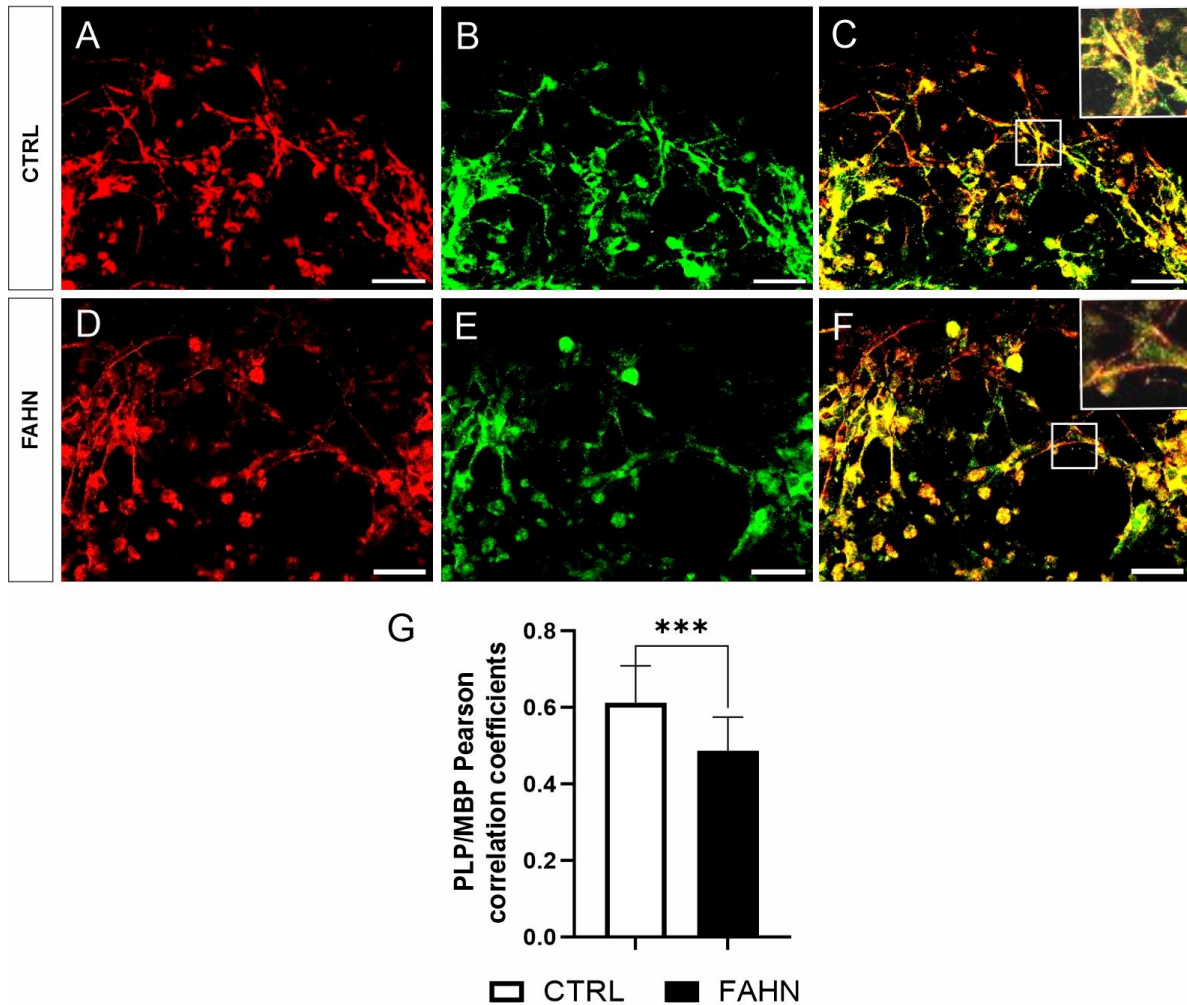


Figure 31: Colocalisation analysis of PLP-MBP in the coculture of neurons and OLs. (A-F) IF shows fluorescent signals of PLP (red) and MBP (green) in the somata of OLs and axonal processes of NDCs. (G) The calculation of the PCC shows a significantly reduced colocalisation of PLP and MBP in the FAHN cell lines compared to the CTRL cell lines. (Mean \pm SD; N=39-41; *** = $p < 0.001$ for CTRL). Scale bars 20 μ m.

Further analyses were conducted based on the observations of myelin proteins from WB and immunofluorescence studies. These analyses were performed to determine whether the observed localization of myelin proteins in the myelinating axon compartments was consistent with the observations made. Colocalisation analyses were conducted with PLP, MBP, and the neuronal cytoskeletal marker MAP2. The analysis of fluorescence signals for PLP (red) and MAP2 (purple) in coculture revealed a comparable pattern in both cell lines, indicating that each cell line has a comparable amount of myelin. Both the CTRL and FAHN cell lines exhibited robust expression of PLP and MAP2, as evidenced by the pronounced colocalisation observed in the axonal regions (Figure 32 A-F). The Pearson correlation coefficients observed in both cell lines indicated that the majority of PLP protein is located along the axons in the FAHN line, contributing to the formation of the myelin membrane in a manner similar to the

CTRL cell line. The Pearson correlation coefficients for colocalisation analysis were almost identical, with the CTRL line exhibiting a value of 0.8190 ± 0.01343 and the FAHN line demonstrating a value of 0.8056 ± 0.01223 .

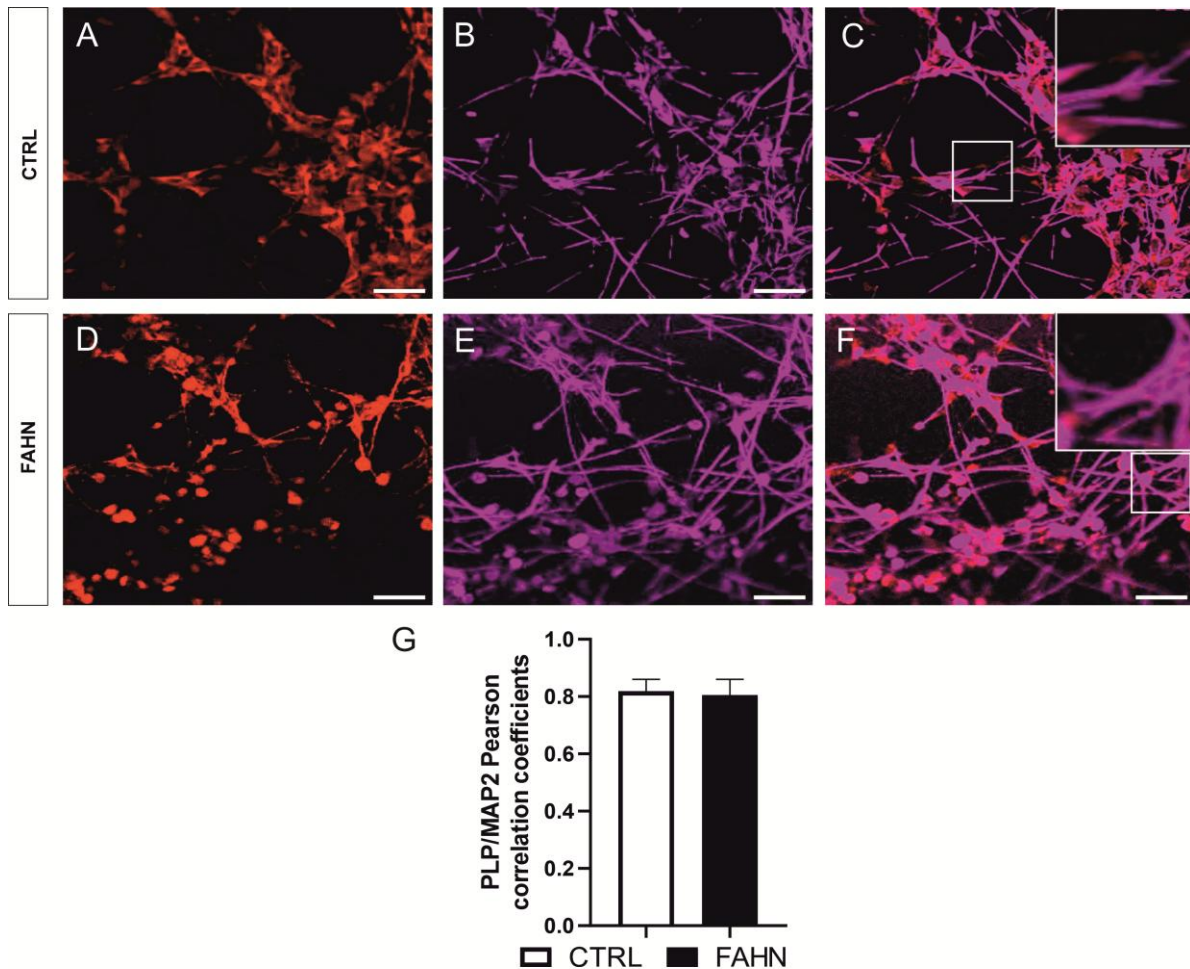


Figure 32: Colocalisation analysis of PLP-MAP2 in the coculture of neurons and OLs. Analyses A to F examine the colocalisation of the PLP in red and the MAP2 in purple within the coculture. The fluorescence images demonstrate a high degree of colocalisation between the PLP and MAP2 proteins in both cell lines, with strong fluorescence signals concentrated primarily in the axonal regions of the cells where the myelin sheath is forming. (G) A quantitative evaluation of the Pearson correlation coefficient indicates that there is no significant difference in colocalisation between the CTRL and FAHN cell lines. (Mean \pm SD; N=49; ns = $p < 0.05$ for CTRL). Scale bars 20 μ m.

An analysis was conducted to examine the colocalisation of MBP and MAP2 in order to determine if similar levels of these proteins are synthesised in coculture in a manner comparable to that observed for PLP. In Figure 32 A-C, within the CTRL cell line, the MBP protein, stained green, is observed to overlap or colocalised with the MAP2 protein, stained purple. Figure 27 C shows the colocalisation of these two proteins. In contrast, in the FAHN cell line, the green and purple signals show less colocalisation and are predominantly located in separate areas (Figure 32 D-F). Additionally, the extent of myelinating branches is reduced in the FAHN cell

line, resulting in cells that tend to cluster together in clumps. In contrast, the CTRL cell line has long branches with smaller somata. A quantitative analysis corroborates these visual observations, demonstrating a significantly reduced Pearson correlation coefficient in the FAHN cell line in comparison to the CTRL (Figure 32 G). In particular, the CTRL cell line exhibited a Pearson correlation coefficient of 0.8274 ± 0.04915 , while the FAHN cell line demonstrated a lower coefficient of 0.7782 ± 0.01283 , thereby confirming a reduction in MBP-MAP2 protein colocalisation in the FAHN condition.

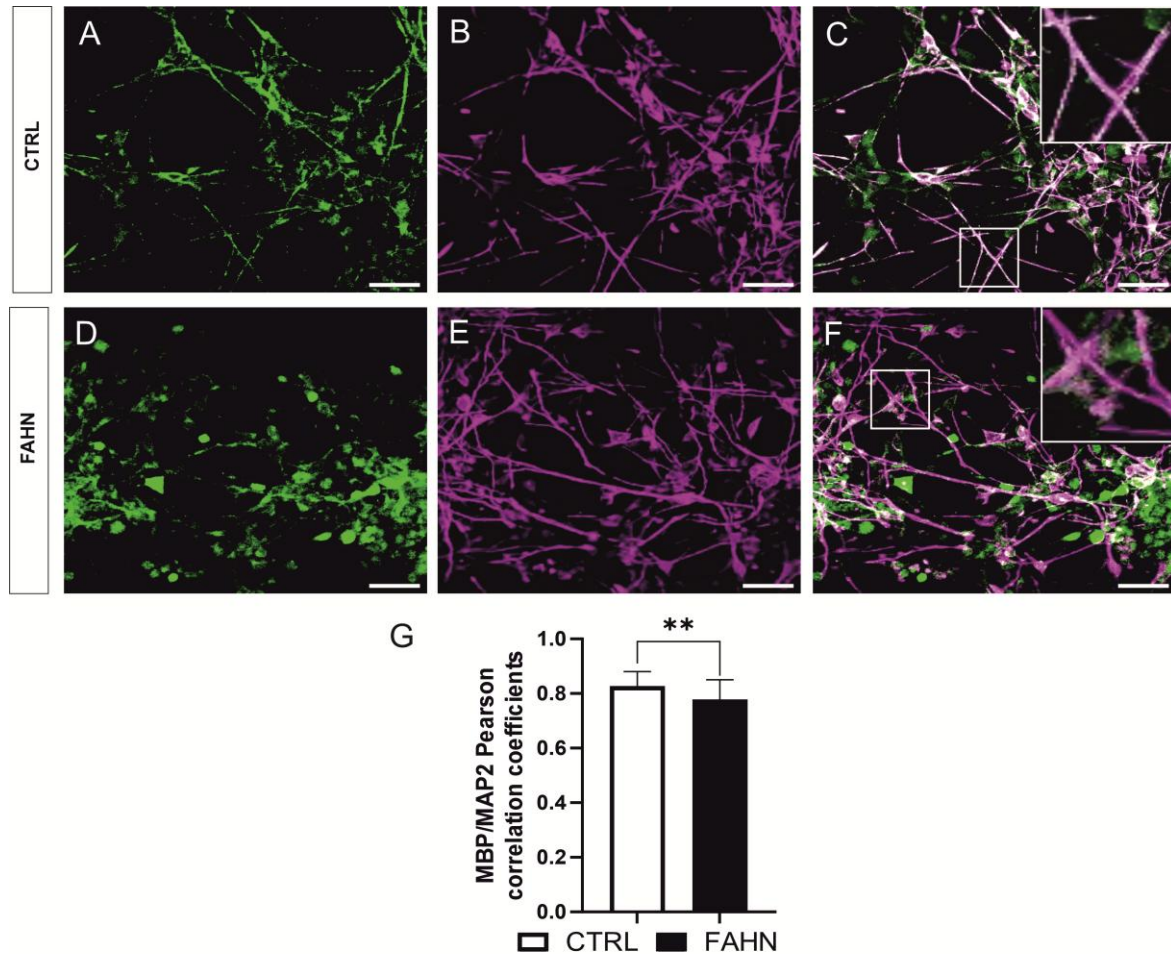


Figure 32: Colocalisation analysis of MBP-MAP2 in the coculture of neurons and OLs. (A-F) The confocal microscopy images demonstrate the localization of MBP (green) and MAP2 (purple) in the coculture. (A-C) The control cell line exhibits a robust colocalised signal of MBP and MAP2 in the axonal processes. (D-F) In the FAHN cell line, the colocalised fluorescence signal was reduced, and the fluorescence intensity of MBP was predominantly observed in the somata region. (G) The quantification of colocalisation revealed a significant reduction of the Pearson correlation coefficient in FA2H-deficient cell line compared to the control cell line (mean \pm SD; N = 49; ** = $p < 0.01$ to CTRL). Scale bars 20 μ m.

4.6.4 Myelin sheath examination and Ranvier node

The detection of the Ranvier node and examination of the myelin sheath structure in the FAHN cell line were achieved using the previously described coculture system. Myelinated axons were identified as positive for MBP. To analyse and access the Ranvier node, the potassium channel Kv7.2 was stained (Figure 33). Rapid, energy-efficient signalling along axons is facilitated by intricate subcellular arrangements of voltage-gated ion channels on myelinated axons. A recent example is the tight colocalisation of Kv7 potassium channels with MBP. Only axons that were myelinated and positive for the Kv7.2 marker were included in the analysis. Axons that were only positive for MBP or Kv7.2 were excluded. Figure 33 illustrates the immunostaining for MAP2, MBP and Kv7.2.

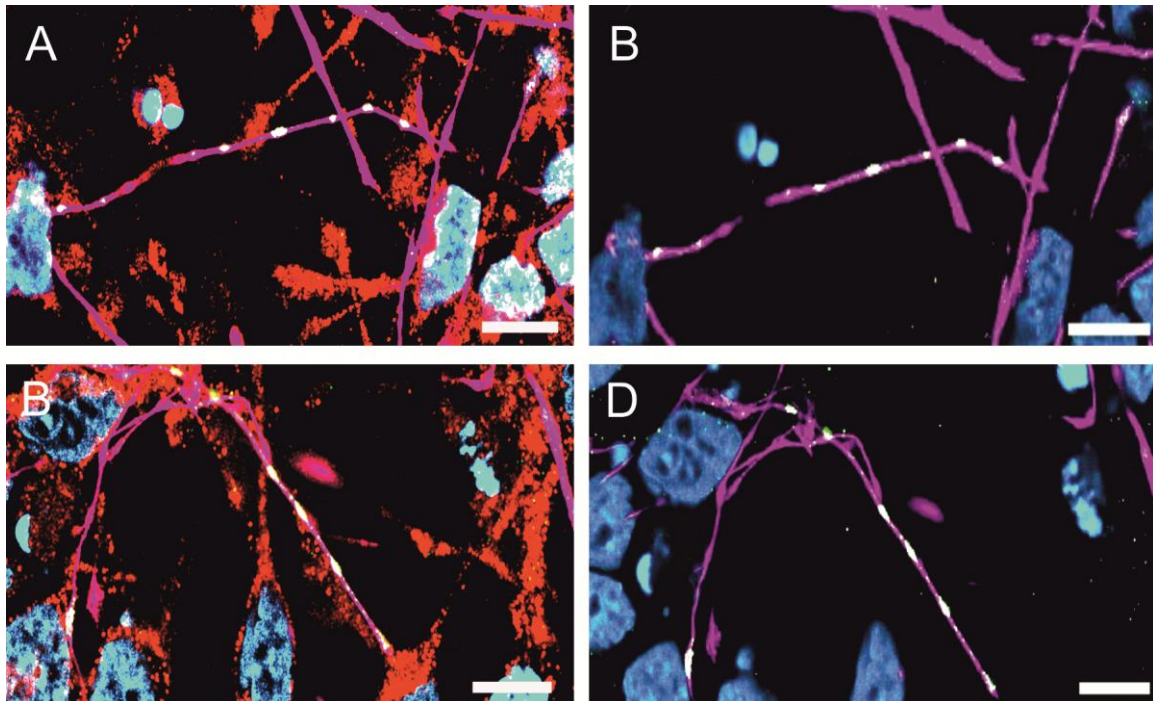


Figure 33: Expression of Kv7.2 channels in myelinated axon. (A, D) Representative confocal images of nodes of Ranvier and myelinated axon showing a node labelled with antibody to juxtapanodal marker Kv7.2 (green), myelin labeled with MBP (purple) and axon labeled with MAP2 (red). Image A and B is representing control cell line CTRL, while image C and D is representing FA2H deficient cell line FAHN. The scale is 20 μ m.

The quantification of the Kv7 channels in myelinated axons was conducted using high-resolution confocal imaging. The length of Kv7.2 aggregates between myelin domains was identified and measured using double immunolabeling (Kv7.2-MBP) from at least five coverslips in at least seven different experiments. Furthermore, in order to gain insight into the structure of the myelinated axon in FAHN, the number of nodes was counted, commencing from the first node and continuing to the last node at each axon. Additionally, the length of the

MBP-labelled internode between two Ranvier nodes was measured. The mean values for each of these parameters are presented in Table 4.3. A total of 40 axons were analysed. Figure 34 A depicts the staining of the CTRL cell line of myelinated axon, while image B represents the FAHN cell line. The fluorescence analysis of Kv7.2 and MBP staining in this figure describes the structure of the myelinated axon and the Ranvier nodes (Figure 34). The myelinated axon of the CTRL cell line in Figure 33 A displays three Ranvier nodes and two internodes of almost identical length. In contrast, the FAHN myelinated axon has four Ranvier nodes and three internodes of different lengths (Figure 34 B). The general organisation of the nerve was markedly different from the CTRL cell line, with normal nodal-like structures being sparse and a dense accumulation of Kv7.2 evident. Occasionally, node-like formations were observed at short and long internodal intervals. This visual finding was supported by quantification. According to the statistical analysis and observations of measured, a significant increase in internode length was observed in the FAHN cell line (FAHN: 63.8 μm for MBP-stained fibres) in comparison to control fibres (CTRL: 47.9 μm for MBP-stained internodes) (Figure 34 C). The relative frequency distribution plots for internode length of the CTRL cell line nerves were consistent for MBP staining (CTRL: 47.98 \pm 13.83 μm), whereas the FAHN cell line fibres showed a significant reduction in internode calibre (FAHN: 61.80 \pm 3.49 μm for MBP-stained fibres) (Figure 34 D). The number of nodes per 100 μm axon length was also quantified on a total of 40 axons. The FAHN cell line exhibited a significantly lower number of nodes per 100 μm axon (CTRL: 2.16 nodes per 100 μm axon) in comparison to the CTRL cell line, which demonstrated a significantly higher number (FAHN: 1.55 nodes per 100 μm axon) (Figure 34 E).

Table 4.3: Measurements on myelinated axon

	CTRL cell line	FAHN cell line	P value
Node Length (μm)	3,024 \pm 0.125 *	6,482 \pm 0.240	p<0,0001
Internode Length (μm)	47.98 \pm 13.83 *	61.80 \pm 3.49	p<0,0031
No. of nodes per 100 (μm) axon	2,162 *	1,558	p<0,0039

The values are presented as the mean \pm standard deviation. * Statistical difference between the CTRL cell line and FAHM cell line axons stained for MBP and Kv7.

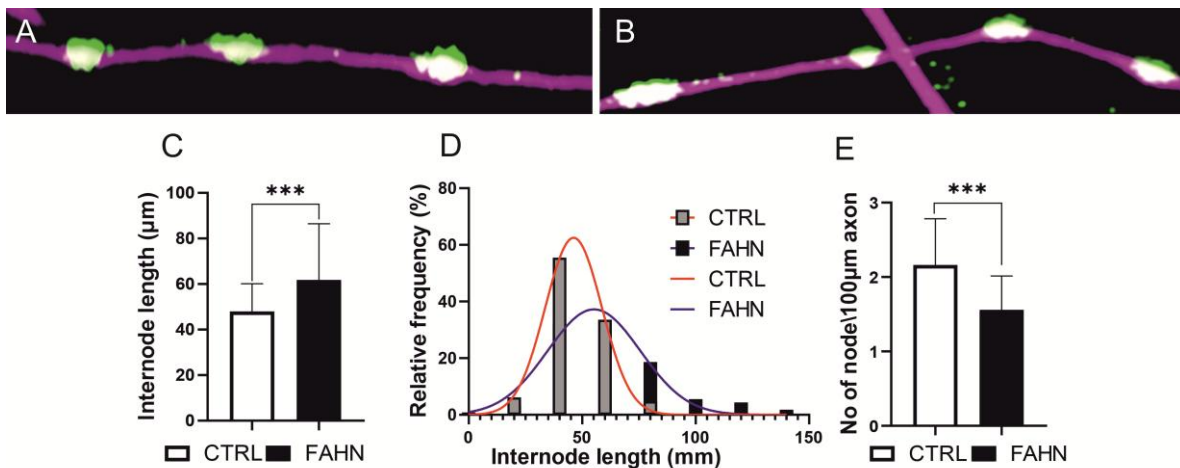


Figure 34: Structure of myelinated axon in FAHN. The **A** (CTRL) and **B** (FAHN) nodes of Ranvier in both cell lines are highlighted and shown in high-resolution images. The nodes of Ranvier were identified as Kv.7.2-positive clusters (green) and myelinated fibres positive for MBP (purple). The plots in **(C, D, E)** are presented as mean \pm s.m. **(C)** illustrates an example of an internode length measurement. Nodes are identified from one node to another node and MBP labelling is performed. **(D)** Displays the distribution of internode lengths, with fitted lines indicating Gaussian distributions in the control (red) and FAHN (blue) groups. **E** plot represent quantification of means number of nodes per 100 μm axon. Mean \pm SD; N = 40; ** = $p < 0.01$, *** = $p < 0.001$ to CTRL. The scale is 5 μm .

The visual distinction between the sizes of the Ranvier nodes in Figure 35 is notable. In particular, the node difference is illustrated in Figures 30 G and H, which represent the CTRL (Figure 35 A) and FAHN (Figure 35 B) cell lines, respectively. As is evident from the fluorescence staining in images A and B, the FAHN cell line exhibited inconsistent node lengths in comparison to the CTRL cell line, where node lengths were predominantly uniform. This is illustrated by the quantification in Figure 30 C, which shows that the CTRL cell line had a mean node length of 3.02 ± 0.12 , while the FAHN cell line had a mean node length of 6.48 ± 0.240 . The relative frequency distribution plots for node length in the FAHN cell line demonstrated a broad distribution, with the minimum node length at 2.22 μm and the maximum at 9.98 μm , which was significantly longer than those in the CTRL cell line (min: 2.53 μm ; max: 4.86 μm). In summary, the FAHN cell line exhibited poorly structured myelinated axons with variable internode lengths and a wide range of node densities. Some axons exhibited a high density of nodes, while others displayed a low density, with only one or two nodes per 100 μm . This resulted in a disorganized myelinated axonal structure.

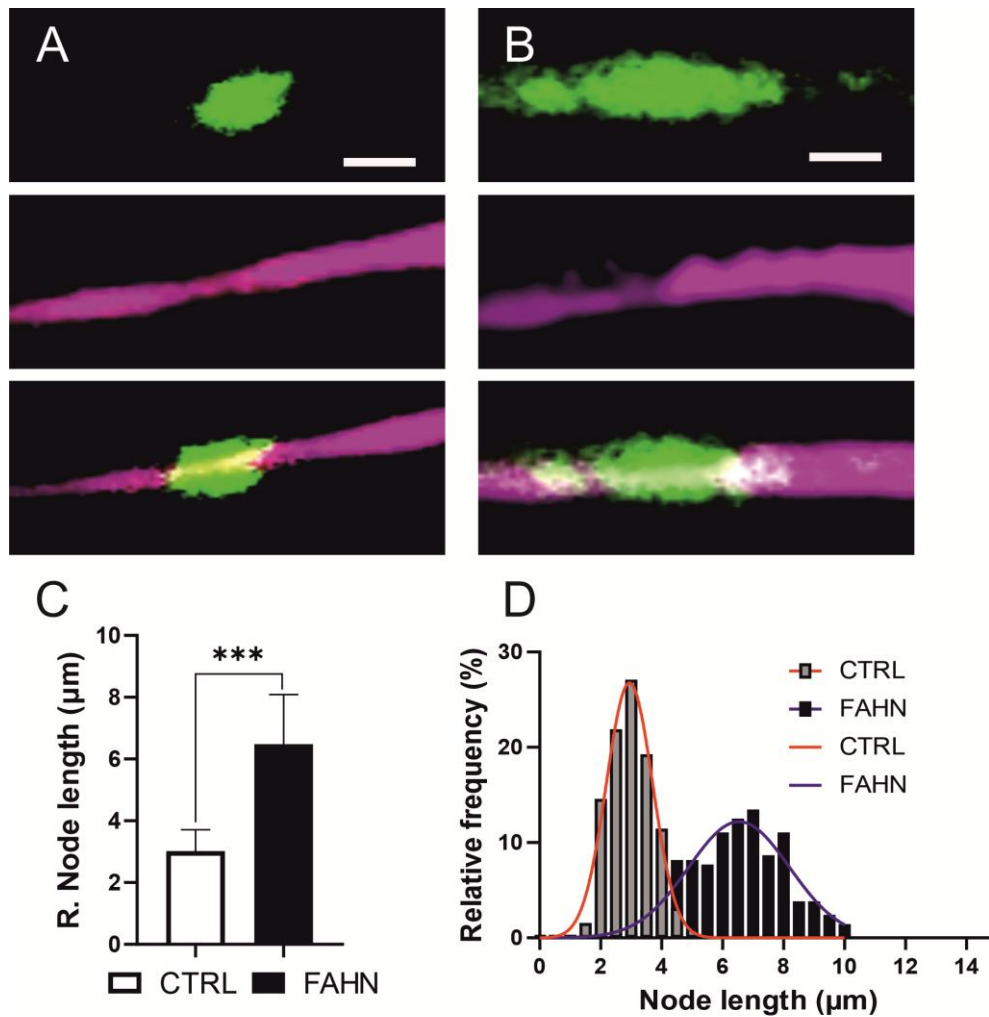


Figure 35: Expression of Kv7.2 channels in myelinated axon, node of Ranvier. **A** represent CTRL cell line, **B** represents FAHN cell line. Confocal image of a single nerve node of Ranvier showing the node labelled with antibody to Kv.7.2 (green) and axon labelled for MBP (purple). Mean \pm s.m. of the node lengths measured in the axon (**C**). Distribution of Ranvier node lengths (**D**), Fits are Gaussian curves, $\{A/[r(2p)]\} \exp \{- (L-M)^2 / (2r^2)\}$, with parameters $A = 26,74 \mu\text{m}$, mean length $M = 2,945 \mu\text{m}$, $r = 0,9878 \mu\text{m}$ in CTRL and $A = 12,19 \mu\text{m}$, $M = 6,540 \mu\text{m}$, $r = 1,337 \mu\text{m}$ in FAHN. mean \pm SD; $N = 192-207$; *** = $p < 0.001$ to CTRL. The scale is $2 \mu\text{m}$.

4.7 Analysis of autophagy

To assess autophagy in FAHN disease, NDCs were subjected to *in vitro* WB experiments against key markers, including p62 (see Figure 36) and LC3B (see Figure 37). This was observed under a variety of experimental conditions. To study the onset of autophagy, the fusion of autophagosomes with lysosomes was inhibited by treating the cells with bafilomycin A1 (BafA1) for 6 hours. BafA1 is a known inhibitor of the late stages of autophagy, preventing the fusion between autophagosomes and lysosomes by inhibiting the vacuolar H⁺-ATPase. This inhibition was expected to result in the accumulation of both p62 and autophagosomes (LC3BII/LC3BI). In the absence of treatment, the expression of the p62 protein was found to be significantly increased in the FAHN cell line compared to the CTRL cell line (Figure 36A). However, when cells were treated with BafA1 for a period of six hours, it can be observed that the expression of p62 only increased in the control cell line CTRL BafA1, while the mutant cell line FAHN BafA1 did not show any significant difference (Figure 36 B). In the CTRL cell line, the amount of p62 protein increased by 54%, whereas in the FAHN cell line, the amount of p62 protein increased by 26%.

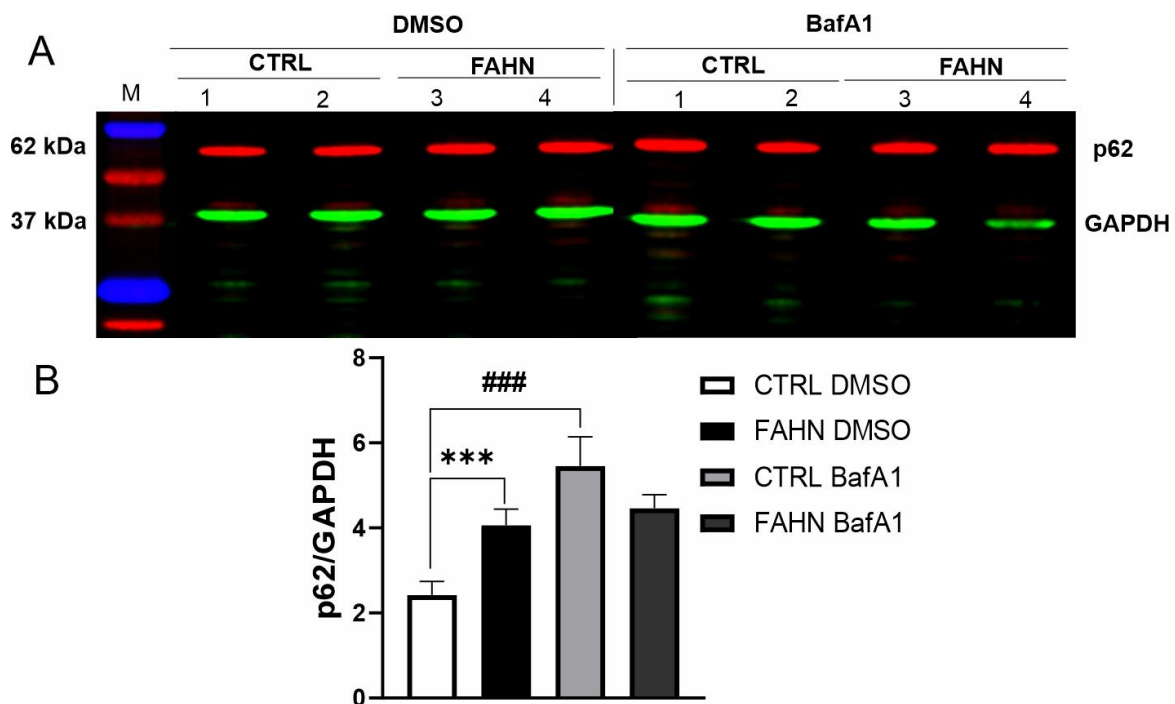


Figure 36: Analysis of the expression of p62 during autophagy. (A) Representative WB of p62 62 kDa expression under basal conditions and after treatment with BafA1. GAPDH 30 kDa acted as an internal control. (B) The significant difference in p62 expression was observed under basal conditions. After treatment with BafA1 for 6h, only the CTRL cell line demonstrated an increase in expression. The data were analysed using a one-way ANOVA with a post-hoc Tukey test. The results showed a significant difference between the CTRL DMSO and FAHN DMSO groups $***=p < 0.001$ and between the CTRL DMSO and CTRL BafA1 groups $###=p < 0.001$).

The LC3BII/LC3BI ratio was employed to ascertain autophagosome formation under identical conditions. In a manner analogous to p62, LC3B expression was analysed both under basal conditions and following BafA1 treatment (Figure 37). Under basal conditions (DMSO), a markedly elevated quantity of LC3BII was observed in the FAHN cell line, thereby corroborating the hypothesis of impaired degradation of these vesicles and the material taken up inside them. Inhibition of the fusion of autophagosomes and lysosomes with BafA1 resulted in a significant increase in LC3BII levels in the CTRL cell line, while in FAHN BafA1 remain similar to the FAHN DMSO. This suggests that the *FA2H*-deficient FAHN cell line had probably already reached the maximum number of autophagosomes and their production could not be increased further

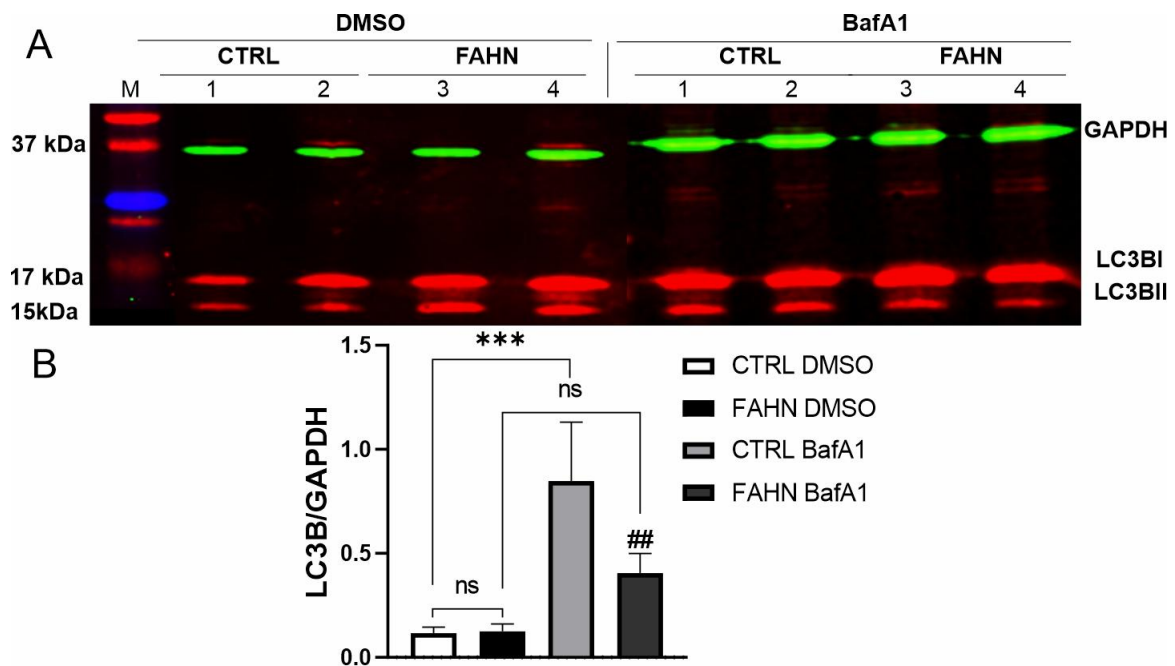


Figure 37: Analysis of LC3B expression during autophagy. (A) Representative WB of LC3BI and LC3BII expression under basal conditions and after treatment with BafA1. GAPDH acted as an internal control. (B) Under basal conditions, an increased LC3BII level was not detectable in the FAHN cell line compared to the control. Following a six-hour treatment with BafA1, the control cell line demonstrated the capacity to enhance the conversion of LC3BI to LC3BII, whereas the FAHN cell line exhibited no significant increase. The mean \pm SD values for the control and FAHN cell lines are presented below. The data were analysed using a one-way ANOVA with a post-hoc Tukey test. The results showed a no significant difference between the CTRL DMSO and FAHN DMSO groups ns= $p < 0.05$ and between the CTRL DMSO and CTRL BafA1 groups ***= $p < 0.001$).

5 Discussion

5.1 FAHN iPSCs model

5.1.1 iPSC generation

The initial success in establishing the first human FAHN patient iPSC line represents a significant milestone for this disease, as these iPSCs are pivotal in advancing our understanding of the pathophysiological mechanisms involved. The primary goal was to develop a dependable *in vitro* myelination model using iPSCs, particularly those obtained from patients with FAHN. This FAHN iPSCs model serves two purposes: it enables thorough investigation into the biology and pathobiology of myelin formation, and it provides a valuable platform for identifying pharmacological compounds that affect human oligodendrogenesis and myelination. Given the limited availability of *in vitro* models for human myelination, I have made a significant contribution by establishing an OLS-neuron culture model that demonstrates robust myelin formation and the organization of myelinated axon structures. The model's thickness is physiologically relevant, and the versatility of generating OLS and neurons from iPSCs derived from both control and FAHN cell lines has been demonstrated. My findings indicate that there is temporal predictability and, to some extent, specificity to myelin development. Furthermore, it was demonstrated that modulation of myelin formation is achievable at both the individual neuronal cell level and across the entire coculture. This research represents a significant advancement in the field of *in vitro* models for human myelination, offering promise for future studies aimed at exploring potential therapeutic interventions (Madhavan et al. 2018; Sarah Kuhn et al. 2018; Donna L. McPhie et al. 2018; Chanoumidou et al. 2019).

5.1.2 OPCs generation

In addressing the challenge of *in vitro* models for human myelination, this thesis presents an innovative OLS-neuron culture model derived from iPSCs of both control and FAHN cell lines. This model is a substantial contribution, illustrating physiologically relevant myelin thickness and organization of myelinated axon structures. Notably, the generated OLS exhibit a temporal predictability and specificity in myelin development, highlighting the advanced maturity and earlier development of nascent myelin sheaths compared to other studies. For instance, MBP+

OLs appear by day 10 post-transfection, markedly earlier than in protocols where induction takes around 90 days (Anna M. Speicher et al., 2019; Douvaras et al., 2019).

The discrepancies in myelin development protocols, such as those using patterned EB without RA and prolonged exposure to growth factors, often result in high microglial content and weaker neuronal connections (Douvaras et al., 2014; Douvaras et al., 2019). These approaches contrast sharply with this study's method, which supports myelin compaction and nodal domain organization akin to *in vivo* conditions. Our results align and extend findings from various other studies (Madhavan et al., 2018; Sarah Kuhn et al., 2018; Donna L. McPhie et al., 2018; Chanoumidou et al., 2019), reinforcing the utility of iPSC-derived OLs in modeling CNS myelination. Furthermore, established models, such as the Shiverer mouse utilized by Rasband et al. (1999), underscore the potential drawbacks in myelin sheath formation due to deficiencies in key proteins like MBP.

5.1.3 Coculture generation

The coculture systems employed in this research have demonstrated notable improvements in stability and maturity, allowing for extended periods of myelination observation which is essential for exploring the dynamics of myelin development and remyelination processes. Utilizing a direct transfer method for OPCs without the need for purification via MACS bead separation circumvents the potential for cell aggregation and damage, facilitating quicker and healthier cell recovery (Figure 17). This method underscores a distinct advantage over other studies which have not reported such efficient transfer techniques (Madhavan et al. 2018; Douvaras et al. 2014; Douvaras et al. 2019; Fossati, McPhie et al. 2018).

This research also highlights the sophisticated development of myelin in the coculture system, which more closely resembles *in vivo* conditions with the organization of compact myelin and properly structured nodal and paranodal domains. Such structural intricacies are essential for the functional properties of neural circuits and have been extensively described (Rasband et al. 1999; Uncini et al. 2013). The methodologies applied here align with those used in studies like Rasband et al. (1999), which observed the capacity of OLs to wrap axons, even though deficiencies in MBP expression impeded compact myelin formation.

Despite the advancements, this model's iPSC-derived OLs still present a limitation in coculture stability, lasting only up to 11 weeks (García-León, et al. 2020; Chanoumidou, et al. 2020).

This restricts the long-term study of myelination and is a challenge that must be addressed to facilitate ongoing research into chronic neurological conditions. Moreover, the system predominantly produces a uniform type of OLs, not accounting for the intrinsic differences identified between OLs from various CNS regions such as spinal cord versus forebrain (Bechler et al. 2015; Leong et al. 2014; Jäkel et al., 2019). Addressing this gap could enhance the relevance and applicability of the model to various neurodegenerative and developmental disorders. The ongoing research into the transcriptome of OLs also suggests unexpected diversity within similar areas, hinting at the complex regulatory mechanisms influencing OL differentiation and myelination (Leong et al. 2014; Jäkel et al., 2019). This points to a nuanced understanding of OL biology that could be crucial for developing targeted therapies for diseases involving myelin dysfunction.

5.2 Pathophysiology of FAHN disease

FA2H is a protein in the fatty acid hydroxylase/desaturase gene family, functioning as an ER-localized NAD(P)H-dependent monooxygenase. It is a major producer of 22hFA or 2hFA-ceramides, critical for oligodendrocytes (OLs) in myelin production. The enzyme 2-hydroxylase, encoded by the human *FA2H* gene, plays a pivotal role in biosynthesizing 2-hydroxylated sphingolipids. The molecular architecture of the enzyme, comprising three domains, emphasizes the cytochrome b5 domain as the primary structural backbone, positioning *FA2H* among lipid biosynthetic enzymes involved in oxidative reactions, akin to fatty acid and sphingolipid desaturases. Research by Eckhardt et al. highlights the cytochrome b5 domain's critical function in *FA2H* activity, showing significant reduction in enzymatic function when this domain is absent (Eckhardt et al., 2005). This indicates the cytochrome b5 domain's involvement in an electron transport chain, suggesting its direct role in FA2H's enzymatic activity. Furthermore, Eckhardt's recent research proposes an alternative pathway activated in the absence of the intramolecular cytochrome b5 domain, involving a microsomal cytochrome b5 domain with reduced efficiency, leading to impaired electron transport or protein accumulation in the ER membrane (Matthias Eckhardt et al., 2023; Maldonado et al., 2008; Alderson et al., 2009; Hama et al., 2009).

The research by Zöllner and colleagues significantly advanced understanding *FA2H*'s functional implications by creating the first FA2H knockout mouse (*FA2H*^{-/-}) (Zöllner et al., 2008). This model, carrying a missense mutation in exon 3 and 4 within the cytochrome b5 domain, was studied across different life stages, showing reduced *FA2H* expression and altered GalCer levels in young *FA2H*^{-/-} mice (Zöllner et al., 2008). These findings align with Eckhardt et al.'s earlier

work, providing further evidence for an alternative pathway affecting sphingolipid metabolism (Eckhardt et al., 2023). Parallel studies by Potter and colleagues with a similar *FA2H*^{-/-} mice model showed comparable results in aging mice (Potter et al., 2011). Hama and colleagues demonstrated that the same mutation led to premature truncation of the FA2H protein, substituting a cysteine for a highly conserved arginine residue (Hama et al., 2009). Predictive modeling algorithms, including PolyPhen, SIFT, and SNAP, indicated this transition as deleterious, potentially affecting protein folding (Hama et al., 2010). These insights into the *FA2H*-deficient cell line highlight the complex consequences of genetic changes on enzyme structure and function.

FA2H expression varies across tissues and cell types (Eckhardt et al., 2023). Studies on *FA2H*^{-/-} mice lines by Zöller et al. and Potter et al. showed significant reduction in *FA2H* expression in the brain and PNS, especially in aged mice (Zöller et al., 2008; Potter et al., 2011). The studies demonstrated *FA2H* activity's crucial role in synthesizing FA2H-sphingolipids (FA2H-SL) in these neural tissues. Notably, while *FA2H* is widely expressed, most FAHN-related symptoms in mice models manifest due to *FA2H* loss specifically in OLs. This raises questions about the mechanisms linking changes in α -hydroxylated GalCer in the myelin sheath to axonal degeneration, offering insights into neurodegenerative processes associated with *FA2H* deficiency.

Abundant expression of *FA2H* is particularly evident in the brain, PNS and intestinal tract, with myelinating cells such as OLs and Schwann cells prominently expressing *FA2H* (Lin Guo et al. 2012; Kota et al. 2014). Studies of OLs lacking the *FA2H* gene revealed normal differentiation in vivo, with normal OPCs and mature oligodendrocyte numbers (Zöller et al., 2008; Potter et al., 2011). However, the stability of the myelin sheath and irregular myelin gene expression during postnatal development were demonstrated (Zöller et al., 2008). The precise mechanism of FA2H remains somewhat elusive, but Eckhardt's review proposes a hypothesis regarding FA2H's interaction with proteins, particularly in sphingolipid trafficking and microdomains (Eckhardt et al., 2023). Eckhardt discusses findings by Simons, suggesting that FA2H-SL significantly influences membrane microdomains' structure and stability, thereby affecting membrane and protein trafficking (Simons et al., 2011)

Indeed, in the *FA2H*-deficient cell line examined in our study, a compound heterozygous configuration involving a missense mutation in the cytochrome b5 domain and a frameshift in the histidine motif domain was utilized. In our in vitro examination of FA2H using WB analysis of NDCs, the CTRL cell line exhibited high expression of FA2H protein. The same method

applied to OPCs in the CTRL cell line showed strong FA2H protein expression, with a notably higher signal in OPCs than in NDCs. In contrast, when the same analyses were performed on the FAHN cell line, the expression of FA2H protein in NDCs was significantly reduced compared to the CTRL cell types (Figure 18 and 19). This reduction was also observed in FAHN OPC cells. The results from WB in both cell types demonstrated a significant reduction in the amount of FA2H protein in the FAHN cell line ($p < 0.0263$). Notably, OPCs exhibited higher FA2H expression, consistent with their increased requirement for FA2H in ceramide production, which is critical for myelin sheath formation. This synthesis capability for hydroxylated fatty acids explains the higher levels of FA2H found in OPCs in both cell lines.

Another area of interest in this part of the study is the localization of FA2H in neurons and OPCs. In neurons, the protein is distributed throughout the cell, whereas in OPCs it is concentrated in cytoplasmic regions, forming cytoplasmic dots around the nucleus in the CTRL cell line. However, the fluorescence intensity measured in FAHN cell line NDCs showed different localization compared to the CTRL cell line, including a significant reduction of signal. Similar results were obtained in OPCs, where the expression and localization of FA2H protein were predominantly different and lower than in the CTRL cell line.

It is important to note that the findings of this study on the expression and localization of FA2H in a FAHN cell line are consistent with those of previous studies conducted by other research groups. These results demonstrate that in any cell type, whether NDC or OPC, and in both WB and IF analyses, the expression of the FA2H protein is significantly reduced. Furthermore, the consistency between our findings and those of other research groups underscores the predominant presence of FA2H in myelinating cells, emphasizing its central role in FA2H biosynthesis in the CNS. Compared to the differentiation and morphology of OPCs in *FA2H*^{-/-} mice models described in this study, our observations are consistent with findings in the FAHN cell line, which demonstrated robust growth, proliferation, and differentiation, coupled with morphological stability. However, the number of myelinated axons was reduced, and the colocalization and creation of compact myelin were visually distinct from those observed in the control cell line. Nevertheless, FA2H protein is predominantly expressed in OPC cells in both cases, thereby confirming its crucial role and importance in OPCs by providing GalCer for the construction of compact and stable myelin membranes. In conclusion, this comprehensive study has enhanced our understanding of the multifaceted roles of FA2H in cellular processes, including membrane dynamics and trafficking (see section 5.5). These insights not only deepen our comprehension of basic biology but also open potential avenues for exploring the

implications of *FA2H* dysfunction in pathological conditions associated with disrupted membrane dynamics and sphingolipid metabolism.

5.3 Impairment of Myelin sheath in FA2H-Deficient Cells

This section of the study examined myelin-associated proteins in OLs and their cocultures. OLs are crucial in forming the myelin sheath in the CNS, adeptly constructing specialized membrane layers that facilitate nerve impulse transmission (Anitei and Pfeiffer, 2006; Kramer et al, 2001; Larocca et al, 2002; Fernandez et al, 2000). These membranes consist of various lipid proteins, and maintaining their expression balance is essential for developing a stable myelin sheath.

Research on FAHN revealed lower MBP protein expression in FA2H models (Maldonado et al., 2007; Kruer et al., 2010; Pohl et al., 2011; Traka et al., 2010). It was suggested that GalCer protein expression, controlled by the *FA2H* gene, regulates MBP protein levels in mature OLs. *FA2H*^{-/-} mice models also demonstrated a significant decrease in MBP and PLP protein levels, leading to unstable myelin sheaths (Zöller et al., 2008; Maldonado et al., 2007; Kruer et al., 2010; Potter et al., 2012; Pohl et al., 2011; Traka et al., 2010).

A detailed study by Zöller et al. (2008) analyzed various myelin proteins in *FA2H*^{-/-} mice at different life stages. Early life (P10) showed downregulation of GalCer, MAG, MBP, PLP, and MAL proteins. By four weeks, protein expression was upregulated, showing no significant differences. However, at 18 months, all myelin proteins decreased in whole brain homogenates, likely linked to demyelination observed in FAHN in previous studies (Alderson et al., 2005; Eckhardt et al., 2005; Uchida et al., 2007; Hama et al., 2008; Kruer et al., 2010; Potter et al., 2011; Garone et al., 2011; Tonelli et al., 2012; Cao et al., 2013; Rupps et al., 2013; Donkervoort et al., 2014; Hashemi et al., 2023; German et al., 2023; Lidangzhi Mo et al., 2024). Myelin proteins were expected to downregulate during the prenatal period, with demyelination indicated in later life.

Another study by Wia Barin and her team (1999a; 2010) found that MBP plays a complex role in myelin assembly, influencing the distribution pattern of its isoforms in the membrane. MBP contributes to signaling, membrane reorganization, and cytoskeletal dynamics (Gould et al., 1999). PLP and MBP are pivotal in forming myelin membrane microdomains, aiding intracellular transport and other functions (Schneider et al, 2005; Baumann et al, 2001; Simons et al., 2000; Pernber et al., 2008). They also help solidify the membrane by moderating electrostatic repulsion between lipids (Klugmann et al., 1997; Hu et al., 2008).

De Bruins highlighted the structural variation in myelin protein, particularly MBP, suggesting its phosphorylation leads to raft localization (De Bruins et al., 2005). This is further supported by studies indicating that carbohydrate moiety variations significantly influence its spatial distribution within the myelin, impacting microdomain organization and targeting functions similar to lectins (Fasano et al., 2008).

The present study focused on two of the most prevalent myelin proteins, PLP and MBP. These proteins serve as exemplary models for the study of their localisation within the myelin sheath, particularly in areas of differing density. The objective of this detailed analysis was to elucidate the spatial distribution and potential interactions of these critical myelin proteins within the sheath structure. Western blot data of OPCs revealed that the protein expression in the control cell line exhibited a robust signal for both MBP and PLP. However, the data from the FAHN cell line indicated a reduction in the expression of both PLP and MBP in the same cell type when compared to the CTRL cell line.

Furthermore, the study demonstrated that when OPCs were cocultured with neurons, Western blot analysis exhibited a robust expression in the control cell line. However, a reduction in the expression levels of MBP and PLP was observed in the FAHN cell line. It is notable that the expression levels of both myelin proteins in OPCs are lower than those observed in coculture. This is to be expected, given that both proteins are upregulated during the myelination process. The WB data, however, indicate that *FA2H*-deficient cells are unable to produce sufficient quantities of the two proteins in question for the synthesis of the compact myelin sheath (see Figures 22 and 23).

The colocalisation of MBP and PLP observed by immunofluorescence staining (Figure 24) in OPCs demonstrates that PLP was predominantly localised intracellularly, with only a minimal amount colocalised with MBP. The analysis yielded a low Pearson correlation coefficient for the CTRL cell line. The Pearson correlation coefficient was observed to be higher in the CTRL cell line when OPCs were cocultured with neurons. When this experiment was conducted in the FAHN cell line, a very low Pearson correlation coefficient was observed in the OPCs. Moreover, when OPCs and neurons were cocultured, the low Pearson correlation coefficient was again lower than that observed in the CTRL cell line. It has been previously demonstrated that the expression of these proteins is dependent on the regulation of other myelin lipid proteins, and mislocalisation results in the instability of the myelin sheath (Redmond et al., 2016). The studies conducted by Boiko and Winckler (2006) and Trajkovic et al. (2006) demonstrated that neuronal signals play a role in regulating the trafficking and formation of

myelin membranes of PLP (Boiko et al., 2006; Trajkovic et al., 2006). Our studies and previous research on FAHN disorder have reached the same conclusion: *FA2H*-deficient cells have difficulty expressing these two proteins (Zöller et al., 2008; Maldonado et al., 2007; Kruer et al., 2010; Potter et al., 2012; Pohl et al., 2011; Traka et al., 2010).

In the same chapter, we sought to ascertain the quantity of myelin proteins present in the coculture. To this end, we conducted a colocalization analysis of PLP and MAP2 (Figure 27). Contrary to expectations based on previous data, no decrease in the quantity of these proteins or their colocalization was observed in the FAHN cell line. Conversely, the colocalisation of MBP and MAP2 aligned with the results of previous studies, indicating a reduction in MBP-MAP2 protein colocalisation (Figure 28). This indicates that the FAHN cell line encountered challenges in expressing MBP, resulting in a reduction in myelin protein production compared to the control.

In light of these findings, the precise manner by which myelin proteins facilitate the clustering of myelin membrane rafts and the underlying mechanisms of this process remain unclear. The data suggest the existence of a potential mechanism for raft clustering. This raises the question of how this is achieved. Research conducted by Fitzner and colleagues indicates that neurons are responsible for the expression of the cholesterol-binding protein PLP on OLs (Fitzner et al., 2006). This finding prompted a study of its role in altering the plasma membrane configuration (Fitzner et al., 2006). Given that MBP interacts with the inner layer of the oligodendroglial plasma membrane, it can be considered an alternative mediator of raft clustering. Nevertheless, evidence from FAHN indicates that the reorganization of the myelin sheath membrane is dependent on the function of MBP (Eckhardt et al., 2023). The functionality of MBP is influenced by its interactions with other myelin-associated proteins, in particular GalCer (De Vries et al., 1997). Additionally, Fitzner's research suggests that neurons regulate the post-translational modification of MBP, which further complicates its role (Fitzner et al., 2006).

It has been suggested that neurons regulate the post-translational modification of MBP, which plays a crucial role within OLs by aligning myelin layers vertically and aggregating lipid bilayers horizontally, thus forming and reinforcing expansive raft domains (Boggs et al., 2006; St. Johnston et al., 2005). This function of MBP as a lipid coupler might be compromised in FAHN, as evidenced by studies showing reduced MBP expression during myelination, potentially impairing the formation of the myelin MBP cytoplasmic bilayer membrane (Kruer et al., 2010; Potter et al., 2011; Cao et al., 2013; Rupps et al., 2013; Donkervoort et al., 2014; Hashemi et al., 2023; German et al., 2023).

The varied structural isoforms of MBP in the FAHN cell line bring uncertainty about their role in lateral membrane localization, which is critical as it may influence their incorporation into vesicles for transport. The reduction in MBP quantity and expression in these cell lines correlates with instability in the myelin sheath and contributes to demyelination, as shown in FA2H-deficient mouse models. The synthesis of MBP depends on the translation of the GalCer protein, indicating that MBP deficiency in FAHN results from impaired FA2H synthesis (Eckhardt et al., 2023). The interactions between FA2H and other myelin proteins, crucial for understanding these mechanisms, remain to be fully explored.

5.4 Myelin sheath examination and Ranvier node

The formation of nodes of Ranvier relies on both intrinsic axonal mechanisms and extrinsic influences from glial cells (Berthold CH et al. 1983; Golan et al. 2013; V. Brivio et al. 2017). The *KCNQ2* gene, crucial for encoding Kv7.2 subunits of the M-current—a voltage-gated potassium current that operates below threshold—plays a vital role in moderating neuronal excitability by reducing action potential firing rates (Golan et al. 2013; S. Fisher et al. 2017). *KCNQ2* has been linked to neurodegenerative disorders, and amyloid beta (A β) oligomers, known for their role in Alzheimer’s disease, reduce Kv7.2 expression, thus impacting myelin integrity (Colom et al. 2011; Leao et al. 2012; Duran-Gonzalez et al. 2013). These findings support earlier research that points to axonal architecture disruption in such diseases (I. Coman et al. 2006; Mayordomo-Cava et al. 2015; Bonham et al. 2018). Along the axon, there is notable degradation of myelin and nerve structure, coupled with Kv7.2 accumulations. Earlier studies have reported elongation of nodal regions in multiple sclerosis patients’ tissue samples (I. Coman et al. 2006). Furthermore, Bostock and Sears demonstrated that chemically demyelinated rat spinal roots could maintain excitability, suggesting that internodal axons can continue functioning even when exposed (Bostock and Sears 1987). This might imply that adjusting node lengths could be a strategy to control conduction velocity, potentially leading to uniform node lengths along an axon, whether they are elongated or shortened.

The structure of myelinated axons in FAHN within the CNS and PNS has been extensively studied using two distinct mouse models. The research of S. Jordans and colleagues concentrated on myelination processes, with a particular focus on myelinated axons and Schmidt-Lanterman incisures, or myelin incisures in Schwann cells in the PNS of *FA2H*^{-/-} mice models deficient in sulfatide (S. Jordans et al. 2022). Additionally, the length of internodes, paranodes, and nodes of Ranvier was quantified. The paranodal structure in young *FA2H*^{-/-} mice was found to be normal. Further analysis at 17 months revealed a consistent

paranodal structure, although minor variations in internode length were observed. However, these variations were not statistically significant. It is crucial to highlight that *FA2H*^{-/-} mice exhibit a deficiency in only the 2-hydroxylated forms of these lipids, accompanied by a slight reduction in total sulfatide levels. However, they do not display a complete absence in the PNS (S. Jordans et al. 2021). This indicates that sulfatide can continue to fulfil its functions at the paranodes, regardless of its hydroxylation status in this young mouse model.

Furthermore, another established FA2H KO model was developed by Zöllner and colleagues, which involved generating an *FA2H*^{-/-} mice model with mutations in exons 3, 4, and 5, including 3 and 4 intron of the cytochrome b5 domain, resulting in the complete elimination of FA2H and galactosidase enzyme activity (Zöllner et al. 2008). Despite notable alterations in the fatty acid constitution of GalCer and sulfatide, the distribution of CASPR remained unaltered in *FA2H*^{-/-} mice (6–7 months of age). The length and spacing of CASPR clusters in the sciatic nerves were found to be unaltered by the measurements. Similarly, the clustering of sodium channels in *FA2H*^{-/-} sciatic nerves appeared to be unaltered. This model indicates that the development and maintenance of paranodes in mice up to 6 months of age do not rely on 2-hydroxylated sphingolipids. Unfortunately, due to the late-onset degeneration in aged *FA2H*^{-/-} mice, further analysis in older specimens was not feasible. Consequently, the question of whether structural changes occur at the paranodes in older *FA2H*^{-/-} mice remains unresolved (Zöllner et al. 2008).

A comparison of the research findings on FAHN by S. Jordans and Zöllner reveals that both studies involving *FA2H*^{-/-} mice models did not fully address the condition across all stages of life (Jordans et al. 2022; Zöllner et al. 2008). The Jordans team conducted research on both young and aged mice within the PNS, focusing on various developmental stages. In contrast, the Zöllner group concentrated solely on the myelinated axon structure in younger mice, leaving gaps in their knowledge concerning how impaired myelination in aged mice might affect the structure of Ranvier nodes and internodes.

To address this gap in the literature, we investigated the analysis of myelinated axons in an *in vitro* myelin model derived from iPSCs. The primary focus of this study was on the position of nodes and internodes, the structure of nodes and internodes, and the length, including the number of nodes and internodes. The analysis aimed to determine whether the variability in node lengths occurs predominantly along individual axons or between different axons. To achieve this, fluorescence staining for Kv7.2 was performed, as detailed in Results 4.6.3. The average lengths of Ranvier nodes were reported as CTRL: 3,024 µm and for FAHN: 6,482 µm

(Figure 29). Notably, the number of nodes observed in FAHN was significantly lower than that observed in CTRL (2,162 vs. 1,558 nodes per 100 μm of axon) (Figure 29 and Figure 30). These findings indicate that node lengths not only vary along individual axons but also exhibit significant differences between different axons. This variation suggests that axons may independently adjust their node lengths in order to regulate conduction speed. However, in FAHN, this modulation is impeded by altered internode lengths. Kelly et al. (2001) did not find a direct correlation between the abundance of Kv7.2 channels and node length, suggesting a constant channel density (Kelly et al. 2001). However, they noted that node length could vary independently of channel quantity. This indicates that, despite a constant number of channels at each node, the predicted conduction speed decreases as node length increases (Kelly et al. 2001). This phenomenon is primarily attributable to two factors. Firstly, an increase in node length leads to a decrease in nodal capacitance, which in turn prolongs the charging time for each node, thereby affecting the conduction speed. Secondly, the intracellular axial resistance to current flow from the node into the internode is increased. In the study by Tomassy et al. it was observed that lengthening the node from its average of 2.02 μm to the maximum recorded value of 4.2 μm resulted in a predicted decrease in conduction speed by 6.5% (Tomassy et al. 2014). Conversely, reducing the node length to the minimum observed value of 0.5 μm led to a 3.2% increase in conduction speed, resulting in a speed that was 10.3% faster than at a node length of 4.2 μm . Nevertheless, Chong and colleagues propose that internode lengths may vary considerably and significantly influence current flow (Chong et al. 2012).

When the channel density at each node remains consistent, node length significantly impacts conduction speed in axons with shorter internodes. This leads to conduction speed variations of up to 38% depending on node length (Chong et al. 2012). Additionally, changes in node length affect the correlation between conduction speed and internode length. Initially, as internode length increases, conduction speed rises due to a larger proportion of the axon being myelinated. However, this trend reverses with longer internodes, as the efficiency of depolarization spread between nodes diminishes (Chong et al. 2012). This effect is more pronounced with shorter node lengths, indicating a significant impact of node length adjustments in these cases (Chong et al. 2012).

The results of these studies reveal significant differences compared to control cell lines in an in vitro model, especially regarding the structure of Ranvier nodes, internode length, and node count. The observed demyelination in the FAHN cell model markedly affects axon structure and function. This underscores the need for more extensive studies to explore FAHN's

progressive impact on myelination, particularly in older age groups, to fully understand the disease's trajectory and develop potential interventions.

5.5 Autophagy is affected following loss of FA2H

The autophagy-lysosome pathway plays a pivotal role in the elimination of misfolded proteins and damaged organelles from cells (Joachim B. Kunz et al. 2004; Uttenweiler A. et al. 2007; Tekirdag, K. A. et al. 2017). A crucial step in this pathway is the fusion between autophagosomes and lysosomes. Neurodegenerative diseases, including NBIA, are characterised by the accumulation of misfolded proteins and unrecycled organelles, which leads to a dysfunctional autophagy machinery (Pereira-Dutra et al. 2019; Hinarejos et al. 2020; V. Alessenko et al. 2020, Koga et al. 2010; Faergeman NJ et al. 2004; Wickner W et al. 2010; Rosales K et al. 2011). Nevertheless, the precise involvement of autophagy in FAHN remains unclear. There is growing evidence to suggest a link between FAHN dysfunction and the regulation of the autophagy process. In a seminal paper, C.E. Arber and colleagues investigated the potential interaction between *FA2H* and the regulation of autophagy genes (C. E. Arber et al. 2016). The study focused on ten genes associated with NBIA, a group of neurodegenerative disorders characterised by iron accumulation in the brain. The proposed mechanism revolves around the intramolecular domain of cytochrome b5, which is crucial for FA2H activity, acting as an electron transfer system. The system provides electrons to putative catalytic iron atoms, which are then taken up by ATP13A2, which is involved in the transport of divalent ions into lysosomal compartments. This process may influence iron transport into lysosomal compartments that are rich in iron. Furthermore, the interrelated processes of autophagy and mitophagy are influenced by genes such as *FA2H* and *PLA2G6*, which may affect autophagy through membrane remodeling and vesicle formation (C. E. Arber et al. 2016).

A parallel analysis was conducted by Mandik et al. in 2023, in which two distinct *FA2H*-deficient *Drosophila* models were generated: a compound heterozygous (*dfa2h1/dfa2h2*) and a homozygous (*dfa2h1*) line (Mandik et al. 2023). In particular, studies have implicated FA2H in this fusion process (Mandik et al. 2023). Alterations in mitochondrial fission and fusion were observed in a *FA2H*-deficient *Drosophila* model, resulting in changes in the mitochondrial network. This was accompanied by an increase in the levels of the autophagy marker LC3B and its activation. Moreover, the study indicates that the inhibition of FA2H impairs the fusion of autophagosomes and lysosomes (Mandik et al. 2023; C E Arber et al. 2016). Additionally, fibroblasts derived from FAHN patients exhibiting the same mutations were incorporated into the study. The results of the WB and immunofluorescence analyses of LC3B were found to be

consistent. The compound heterozygous allele demonstrated increased LC3B intensity, whereas no significant difference was observed in the homozygous *dfa2h* alleles. This corroborates the hypotheses put forth by C.E. Arber and H. Hama in 2010, emphasizing the pivotal role of the cytochrome b5 domain in iron ion transfer and the overall expression and activity of the FA2H protein (H. Hama et al. 2010; C. E. Arber et al. 2016). The WB results on the FA2H protein are in accordance with this observation. Consequently, the evolutionary conservation of these results indicates that the loss of *FA2H* is associated with alterations in autophagy across species.

In order to assess the effect of FA2H on the autophagy-lysosome pathway, we examined the expression of the commonly used autophagy markers LC3B and p62. Firstly, the expression of the autophagosomal marker microtubule-associated proteins LC3B was quantified. Under basal conditions, FAHN cell lines exhibited an elevated LC3BII/LC3BI ratio (Figure 31A and B). This is consistent with observations in *FA2H*-deficient cells and other neurodegenerative diseases, indicating impaired autophagic vesicle clearance. However, the difference did not reach statistical significance. Moreover, when the FAHN cell line was subjected to BafA1 treatment for six hours, there were no significant changes in the WB results. This indicates that the synthesis of autophagosomes may have reached its maximum capacity, while the clearance of autophagic vesicles may be impaired. In contrast, the control cell line exhibited a significant increase in LC3BII/LC3BI levels under the same treatment, indicating the inhibition of lysosomal hydrolases, lysosomal dysfunction and the accumulation of autophagosomes.

In our WB study, we also employed the autophagy marker SQSTM1, which is commonly referred to as the ubiquitin-binding protein p62. In the absence of any external stimuli, the FAHN cell line exhibited a pronounced elevation in p62 protein expression in comparison to the CTRL cell line (Figure 32A and B). This finding provides further evidence for a malfunction in cargo targeting and organelle accumulation in FAHN. A parallel study was conducted under BafA1 treatment. It was observed that the p62 expression level remained unchanged in the FAHN cell line, whereas the treatment led to an increase in p62 levels in the CTRL cell line. Given that p62 targets cargo for degradation by autophagy, this result in FAHN suggests an impairment in the cargo targeting process, leading to accumulation and a defective autophagy induction machinery. The reduction in p62 expression following treatment suggests that the initial cargo targeting may have been compromised due to impaired p62 expression. Consequently, the FAHN cell line may have already reached the maximum level of autophagosome accumulation and may have been unable to respond to functional inhibition of lysosomal hydrolases. This is in contrast to findings in other neurodegenerative diseases, such

as Niemann-Pick type C1 (Liedke et al. 2022) and Parkinson's disease (PD) (Menzies et al. 2017), where no differences in p62 levels were detected under basal or treated conditions. This indicates that, in contrast to FAHN, the cargo targeting step is defective in these diseases, yet no accumulation is observed.

6 Summary

Fatty acid 2-hydroxylase (FA2H) is a 43 kDa enzyme that is embedded in the endoplasmic reticulum membrane. This enzyme plays a crucial role in the hydroxylation of fatty acids and their subsequent incorporation into 2-hydroxylated sphingolipids. *FA2H* is present in a number of different tissues, including the brain, spinal cord, skin, testes, ovaries, kidneys, stomach and intestines, in conjunction with 2-OH sphingolipids. In myelin, FA2H plays a role in the synthesis of galactosylceramide and sulfatide, which collectively constitute up to 60% of these molecules. A deficiency of *FA2H* is associated with fatty acid hydroxylase neurodegeneration (FAHN), an autosomal recessive rare disorder that results in the deterioration of the myelin sheath. Despite extensive research into its clinical manifestations, the mechanisms underlying the disease and the biological processes controlling FA2H within its protein environment remain unclear. The initial phase of the research project involved the generation and analysis of *FA2H*-deficient induced pluripotent stem cell (iPSC) lines. These were subsequently employed to generate neuronal, glial and, in particular, oligodendroglial cells for pathophysiological analysis, with a specific focus on myelination processes. The FAHN iPSC line was found to be stable and to exhibit normal growth patterns, with no evidence of morphological abnormalities during culturing processes.

The differentiation process of FAHN cells into neuronal differentiated cells (NDC) and oligodendrocyte precursor cells (OPCs) was found to be unaltered. Furthermore, the differentiation process of NDCs and OPCs in a coculture did not exhibit any alterations. The morphology, growth, and differentiation of FAHN cells into neural lineage cells were observed to be normal. Nevertheless, it was observed that the expression of FA2H was affected and reduced in NDC and OPCs in FAHN. This was observed in Western blot and immunofluorescence staining, thereby demonstrating the impact of the mutation.

The expression of myelin proteins MBP and PLP was found to be reduced. This was observed in both cell types, namely OPCs, and in coculture, respectively. Moreover, the colocalisation of PLP-MBP in OPC and coculture was diminished, which is analogous to the other findings in *FA2H*-deficient mice models. This suggests that the myelin membrane scaffold is affected, which in turn results in an unstable myelin sheath and demyelination. It is noteworthy that impairment of the Ranvier nodes and an increase in the length of the internodes were observed. The number and size of nodes were analysed, and it was found that there are fewer nodes per 100 μm axons in FAHN.

The latter part of the study was dedicated to the analysis of the autophagy process in FAHN, with the objective of examining the expression and subcellular localisation of key autophagic proteins, p62 and LC3B, through Western blot. These analyses were conducted under both standard culture conditions and conditions simulating nutrient deprivation or inhibition of autophagosome degradation with Bafilomycin A1 (BafA1). The findings indicated a disruption in autolysosome accumulation and autophagic processes, which aligns with patterns observed in other neurodegenerative diseases.

The findings of this research have significant implications for the understanding of FAHN disease. The establishment of the FAHN iPSC line will facilitate a deeper understanding of FAHN, providing crucial insights that will inform future research. This opens up new avenues for further investigation and brings us closer to pharmacological developments and potential treatment options for patients with FAHN.

7 Outlook

The findings of this research have significant implications for understanding FAHN disease. The establishment of the FAHN iPSC line will facilitate a deeper comprehension of FAHN, providing crucial insights that will inform future research. This development opens up new avenues for further investigation and brings us closer to pharmacological advancements and potential treatment options for patients with FAHN.

Key areas for future research include:

- **Defect in Transport:** This study observed an imbalance between node and internode length. Future investigations into ion homeostasis and energy flow content in FAHN can elucidate defects in transport, presumably influenced by an altered cytoskeleton.
- **Autophagy Process:** Future research should focus on the autophagy process, specifically the roles of *FA2H* and ceramide in OPC cells in autophagy and mitophagy. Such studies could provide valuable insights into how sphingolipids influence different stages of autophagy, enhancing our understanding of cellular regulatory mechanisms.
- **Remyelination:** The process of myelin instability and the imbalanced formation of the myelin membrane scaffold in FAHN was observed in this study. Future studies should extend coculture experiments of OLs and neurons to understand the potential processes of remyelination in regenerated axons.
- **Pharmaceutical Chaperones:** iPSCs, being stable cells, offer the possibility for treatment with different molecules. This could lead to the identification of suitable pharmaceutical chaperones and the development of drug screening protocols for clinical treatment for FAHN patients.

These avenues of research will contribute significantly to the understanding and treatment of FAHN, potentially leading to groundbreaking discoveries in the field.

8 References

- Aggarwal, S., Yurlova, L., & Simons, M. (2011). Central nervous system myelin: Structure, synthesis and assembly. *Trends in Cell Biology*, 21(10), 585–593. <https://doi.org/10.1016/j.tcb.2011.06.004>
- Alderson, N. L., & Hama, H. (2009). Fatty acid 2-hydroxylase regulates cAMP-induced cell cycle exit in D6P2T schwannoma cells. *Journal of Lipid Research*, 50(6), 1203–1208. <https://doi.org/10.1194/jlr.M800666-JLR200>
- Alderson, N. L., Maldonado, E. N., Kern, M. J., Bhat, N. R., & Hama, H. (2006). Fa2h-dependent fatty acid 2-hydroxylation in postnatal mouse brain. *Journal of Lipid Research*, 47(12), 2772–2780. <https://doi.org/10.1194/jlr.M600362-JLR200>
- Alderson, N. L., Rembiesa, B. M., Walla, M. D., Bielawska, A., Bielawski, J., & Hama, H. (2004). The human FA2H gene encodes a fatty acid 2-hydroxylase. *The Journal of Biological Chemistry*, 279(47), 48562–48568. <https://doi.org/10.1074/jbc.M406649200>
- Alderson, N. L., Walla, M. D., & Hama, H. (2005). A novel method for the measurement of in vitro fatty acid 2-hydroxylase activity by gas chromatography-mass spectrometry. *Journal of Lipid Research*, 46(7), 1569–1575. <https://doi.org/10.1194/jlr.D500013-JLR200>
- Alessenko, A. V., & Albi, E. (2020). Exploring Sphingolipid Implications in Neurodegeneration. *Frontiers in Neurology*, 11, 437. <https://doi.org/10.3389/fneur.2020.00437>
- Alexaki, A., Gupta, S. D., Majumder, S., Kono, M., Tuymetova, G., Harmon, J. M., . . . Proia, R. L. (2014). Autophagy regulates sphingolipid levels in the liver. *Journal of Lipid Research*, 55(12), 2521–2531. <https://doi.org/10.1194/jlr.M051862>
- Arancibia-Carcamo, I. L., & Attwell, D. (2014). The node of Ranvier in CNS pathology. *Acta Neuropathologica*, 128(2), 161–175. <https://doi.org/10.1007/s00401-014-1305-z>
- Arber, C., Angelova, P. R., Wiethoff, S., Tsuchiya, Y., Mazzacuva, F., Preza, E., . . . Wray, S. [Selina] (2017). İpsc-derived neuronal models of PANK2-associated neurodegeneration reveal mitochondrial dysfunction contributing to early disease. *PloS One*, 12(9), e0184104. <https://doi.org/10.1371/journal.pone.0184104>
- Arber, C. E., Li, A., Houlden, H. [H.], & Wray, S. [S.] (2016). Review: Insights into molecular mechanisms of disease in neurodegeneration with brain iron accumulation: unifying theories. *Neuropathology and Applied Neurobiology*, 42(3), 220–241. <https://doi.org/10.1111/nan.12242>
- Backer, J. M. (2008). The regulation and function of Class III PI3Ks: Novel roles for Vps34. *The Biochemical Journal*, 410(1), 1–17. <https://doi.org/10.1042/BJ20071427>
- Bansal, R., Warrington, A. E., Gard, A. L., Ranscht, B., & Pfeiffer, S. E. (1989). Multiple and novel specificities of monoclonal antibodies O1, O4, and R-mAb used in the analysis of oligodendrocyte development. *Journal of Neuroscience Research*, 24(4), 548–557. <https://doi.org/10.1002/jnr.490240413>
- Baron, W., & Hoekstra, D. (2010). On the biogenesis of myelin membranes: Sorting, trafficking and cell polarity. *FEBS Letters*, 584(9), 1760–1770. <https://doi.org/10.1016/j.febslet.2009.10.085>
- Baron, W., Vries, E. J. de, Vries, H. de, & Hoekstra, D. (1999). Protein kinase C prevents oligodendrocyte differentiation: modulation of actin cytoskeleton and cognate polarized membrane traffic. *Journal of Neurobiology*, 41(3), 385–398. [https://doi.org/10.1002/\(SICI\)1097-4695\(19991115\)41:3<385::AID-NEU7>3.0.CO;2-E](https://doi.org/10.1002/(SICI)1097-4695(19991115)41:3<385::AID-NEU7>3.0.CO;2-E)
- Bechler, M. E., Byrne, L., & Ffrench-Constant, C. (2015). Cns Myelin Sheath Lengths Are an Intrinsic Property of Oligodendrocytes. *Current Biology : CB*, 25(18), 2411–2416. <https://doi.org/10.1016/j.cub.2015.07.056>

- Benamer, N., Vidal, M., Balia, M., & Angulo, M. C. (2020). Myelination of parvalbumin interneurons shapes the function of cortical sensory inhibitory circuits. *Nature Communications*, *11*(1), 5151. <https://doi.org/10.1038/s41467-020-18984-7>
- Bizzozero, O. A., Malkoski, S. P., Mobarak, C., Bixler, H. A., & Evans, J. E. (2002). Mass-spectrometric analysis of myelin proteolipids reveals new features of this family of palmitoylated membrane proteins. *Journal of Neurochemistry*, *81*(3), 636–645. <https://doi.org/10.1046/j.1471-4159.2002.00852.x>
- Boggs, J. M. (2006). Myelin basic protein: A multifunctional protein. *Cellular and Molecular Life Sciences : CMLS*, *63*(17), 1945–1961. <https://doi.org/10.1007/s00018-006-6094-7>
- Boiko, T., & Winckler, B. (2006). Myelin under construction -- teamwork required. *The Journal of Cell Biology*, *172*(6), 799–801. <https://doi.org/10.1083/jcb.200602101>
- Bonham, L. W., Evans, D. S., Liu, Y., Cummings, S. R., Yaffe, K., & Yokoyama, J. S. (2018). Neurotransmitter Pathway Genes in Cognitive Decline During Aging: Evidence for GNG4 and KCNQ2 Genes. *American Journal of Alzheimer's Disease and Other Dementias*, *33*(3), 153–165. <https://doi.org/10.1177/1533317517739384>
- Brinkmann, B. G., Agarwal, A., Sereda, M. W., Garratt, A. N., Müller, T., Wende, H., . . . Nave, K. A. [Klaus Armin] (2008). Neuregulin-1/ErbB signaling serves distinct functions in myelination of the peripheral and central nervous system. *Neuron*, *59*(4), 581–595. <https://doi.org/10.1016/j.neuron.2008.06.028>
- Brivio, V., Faivre-Sarrailh, C., Peles, E. [Elior], Sherman, D. L., & Brophy, P. J. (2017). Assembly of CNS Nodes of Ranvier in Myelinated Nerves Is Promoted by the Axon Cytoskeleton. *Current Biology : CB*, *27*(7), 1068–1073. <https://doi.org/10.1016/j.cub.2017.01.025>
- BRUCE A. BARUT and LEONARD I. ZON. Realizing the potential of zebrafish as a model for human disease.
- Cao, L., Huang, X.-J., Chen, C.-J., & Chen, S.-D. (2013). A rare family with Hereditary Spastic Paraplegia Type 35 due to novel FA2H mutations: A case report with literature review. *Journal of the Neurological Sciences*, *329*(1-2), 1–5. <https://doi.org/10.1016/j.jns.2013.02.026>
- Chanoumidou, K., Mozafari, S., Baron-Van Evercooren, A., & Kuhlmann, T. (2020). Stem cell derived oligodendrocytes to study myelin diseases. *Glia*, *68*(4), 705–720. <https://doi.org/10.1002/glia.23733>
- Chong, S. Y. C., Rosenberg, S. S., Fancy, S. P. J., Zhao, C., Shen, Y.-A. A., Hahn, A. T., . . . Chan, J. R. (2012). Neurite outgrowth inhibitor Nogo-A establishes spatial segregation and extent of oligodendrocyte myelination. *Proceedings of the National Academy of Sciences of the United States of America*, *109*(4), 1299–1304. <https://doi.org/10.1073/pnas.1113540109>
- Clague, M. J., & Hammond, D. E. (2006). Membrane traffic: Catching the lysosome express. *Current Biology : CB*, *16*(11), R416-8. <https://doi.org/10.1016/j.cub.2006.05.009>
- Cognato, H., Galvin, J., Wang, Z., Relucio, J., Nguyen, T., Harrison, D., . . . French-Constant, C. (2007). Identification of dystroglycan as a second laminin receptor in oligodendrocytes, with a role in myelination. *Development (Cambridge, England)*, *134*(9), 1723–1736. <https://doi.org/10.1242/dev.02819>
- Coman, I., Aigrot, M. S., Seilhean, D., Reynolds, R., Girault, J. A., Zalc, B., & Lubetzki, C. [C.] (2006). Nodal, paranodal and juxtapanodal axonal proteins during demyelination and remyelination in multiple sclerosis. *Brain : A Journal of Neurology*, *129*(Pt 12), 3186–3195. <https://doi.org/10.1093/brain/awl144>
- Dan, P., Edvardson, S., Bielawski, J., Hama, H., & Saada, A. (2011). 2-Hydroxylated sphingomyelin profiles in cells from patients with mutated fatty acid 2-hydroxylase. *Lipids in Health and Disease*, *10*, 84. <https://doi.org/10.1186/1476-511X-10-84>

- Dick, K. J., Eckhardt, M., Paisán-Ruiz, C., Alshehhi, A. A., Proukakis, C., Sibtain, N. A., . . . Crosby, A. H. (2010). Mutation of FA2H underlies a complicated form of hereditary spastic paraplegia (SPG35). *Human Mutation*, *31*(4), E1251-60. <https://doi.org/10.1002/humu.21205>
- Dimos, J. T., Rodolfa, K. T., Niakan, K. K., Weisenthal, L. M., Mitsumoto, H., Chung, W., . . . Eggan, K. (2008). Induced pluripotent stem cells generated from patients with ALS can be differentiated into motor neurons. *Science (New York, N.Y.)*, *321*(5893), 1218–1221. <https://doi.org/10.1126/science.1158799>
- Dingjan, T., & Futerman, A. H. (2021). The role of the 'sphingoid motif' in shaping the molecular interactions of sphingolipids in biomembranes. *Biochimica Et Biophysica Acta. Biomembranes*, *1863*(11), 183701. <https://doi.org/10.1016/j.bbamem.2021.183701>
- Fitzner D, Schneider A, Kippert A, Möbius W, Willig KI, Hell SW, Bunt G, Gaus K, Simons M. Myelin basic protein-dependent plasma membrane reorganization in the formation of myelin. *EMBO J*. 2006 Nov 1;25(21):5037-48. doi: 10.1038/sj.emboj.7601376. Epub 2006 Oct 12. PMID: 17036049; PMCID: PMC1630406.
- Dirkx, N., Miceli, F., Tagliatalata, M., & Weckhuysen, S. (2020). The Role of Kv7.2 in Neurodevelopment: Insights and Gaps in Our Understanding. *Frontiers in Physiology*, *11*, 570588. <https://doi.org/10.3389/fphys.2020.570588>
- Donkervoort, S., Dastgir, J., Hu, Y., Zein, W. M., Marks, H., Blackstone, C., & Bönnemann, C. G. (2014). Phenotypic variability of a likely FA2H founder mutation in a family with complicated hereditary spastic paraplegia. *Clinical Genetics*, *85*(4), 393–395. <https://doi.org/10.1111/cge.12185>
- Douvaras, P., Wang, J., Zimmer, M., Hanchuk, S., O'Bara, M. A., Sadiq, S., . . . Fossati, V. (2014). Efficient generation of myelinating oligodendrocytes from primary progressive multiple sclerosis patients by induced pluripotent stem cells. *Stem Cell Reports*, *3*(2), 250–259. <https://doi.org/10.1016/j.stemcr.2014.06.012>
- Durán-González, J., Michi, E. D., Elorza, B., Perez-Córdova, M. G., Pacheco-Otalora, L. F., Touhami, A., . . . Colom, L. V. (2013). Amyloid β peptides modify the expression of antioxidant repair enzymes and a potassium channel in the septohippocampal system. *Neurobiology of Aging*, *34*(8), 2071–2076. <https://doi.org/10.1016/j.neurobiolaging.2013.02.005>
- Ebert, A. D., Liang, P., & Wu, J. C. (2012). Induced pluripotent stem cells as a disease modeling and drug screening platform. *Journal of Cardiovascular Pharmacology*, *60*(4), 408–416. <https://doi.org/10.1097/FJC.0b013e318247f642>
- Eckhardt, M. (2023). Fatty Acid 2-Hydroxylase and 2-Hydroxylated Sphingolipids: Metabolism and Function in Health and Diseases. *International Journal of Molecular Sciences*, *24*(5). <https://doi.org/10.3390/ijms24054908>
- Edvardson, S., Hama, H., Shaag, A., Gomori, J. M., Berger, I., Soffer, D., . . . Elpeleg, O. (2008). Mutations in the fatty acid 2-hydroxylase gene are associated with leukodystrophy with spastic paraparesis and dystonia. *American Journal of Human Genetics*, *83*(5), 643–648. <https://doi.org/10.1016/j.ajhg.2008.10.010>
- Efendic, f., Krohn, S., Murua Escobar, H., Venkateswaran, S., Bennett, S. A. L., Hermann, A., & Frech, M. J. (2023). Generation of the human iPSC lines AKOSi011-A carrying the mutation p.Pro65ser/p.Asp35t and AKOSi012-A, carrying the mutation p.Tyr231his, derived from FAHN patient fibroblasts. *Stem Cell Research*, *71*, 103178. <https://doi.org/10.1016/j.scr.2023.103178>
- Efendic, f., Völkner, C., Krohn, S., Murua Escobar, H., Venkateswaran, S., Bennett, S., . . . Frech, M. J. (2022). Generation of the human iPSC line AKOSi010-A from fibroblasts of a female FAHN patient, carrying the compound heterozygous mutation p.Gly45arg/p.His319arg. *Stem Cell Research*, *63*, 102863. <https://doi.org/10.1016/j.scr.2022.102863>
- Ehrlich, M., Mozafari, S., Glatza, M., Starost, L., Velychko, S., Hallmann, A.-L., . . . Kuhlmann, T. (2017). Rapid and efficient generation of oligodendrocytes from human induced pluripotent stem

- cells using transcription factors. *Proceedings of the National Academy of Sciences of the United States of America*, 114(11), E2243–E2252. <https://doi.org/10.1073/pnas.1614412114>
- Ettle, B., Schlachetzki, J. C. M., & Winkler, J. (2016). Oligodendroglia and Myelin in Neurodegenerative Diseases: More Than Just Bystanders? *Molecular Neurobiology*, 53(5), 3046–3062. <https://doi.org/10.1007/s12035-015-9205-3>
- Fasano, A., Amoresano, A., Rossano, R., Carlone, G., Carpentieri, A., Liuzzi, G. M., . . . Riccio, P. (2008). The different forms of PNS myelin P0 protein within and outside lipid rafts. *Journal of Neurochemistry*, 107(1), 291–301. <https://doi.org/10.1111/j.1471-4159.2008.05598.x>
- Feldmann, A., Winterstein, C., White, R., Trotter, J., & Krämer-Albers, E.-M. (2009). Comprehensive analysis of expression, subcellular localization, and cognate pairing of SNARE proteins in oligodendrocytes. *Journal of Neuroscience Research*, 87(8), 1760–1772. <https://doi.org/10.1002/jnr.22020>
- Feltri, M. L., Weinstock, N. I., Favret, J., Dhimal, N., Wrabetz, L., & Shin, D. (2021). Mechanisms of demyelination and neurodegeneration in globoid cell leukodystrophy. *Glia*, 69(10), 2309–2331. <https://doi.org/10.1002/glia.24008>
- Fisher, R. S., Cross, J. H., D'Souza, C., French, J. A., Haut, S. R., Higurashi, N., . . . Zuberi, S. M. (2017). Instruction manual for the ILAE 2017 operational classification of seizure types. *Epilepsia*, 58(4), 531–542. <https://doi.org/10.1111/epi.13671>
- Fraichard, A., Chassande, O., Bilbaut, G., Dehay, C., Savatier, P., & Samarut, J. (1995). In vitro differentiation of embryonic stem cells into glial cells and functional neurons. *Journal of Cell Science*, 108 (Pt 10), 3181–3188. <https://doi.org/10.1242/jcs.108.10.3181>
- Friedman, A. K., Walsh, J. J., Juarez, B., Ku, S. M., Chaudhury, D., Wang, J., . . . Han, M.-H. (2014). Enhancing depression mechanisms in midbrain dopamine neurons achieves homeostatic resilience. *Science (New York, N.Y.)*, 344(6181), 313–319. <https://doi.org/10.1126/science.1249240>
- Fujita N, Itoh T, Omori H, Fukuda M, Noda T, Yoshimori T. The Atg16L complex specifies the site of LC3 lipidation for membrane biogenesis in autophagy. *Mol Biol Cell*. 2008 May;19(5):2092-100. doi: 10.1091/mbc.e07-12-1257. Epub 2008 Mar 5. PMID: 18321988; PMCID: PMC2366860.
- Gaesser, J. M., & Fyffe-Maricich, S. L. (2016). Intracellular signaling pathway regulation of myelination and remyelination in the CNS. *Experimental Neurology*, 283(Pt B), 501–511. <https://doi.org/10.1016/j.expneurol.2016.03.008>
- García-León, J. A., García-Díaz, B., Eggermont, K., Cáceres-Palomo, L., Neyrinck, K., Da Madeiro Costa, R., . . . Verfaillie, C. M. (2020). Generation of oligodendrocytes and establishment of an all-human myelinating platform from human pluripotent stem cells. *Nature Protocols*, 15(11), 3716–3744. <https://doi.org/10.1038/s41596-020-0395-4>
- Garone, C., Pippucci, T., Cordelli, D. M., Zuntini, R., Castegnaro, G., Marconi, C., . . . Franzoni, E. (2011). Fa2h-related disorders: A novel c.270+3at splice-site mutation leads to a complex neurodegenerative phenotype. *Developmental Medicine and Child Neurology*, 53(10), 958–961. <https://doi.org/10.1111/j.1469-8749.2011.03993.x>
- German, A., Jukic, J., Laner, A., Arnold, P., Socher, E., Mennecke, A., . . . Regensburger, M. (2023). Novel Homozygous FA2H Variant Causing the Full Spectrum of Fatty Acid Hydroxylase-Associated Neurodegeneration (SPG35). *Genes*, 15(1). <https://doi.org/10.3390/genes15010014>
- Glick, D., Barth, S., & Macleod, K. F. (2010). Autophagy: Cellular and molecular mechanisms. *The Journal of Pathology*, 221(1), 3–12. <https://doi.org/10.1002/path.2697>
- Golan, N., Kartvelishvily, E., Spiegel, I., Salomon, D., Sabanay, H., Rechav, K., . . . Peles, E. [E.] (2013). Genetic Deletion of Cadm4 Results in Myelin Abnormalities Resembling Charcot-Marie-Tooth Neuropathy. *Journal of Neuroscience*, 33(27), 10950–10961. <https://doi.org/10.1523/JNEUROSCI.0571-13.2013>

- Goldman, S. A., & Kuypers, N. J. (2015). How to make an oligodendrocyte. *Development (Cambridge, England)*, 142(23), 3983–3995. <https://doi.org/10.1242/dev.126409>
- Gow, A., Friedrich, V. L., & Lazzarini, R. A. (1994). Many naturally occurring mutations of myelin proteolipid protein impair its intracellular transport. *Journal of Neuroscience Research*, 37(5), 574–583. <https://doi.org/10.1002/jnr.490370504>
- Guo, F., Liu, X., Cai, H., & Le, W. (2018). Autophagy in neurodegenerative diseases: Pathogenesis and therapy. *Brain Pathology (Zurich, Switzerland)*, 28(1), 3–13. <https://doi.org/10.1111/bpa.12545>
- Guo, L., Zhang, X., Zhou, D., Okunade, A. L., & Su, X. (2012). Stereospecificity of fatty acid 2-hydroxylase and differential functions of 2-hydroxy fatty acid enantiomers. *Journal of Lipid Research*, 53(7), 1327–1335. <https://doi.org/10.1194/jlr.M025742>
- Hama, H. (2010). Fatty acid 2-Hydroxylation in mammalian sphingolipid biology. *Biochimica Et Biophysica Acta*, 1801(4), 405–414. <https://doi.org/10.1016/j.bbalip.2009.12.004>
- Hamilton, N. B., Clarke, L. E., Arancibia-Carcamo, I. L., Kougioumtzidou, E., Matthey, M., Káradóttir, R., . . . Attwell, D. (2017). Endogenous GABA controls oligodendrocyte lineage cell number, myelination, and CNS internode length. *Glia*, 65(2), 309–321. <https://doi.org/10.1002/glia.23093>
- Handbook of Laboratory Animal Science, Volume I.
- Hashemi, N., Abadi, R. N. S., Alavi, A., Rohani, M., Ghasemi, A., & Tavasoli, A. R. (2023). The first reports of FA2H-associated neurodegeneration from two unrelated Iranian families. *Neurological Sciences : Official Journal of the Italian Neurological Society and of the Italian Society of Clinical Neurophysiology*, 44(12), 4359–4362. <https://doi.org/10.1007/s10072-023-06932-4>
- Hinarejos, I., Machuca-Arellano, C., Sancho, P., & Espinós, C. (2020). Mitochondrial Dysfunction, Oxidative Stress and Neuroinflammation in Neurodegeneration with Brain Iron Accumulation (NBIA). *Antioxidants (Basel, Switzerland)*, 9(10). <https://doi.org/10.3390/antiox9101020>
- Ho Bum Kang, Jin Sook Kim, Hyung-Joo Kwon, Ki Hoan Nam, Hyun Soo Youn, Dai-Eun Sok, & Dr. Younghee Lee. Basic Fibroblast Growth Factor Activates ERK and Induces c-Fos in Human Embryonic Stem Cell Line MizhES1.
- Jaber, N., & Zong, W.-X. (2013). Class III PI3K Vps34: Essential roles in autophagy, endocytosis, and heart and liver function. *Annals of the New York Academy of Sciences*, 1280, 48–51. <https://doi.org/10.1111/nyas.12026>
- Jäkel, S., Agirre, E., Mendanha Falcão, A., van Bruggen, D., Lee, K. W., Knuesel, I., . . . Castelo-Branco, G. (2019). Altered human oligodendrocyte heterogeneity in multiple sclerosis. *Nature*, 566(7745), 543–547. <https://doi.org/10.1038/s41586-019-0903-2>
- John Shanklin and Edgar B. Cahoon. DESATURATION AND RELATED MODIFICATIONS OF FATTY ACIDS.
- Jordans, S., Hardt, R., Becker, I., Winter, D., Wang-Eckhardt, L., & Eckhardt, M. (2022). Age-Dependent Increase in Schmidt-Lanterman Incisures and a Cadm4-Associated Membrane Skeletal Complex in Fatty Acid 2-hydroxylase Deficient Mice: A Mouse Model of Spastic Paraplegia SPG35. *Molecular Neurobiology*, 59(7), 3969–3979. <https://doi.org/10.1007/s12035-022-02832-4>
- K⁺ channel distribution and clustering in developing and hypomyelinated axons of the optic nerve.
- Kabaya Y, Mizushima N, Ueno T, Yamamoto A, Kirisako T, Noda T, Kominami E, Ohsumi Y, Yoshimori T. LC3, a mammalian homologue of yeast Apg8p, is localized in autophagosome membranes after processing. *EMBO J*. 2000 Nov 1;19(21):5720-8. doi: 10.1093/emboj/19.21.5720. Erratum in: *EMBO J*. 2003 Sep 1;22(17):4577. PMID: 11060023; PMCID: PMC305793.
- Kelly, M. K., Carvell, G. E., Hartings, J. A., & Simons, D. J. (2001). Axonal conduction properties of antidromically identified neurons in rat barrel cortex. *Somatosensory & Motor Research*, 18(3), 202–210. <https://doi.org/10.1080/01421590120072196>

- Kocaturk, N. M., & Gozuacik, D. (2018). Crosstalk Between Mammalian Autophagy and the Ubiquitin-Proteasome System. *Frontiers in Cell and Developmental Biology*, 6, 128. <https://doi.org/10.3389/fcell.2018.00128>
- Koga, H., Kaushik, S., & Cuervo, A. M. (2010). Altered lipid content inhibits autophagic vesicular fusion. *The FASEB Journal*, 24(8), 3052–3065. <https://doi.org/10.1096/fj.09-144519>
- Kohlschütter, A., & Eichler, F. (2011). Childhood leukodystrophies: A clinical perspective. *Expert Review of Neurotherapeutics*, 11(10), 1485–1496. <https://doi.org/10.1586/ern.11.135>
- Kota, V., Dhople, V. M., Fullbright, G., Smythe, N. M., Szulc, Z. M., Bielawska, A., & Hama, H. (2013). 2'-hydroxy C16-ceramide induces apoptosis-associated proteomic changes in C6 glioma cells. *Journal of Proteome Research*, 12(10), 4366–4375. <https://doi.org/10.1021/pr4003432>
- Kota, V., & Hama, H. (2014). 2'-Hydroxy ceramide in membrane homeostasis and cell signaling. *Advances in Biological Regulation*, 54, 223–230. <https://doi.org/10.1016/j.jbior.2013.09.012>
- Krämer, E. M., Schardt, A., & Nave, K. A. [K. A.] (2001). Membrane traffic in myelinating oligodendrocytes. *Microscopy Research and Technique*, 52(6), 656–671. <https://doi.org/10.1002/jemt.1050>
- Kroepfl, J. F., & Gardinier, M. V. (2001). Mutually exclusive apicobasolateral sorting of two oligodendroglial membrane proteins, proteolipid protein and myelin/oligodendrocyte glycoprotein, in Madin-Darby canine kidney cells. *Journal of Neuroscience Research*, 66(6), 1140–1148. <https://doi.org/10.1002/jnr.10035>
- Kruer, M. C., Paisán-Ruiz, C., Boddaert, N., Yoon, M. Y., Hama, H., Gregory, A., . . . Hayflick, S. J. (2010). Defective FA2H leads to a novel form of neurodegeneration with brain iron accumulation (NBIA). *Annals of Neurology*, 68(5), 611–618. <https://doi.org/10.1002/ana.22122>
- Kuhn, S., Gritti, L., Crooks, D., & Dombrowski, Y. (2019). Oligodendrocytes in Development, Myelin Generation and Beyond. *Cells*, 8(11). <https://doi.org/10.3390/cells8111424>
- Kumar, V., Sami, N., Kashav, T., Islam, A., Ahmad, F., & Hassan, M. I. (2016). Protein aggregation and neurodegenerative diseases: From theory to therapy. *European Journal of Medicinal Chemistry*, 124, 1105–1120. <https://doi.org/10.1016/j.ejmech.2016.07.054>
- Kunz, J. B., Schwarz, H., & Mayer, A. (2004). Determination of four sequential stages during microautophagy in vitro. *The Journal of Biological Chemistry*, 279(11), 9987–9996. <https://doi.org/10.1074/jbc.M307905200>
- Kyogashima, M., Tadano-Aritomi, K., Aoyama, T., Yusa, A., Goto, Y., Tamiya-Koizumi, K., . . . Hara, A. (2008). Chemical and apoptotic properties of hydroxy-ceramides containing long-chain bases with unusual alkyl chain lengths. *Journal of Biochemistry*, 144(1), 95–106. <https://doi.org/10.1093/jb/mvn050>
- Laukka, J. J., Kamholz, J., Bessert, D., & Skoff, R. P. (2016). Novel pathologic findings in patients with Pelizaeus-Merzbacher disease. *Neuroscience Letters*, 627, 222–232. <https://doi.org/10.1016/j.neulet.2016.05.028>
- Leão, R. N., Colom, L. V., Borgius, L., Kiehn, O., & Fisahn, A. (2012). Medial septal dysfunction by Aβ-induced KCNQ channel-block in glutamatergic neurons. *Neurobiology of Aging*, 33(9), 2046–2061. <https://doi.org/10.1016/j.neurobiolaging.2011.07.013>
- Lee, G., & Leugers, C. J. (2012). Tau and Tauopathies. In *Progress in Molecular Biology and Translational Science. Molecular Biology of Neurodegenerative Diseases* (Vol. 107, pp. 263–293). Elsevier. <https://doi.org/10.1016/B978-0-12-385883-2.00004-7>
- Leong, S. Y., Rao, V. T. S., Bin, J. M., Gris, P., Sangaralingam, M., Kennedy, T. E., & Antel, J. P. (2014). Heterogeneity of oligodendrocyte progenitor cells in adult human brain. *Annals of Clinical and Translational Neurology*, 1(4), 272–283. <https://doi.org/10.1002/acn3.55>

- Liedtke, M., Völkner, C., Hermann, A., & Frech, M. J. (2022). Impact of Organelle Transport Deficits on Mitophagy and Autophagy in Niemann-Pick Disease Type C. *Cells*, *11*(3). <https://doi.org/10.3390/cells11030507>
- Livesey, M. R., Magnani, D., Cleary, E. M., Vasistha, N. A., James, O. T., Selvaraj, B. T., . . . Chandran, S. (2016). Maturation and electrophysiological properties of human pluripotent stem cell-derived oligodendrocytes. *Stem Cells (Dayton, Ohio)*, *34*(4), 1040–1053. <https://doi.org/10.1002/stem.2273>
- Lubetzki, C. [Catherine], Sol-Foulon, N., & Desmazières, A. (2020). Nodes of Ranvier during development and repair in the CNS. *Nature Reviews. Neurology*, *16*(8), 426–439. <https://doi.org/10.1038/s41582-020-0375-x>
- Madhavan, M., Nevin, Z. S., Shick, H. E., Garrison, E., Clarkson-Paredes, C., Karl, M., . . . Tesar, P. J. (2018). Induction of myelinating oligodendrocytes in human cortical spheroids. *Nature Methods*, *15*(9), 700–706. <https://doi.org/10.1038/s41592-018-0081-4>
- Maier, H., Meixner, M., Hartmann, D., Sandhoff, R., Wang-Eckhardt, L., Zöllner, I., . . . Eckhardt, M. (2011). Normal fur development and sebum production depends on fatty acid 2-hydroxylase expression in sebaceous glands. *The Journal of Biological Chemistry*, *286*(29), 25922–25934. <https://doi.org/10.1074/jbc.M111.231977>
- Maldonado, E. N., Alderson, N. L., Monje, P. V., Wood, P. M., & Hama, H. (2008). Fa2h is responsible for the formation of 2-hydroxy galactolipids in peripheral nervous system myelin. *Journal of Lipid Research*, *49*(1), 153–161. <https://doi.org/10.1194/jlr.M700400-JLR200>
- Mandik, F., Kanana, Y., Rody, J., Misera, S., Wilken, B., Laabs von Holt, B.-H., . . . Vos, M. (2022). A new model for fatty acid hydroxylase-associated neurodegeneration reveals mitochondrial and autophagy abnormalities. *Frontiers in Cell and Developmental Biology*, *10*, 1000553. <https://doi.org/10.3389/fcell.2022.1000553>
- Marcus, J., Honigbaum, S., Shroff, S., Honke, K., Rosenbluth, J., & Dupree, J. L. (2006). Sulfatide is essential for the maintenance of CNS myelin and axon structure. *Glia*, *53*(4), 372–381. <https://doi.org/10.1002/glia.20292>
- Meixner, M., Jungnickel, J., Grothe, C. et al. Myelination in the absence of UDP-galactose:ceramide galactosyl-transferase and fatty acid 2 -hydroxylase. *BMC Neurosci* *12*, 22 (2011). <https://doi.org/10.1186/1471-2202-12-22>
- Mayordomo-Cava, J., Yajeya, J., Navarro-López, J. D., & Jiménez-Díaz, L. (2015). Amyloid-β(25-35) Modulates the Expression of GirK and KCNQ Channel Genes in the Hippocampus. *PLoS One*, *10*(7), e0134385. <https://doi.org/10.1371/journal.pone.0134385>
- Mayshar, Y., Ben-David, U., Lavon, N., Biancotti, J.-C., Yakir, B., Clark, A. T., . . . Benvenisty, N. (2010). Identification and classification of chromosomal aberrations in human induced pluripotent stem cells. *Cell Stem Cell*, *7*(4), 521–531. <https://doi.org/10.1016/j.stem.2010.07.017>
- McPhie, D. L., Nehme, R., Ravichandran, C., Babb, S. M., Ghosh, S. D., Staskus, A., . . . Cohen, B. M. (2018). Oligodendrocyte differentiation of induced pluripotent stem cells derived from subjects with schizophrenias implicate abnormalities in development. *Translational Psychiatry*, *8*(1), 230. <https://doi.org/10.1038/s41398-018-0284-6>
- Meireles, A. M., Shen, K., Zoupi, L., Iyer, H., Bouchard, E. L., Williams, A., & Talbot, W. S. (2018). The Lysosomal Transcription Factor TFEB Represses Myelination Downstream of the Rag-Ragulator Complex. *Developmental Cell*, *47*(3), 319–330.e5. <https://doi.org/10.1016/j.devcel.2018.10.003>
- Menzies, F. M., Fleming, A., Caricasole, A., Bento, C. F., Andrews, S. P., Ashkenazi, A., . . . Rubinsztein, D. C. (2017). Autophagy and Neurodegeneration: Pathogenic Mechanisms and Therapeutic Opportunities. *Neuron*, *93*(5), 1015–1034. <https://doi.org/10.1016/j.neuron.2017.01.022>

- Merkle, F. T., & Eggan, K. (2013). Modeling human disease with pluripotent stem cells: From genome association to function. *Cell Stem Cell*, 12(6), 656–668. <https://doi.org/10.1016/j.stem.2013.05.016>
- Mizutani, Y., Kihara, A., Chiba, H., Tojo, H., & Igarashi, Y. (2008). 2-Hydroxy-ceramide synthesis by ceramide synthase family: Enzymatic basis for the preference of FA chain length. *Journal of Lipid Research*, 49(11), 2356–2364. <https://doi.org/10.1194/jlr.M800158-JLR200>
- Mo, L., Tie, X., Che, F., Zhang, L., Li, B., Wang, G., & Yang, Y. (2024). A Novel Homozygous Deletion Including Exon 1 of FA2H Gene Causes Spastic Paraplegia-35: Genetic and Lipidomics Analysis of the Patients. *Pediatric Neurology*, 152, 200–208. <https://doi.org/10.1016/j.pediatrneurol.2023.12.031>
- Myelin Biogenesis: Vesicle Transport in Oligodendrocytes.
- Myelin-Associated Oligodendrocytic Basic Protein mRNAs Reside at Different Subcellular Locations (1999). *Journal of Neurochemistry*, 73(5), 1913–1924. <https://doi.org/10.1046/j.1471-4159.1999.01913.x>
- Nicole Baumann and Danielle Pham-Dinh. Biology of Oligodendrocyte and Myelin in the Mammalian Central Nervous System.
- Pan, Z., Kao, T., Horvath, Z., Lemos, J., Sul, J.-Y., Cranstoun, S. D., . . . Cooper, E. C. (2006). A common ankyrin-G-based mechanism retains KCNQ and NaV channels at electrically active domains of the axon. *The Journal of Neuroscience : The Official Journal of the Society for Neuroscience*, 26(10), 2599–2613. <https://doi.org/10.1523/JNEUROSCI.4314-05.2006>
- Pankiv, S., Clausen, T. H., Lamark, T., Brech, A., Bruun, J.-A., Outzen, H., . . . Johansen, T. (2007). P62/sqstm1 binds directly to Atg8/LC3 to facilitate degradation of ubiquitinated protein aggregates by autophagy. *The Journal of Biological Chemistry*, 282(33), 24131–24145. <https://doi.org/10.1074/jbc.M702824200>
- Park, H., Kang, J.-H., & Lee, S. (2020). Autophagy in Neurodegenerative Diseases: A Hunter for Aggregates. *International Journal of Molecular Sciences*, 21(9). <https://doi.org/10.3390/ijms21093369>
- Parrilla, G. E., Gupta, V., Wall, R. V., Salkar, A., Basavarajappa, D., Mirzaei, M., . . . You, Y. (2024). The role of myelin in neurodegeneration: Implications for drug targets and neuroprotection strategies. *Reviews in the Neurosciences*, 35(3), 271–292. <https://doi.org/10.1515/revneuro-2023-0081>
- Pereira-Dutra, F. S., Teixeira, L., Souza Costa, M. F. de, & Bozza, P. T. (2019). Fat, fight, and beyond: The multiple roles of lipid droplets in infections and inflammation. *Journal of Leukocyte Biology*, 106(3), 563–580. <https://doi.org/10.1002/JLB.4MR0119-035R>
- Perlman, R. L. (2016). Mouse models of human disease: An evolutionary perspective. *Evolution, Medicine, and Public Health*, 2016(1), 170–176. <https://doi.org/10.1093/emph/eow014>
- Pernber, Z., Richter, K., Mansson, J.-E., & Nygren, H. (2007). Sulfatide with different fatty acids has unique distributions in cerebellum as imaged by time-of-flight secondary ion mass spectrometry (TOF-SIMS). *Biochimica Et Biophysica Acta*, 1771(2), 202–209. <https://doi.org/10.1016/j.bbalip.2006.12.007>
- Peter, F., Rost, S., Rolfs, A., & Frech, M. J. (2017). Activation of PKC triggers rescue of NPC1 patient specific iPSC derived glial cells from gliosis. *Orphanet Journal of Rare Diseases*, 12(1), 145. <https://doi.org/10.1186/s13023-017-0697-y>
- Potter, K. A., Kern, M. J., Fullbright, G., Bielawski, J., Scherer, S. S., Yum, S. W., . . . Hama, H. (2011). Central nervous system dysfunction in a mouse model of FA2H deficiency. *Glia*, 59(7), 1009–1021. <https://doi.org/10.1002/glia.21172>
- Raghavan, S., & Kanfer, J. N. (1972). Ceramide Galactoside of Enriched Neuronal and Glial Fractions from Rat Brain. *Journal of Biological Chemistry*, 247(4), 1055–1056. [https://doi.org/10.1016/S0021-9258\(19\)45614-7](https://doi.org/10.1016/S0021-9258(19)45614-7)

- Rasband, M. N., & Peles, E. [Elior] (2015). The Nodes of Ranvier: Molecular Assembly and Maintenance. *Cold Spring Harbor Perspectives in Biology*, 8(3), a020495. <https://doi.org/10.1101/cshperspect.a020495>
- Rasband, M. N., & Peles, E. [Elior] (2016). The Nodes of Ranvier: Molecular Assembly and Maintenance. *Cold Spring Harbor Perspectives in Biology*, 8(3), a020495. <https://doi.org/10.1101/cshperspect.a020495>
- Rattay, T. W., Lindig, T., Baets, J., Smets, K., Deconinck, T., Söhn, A. S., . . . Schüle, R. (2019). Fahn/spg35: A narrow phenotypic spectrum across disease classifications. *Brain : A Journal of Neurology*, 142(6), 1561–1572. <https://doi.org/10.1093/brain/awz102>
- Ravanelli, A. M., & Appel, B. (2015). Motor neurons and oligodendrocytes arise from distinct cell lineages by progenitor recruitment. *Genes & Development*, 29(23), 2504–2515. <https://doi.org/10.1101/gad.271312.115>
- Ravera, S., & Panfoli, I. (2015). Role of myelin sheath energy metabolism in neurodegenerative diseases. *Neural Regeneration Research*, 10(10), 1570–1571. <https://doi.org/10.4103/1673-5374.167749>
- Redmond, S. A., Mei, F., Eshed-Eisenbach, Y. [Yael], Osso, L. A., Leshkowitz, D., Shen, Y.-A. A., . . . Chan, J. R. (2016). Somatodendritic Expression of JAM2 Inhibits Oligodendrocyte Myelination. *Neuron*, 91(4), 824–836. <https://doi.org/10.1016/j.neuron.2016.07.021>
- Reggiori, F. (2006). 1. Membrane origin for autophagy. *Current Topics in Developmental Biology*, 74, 1–30. [https://doi.org/10.1016/S0070-2153\(06\)74001-7](https://doi.org/10.1016/S0070-2153(06)74001-7)
- Romero Rosales, K., Singh, G., Wu, K., Chen, J., Janes, M. R., Lilly, M. B., . . . Edinger, A. L. (2011). Sphingolipid-based drugs selectively kill cancer cells by down-regulating nutrient transporter proteins. *The Biochemical Journal*, 439(2), 299–311. <https://doi.org/10.1042/BJ20110853>
- Rowitch, D. H. (2004). Glial specification in the vertebrate neural tube. *Nature Reviews. Neuroscience*, 5(5), 409–419. <https://doi.org/10.1038/nrn1389>
- Roza, C., Castillejo, S., & Lopez-García, J. A. (2011). Accumulation of Kv7.2 channels in putative ectopic transduction zones of mice nerve-end neuromas. *Molecular Pain*, 7, 58. <https://doi.org/10.1186/1744-8069-7-58>
- Rubinsztein, D. C., Mariño, G., & Kroemer, G. (2011). Autophagy and aging. *Cell*, 146(5), 682–695. <https://doi.org/10.1016/j.cell.2011.07.030>
- Rupps, R., Hukin, J., Balicki, M., Mercimek-Mahmutoglu, S., Rolfs, A., & Dias, C. (2013). Novel Mutations in FA2H-Associated Neurodegeneration: An Underrecognized Condition? *Journal of Child Neurology*, 28(11), 1500–1504. <https://doi.org/10.1177/0883073812458538>
- Saab, A. S., Tzvetanova, I. D., & Nave, K.-A. (2013). The role of myelin and oligodendrocytes in axonal energy metabolism. *Current Opinion in Neurobiology*, 23(6), 1065–1072. <https://doi.org/10.1016/j.conb.2013.09.008>
- Sango, K., Yamauchi, J., Ogata, T., & Susuki, K. (2019). *Myelin* (Vol. 1190). Singapore: Springer Singapore. <https://doi.org/10.1007/978-981-32-9636-7>
- Schneider, A., Länder, H., Schulz, G., Wolburg, H., Nave, K.-A., Schulz, J. B., & Simons, M. (2005). Palmitoylation is a sorting determinant for transport to the myelin membrane. *Journal of Cell Science*, 118(Pt 11), 2415–2423. <https://doi.org/10.1242/jcs.02365>
- Schulze, H., & Sandhoff, K. (2011). Lysosomal lipid storage diseases. *Cold Spring Harbor Perspectives in Biology*, 3(6). <https://doi.org/10.1101/cshperspect.a004804>
- Simons, M., Misgeld, T., & Kerschensteiner, M. (2014). A unified cell biological perspective on axon-myelin injury. *The Journal of Cell Biology*, 206(3), 335–345. <https://doi.org/10.1083/jcb.201404154>
- Simons, M., & Nave, K.-A. (2015). Oligodendrocytes: Myelination and Axonal Support. *Cold Spring Harbor Perspectives in Biology*, 8(1), a020479. <https://doi.org/10.1101/cshperspect.a020479>

- Simons, K., & Sampaio, J. L. (2011). Membrane organization and lipid rafts. *Cold Spring Harbor Perspectives in Biology*, 3(10), a004697. <https://doi.org/10.1101/cshperspect.a004697>
- Simonsen, A., & Tooze, S. A. (2009). Coordination of membrane events during autophagy by multiple class III PI3-kinase complexes. *The Journal of Cell Biology*, 186(6), 773–782. <https://doi.org/10.1083/jcb.20090701>
- Snaidero, N., Möbius, W., Czopka, T., Hekking, L. H. P., Mathisen, C., Verkleij, D., . . . Simons, M. (2014). Myelin membrane wrapping of CNS axons by PI(3,4,5)P₃-dependent polarized growth at the inner tongue. *Cell*, 156(1-2), 277–290. <https://doi.org/10.1016/j.cell.2013.11.044>
- Snaidero, N., Velte, C., Myllykoski, M., Raasakka, A., Ignatev, A., Werner, H. B., . . . Simons, M. (2017). Antagonistic Functions of MBP and CNP Establish Cytosolic Channels in CNS Myelin. *Cell Reports*, 18(2), 314–323. <https://doi.org/10.1016/j.celrep.2016.12.053>
- Speicher, A. M., Wiendl, H., Meuth, S. G., & Pawlowski, M. (2019). Generating microglia from human pluripotent stem cells: Novel in vitro models for the study of neurodegeneration. *Molecular Neurodegeneration*, 14(1), 46. <https://doi.org/10.1186/s13024-019-0347-z>
- St Johnston, D. (2005). Moving messages: The intracellular localization of mRNAs. *Nature Reviews. Molecular Cell Biology*, 6(5), 363–375. <https://doi.org/10.1038/nrm1643>
- Sun, L. O., Mulinyawe, S. B., Collins, H. Y., Ibrahim, A., Li, Q., Simon, D. J., . . . Barres, B. A. (2018). Spatiotemporal Control of CNS Myelination by Oligodendrocyte Programmed Cell Death through the TFEB-PUMA Axis. *Cell*, 175(7), 1811–1826.e21. <https://doi.org/10.1016/j.cell.2018.10.044>
- Sural nerve biopsies from workers with a history of chronic exposure to organic solvents and from normal control cases.
- Susuki, K. (2013). Node of Ranvier disruption as a cause of neurological diseases. *ASN Neuro*, 5(3), 209–219. <https://doi.org/10.1042/AN20130025>
- Susuki, K., & Rasband, M. N. (2008). Molecular mechanisms of node of Ranvier formation. *Current Opinion in Cell Biology*, 20(6), 616–623. <https://doi.org/10.1016/j.ceb.2008.09.007>
- Takahashi, K., Tanabe, K., Ohnuki, M., Narita, M., Ichisaka, T., Tomoda, K., & Yamanaka, S. (2007). Induction of pluripotent stem cells from adult human fibroblasts by defined factors. *Cell*, 131(5), 861–872. <https://doi.org/10.1016/j.cell.2007.11.019>
- Takahashi, K., & Yamanaka, S. (2006). Induction of pluripotent stem cells from mouse embryonic and adult fibroblast cultures by defined factors. *Cell*, 126(4), 663–676. <https://doi.org/10.1016/j.cell.2006.07.024>
- Tekirdag, K., & Cuervo, A. M. (2018). Chaperone-mediated autophagy and endosomal microautophagy: Joint by a chaperone. *The Journal of Biological Chemistry*, 293(15), 5414–5424. <https://doi.org/10.1074/jbc.R117.818237>
- Tonelli, A., D'Angelo, M. G. [M. G.], Arrigoni, F., Brighina, E., Arnoldi, A., Citterio, A., . . . Bassi, M. T. [M. T.] (2012). Atypical adult onset complicated spastic paraparesis with thin corpus callosum in two patients carrying a novel FA2H mutation. *European Journal of Neurology*, 19(11), e127-9. <https://doi.org/10.1111/j.1468-1331.2012.03838.x>
- Trajkovic, K., Dhaunchak, A. S., Goncalves, J. T., Wenzel, D., Schneider, A., Bunt, G., . . . Simons, M. (2006). Neuron to glia signaling triggers myelin membrane exocytosis from endosomal storage sites. *The Journal of Cell Biology*, 172(6), 937–948. <https://doi.org/10.1083/jcb.200509022>
- Traka, M., Arasi, K., Avila, R. L., Podojil, J. R., Christakos, A., Miller, S. D., . . . Popko, B. (2010). A genetic mouse model of adult-onset, pervasive central nervous system demyelination with robust remyelination. *Brain : A Journal of Neurology*, 133(10), 3017–3029. <https://doi.org/10.1093/brain/awq247>
- Uchida, Y., Hama, H., Alderson, N. L., Douangpanya, S., Wang, Y., Crumrine, D. A., . . . Holleran, W. M. (2007). Fatty acid 2-hydroxylase, encoded by FA2H, accounts for differentiation-

- associated increase in 2-OH ceramides during keratinocyte differentiation. *The Journal of Biological Chemistry*, 282(18), 13211–13219. <https://doi.org/10.1074/jbc.M611562200>
- Uncini, A., Susuki, K., & Yuki, N. (2013). Nodo-paranodopathy: Beyond the demyelinating and axonal classification in anti-ganglioside antibody-mediated neuropathies. *Clinical Neurophysiology : Official Journal of the International Federation of Clinical Neurophysiology*, 124(10), 1928–1934. <https://doi.org/10.1016/j.clinph.2013.03.025>
- Vaz, I. M., Borgonovo, T., Kasai-Brunswick, T. H., Santos, D. S. D., Mesquita, F. C. P., Vasques, J. F., . . . Brofman, P. R. S. (2021). Chromosomal aberrations after induced pluripotent stem cells reprogramming. *Genetics and Molecular Biology*, 44(3), e20200147. <https://doi.org/10.1590/1678-4685-GMB-2020-0147>
- Völkner, C., Liedtke, M., Petters, J., Huth, K., Knuebel, G., Murua Escobar, H., . . . Frech, M. J. (2020). Generation of an iPSC line (AKOSi006-A) from fibroblasts of an NPC1 patient, carrying the homozygous mutation p.I1061t (c.3182 T C) and a control iPSC line (AKOSi007-A) using a non-integrating Sendai virus system. *Stem Cell Research*, 49, 102056. <https://doi.org/10.1016/j.scr.2020.102056>
- Vries, H. de, Jonge, J. C. de, Schrage, C., van der Haar, M. E., & Hoekstra, D. (1997). Differential and cell development-dependent localization of myelin mRNAs in oligodendrocytes. *Journal of Neuroscience Research*, 47(5), 479–488. [https://doi.org/10.1002/\(SICI\)1097-4547\(19970301\)47:5<479::AID-JNR3>3.0.CO;2-E](https://doi.org/10.1002/(SICI)1097-4547(19970301)47:5<479::AID-JNR3>3.0.CO;2-E)
- Wake, H., Lee, P. R., & Fields, R. D. (2011). Control of local protein synthesis and initial events in myelination by action potentials. *Science (New York, N.Y.)*, 333(6049), 1647–1651. <https://doi.org/10.1126/science.1206998>
- Wang, S., Bates, J., Li, X. [Xiaojie], Schanz, S., Chandler-Militello, D., Levine, C., . . . Goldman, S. A. (2013). Human iPSC-derived oligodendrocyte progenitor cells can myelinate and rescue a mouse model of congenital hypomyelination. *Cell Stem Cell*, 12(2), 252–264. <https://doi.org/10.1016/j.stem.2012.12.002>
- Wang, D., & Hiesinger, P. R. (2012). Autophagy, neuron-specific degradation and neurodegeneration. *Autophagy*, 8(4), 711–713. <https://doi.org/10.4161/autophagy.19660>
- Wedel, M., Fröb, F., Elsesser, O., Wittmann, M.-T., Lie, D. C., Reis, A., & Wegner, M. (2020). Transcription factor Tcf4 is the preferred heterodimerization partner for Olig2 in oligodendrocytes and required for differentiation. *Nucleic Acids Research*, 48(9), 4839–4857. <https://doi.org/10.1093/nar/gkaa218>
- Weerachayanukul, W., Probohdh, I., Kongmanas, K., Tanphaichitr, N., & Johnston, L. J. (2007). Visualizing the localization of sulfoglycolipids in lipid raft domains in model membranes and sperm membrane extracts. *Biochimica Et Biophysica Acta*, 1768(2), 299–310. <https://doi.org/10.1016/j.bbamem.2006.08.022>
- Wickner, W. (2010). Membrane fusion: Five lipids, four SNAREs, three chaperones, two nucleotides, and a Rab, all dancing in a ring on yeast vacuoles. *Annual Review of Cell and Developmental Biology*, 26, 115–136. <https://doi.org/10.1146/annurev-cellbio-100109-104131>
- Winterstein, C., Trotter, J., & Krämer-Albers, E.-M. (2008). Distinct endocytic recycling of myelin proteins promotes oligodendroglial membrane remodeling. *Journal of Cell Science*, 121(Pt 6), 834–842. <https://doi.org/10.1242/jcs.022731>
- Yamagata, M., Obara, K., & Kihara, A. (2011). Sphingolipid synthesis is involved in autophagy in *Saccharomyces cerevisiae*. *Biochemical and Biophysical Research Communications*, 410(4), 786–791. <https://doi.org/10.1016/j.bbrc.2011.06.061>
- Zhang, Y., Bekku, Y., Dzhashiashvili, Y., Armenti, S., Meng, X., Sasaki, Y., . . . Salzer, J. L. (2012). Assembly and maintenance of nodes of ranvier rely on distinct sources of proteins and targeting mechanisms. *Neuron*, 73(1), 92–107. <https://doi.org/10.1016/j.neuron.2011.10.016>

- Xie Z, Klionsky DJ. Autophagosome formation: core machinery and adaptations. *Nat Cell Biol.* 2007 Oct;9(10):1102-9. doi: 10.1038/ncb1007-1102. PMID: 17909521.
- Zhang SC, Wernig M, Duncan ID, Brüstle O, Thomson JA. In vitro differentiation of transplantable neural precursors from human embryonic stem cells. *Nat Biotechnol.* 2001 Dec;19(12):1129-33. doi:10.1038/nbt1201-1129. PMID: 11731781
- Zöller, I., Meixner, M., Hartmann, D., Büssow, H., Meyer, R., Gieselmann, V., & Eckhardt, M. (2008). Absence of 2-hydroxylated sphingolipids is compatible with normal neural development but causes late-onset axon and myelin sheath degeneration. *The Journal of Neuroscience : The Official Journal of the Society for Neuroscience*, 28(39), 9741–9754. <https://doi.org/10.1523/JNEUROSCI.0458-08.20>

9 List of Figures

Figure 1: The process of 2-OH sphingolipid formation

Figure 2: Domain organization of FA2H gene

Figure 3: Neurogenesis and oligodendrogenesis processes from neuroectodermal tube development

Figure 4: Myelin wrapping and compaction

Figure 5: Organisation and molecular composition of myelinated axon sub-domains

Figure 6: Timeline of O4+ oligodendrocyte generation

Figure 7: Timeline of O4+ oligodendrocyte generation

Figure 8: Timeline of O4+ oligodendrocyte generation

Figure 9: Timeline of coculture generation

Figure 10: Reprogramming of fibroblasts into iPSCs via Sendai virus.

Figure 11: Detection of pluripotency markers in the established iPSC line

Figure 12: Analysis of pluripotency-related proteins via flow cytometry is depicted

Figure 13: Detection of pluripotency-associated genes using RT-PCR

Figure 14: Results of the RT-PCR expression analysis of the transgenes

Figure 15: The iPSCs clones spontaneously differentiated into cell types representative of the three germ layers

Figure 16: The karyogram of the established FAHN iPSC line

Figure 17: Generation of Neural Progenitor Cells

Figure 18: Generation of Neural Differentiated Cells

Figure 19: Representative images of the main stages of the protocol for the generation of OLs using the lentiviral-based methodologies

Figure 20: Oligodendrocyte precursor cells generating from iPSCs

Figure 21: Oligodendrocyte precursor cells differentiation process.

Figure 22. Example of a FACS dot plot for the number of O4+ cells within the culture after 10 d of SOX10 induction

Figure 22. Example of a FACS dot plot for the number of O4+ cells within the culture after 10 d of SOX10 induction

Figure 24: FA2H protein analysis in Neural Differentiated Cells

Figure 25: FA2H protein analysis in Oligodendrocyte Precursor Cells

- Figure 26: Fluorescence intensity of FA2H protein in Neural Differentiated Cells.
- Figure 27: Fluorescence intensity of FA2H protein Oligodendrocyte Precursor Cells.
- Figure 28: Analysis of myelin protein MBP in Oligodendrocyte Precursor Cells and coculture.
- Figure 29: Analysis of myelin PLP protein in Oligodendrocyte Precursor Cells and coculture.
- Figure 30: Colocalisation analysis of PLP-MBP in Oligodendrocyte Precursor Cells
- Figure 31: Colocalisation analysis of PLP-MBP in the coculture of neurons and OLs
- Figure 32: Colocalisation analysis of PLP-MAP2 in the coculture of neurons and OLs
- Figure 32: Colocalisation analysis of MBP-MAP2 in the coculture of neurons and OLs
- Figure 33: Expression of Kv7.2 channels in myelinated axon.
- Figure 34: Structure of myelinated axon in FAHN
- Figure 35: Expression of Kv7.2 channels in myelinated axon, node of Ranvier
- Figure 36: Analysis of the expression of p62 during autophagy
- Figure 37: Analysis of LC3B expression during autophagy
- Figure 38: Detection of pluripotency markers in the established iPS cells
- Figure 39: Flow cytometric analysis of pluripotency-associated protein

10 Table

Table 3.1: Instrument

Table 3.2: Chemicals and reagents

Table 3.3: Commercially available kits

Table 3.4: Cell culture media and supplements

Table 3.5: Growth factors and small molecules

Table 3.6: Composition of buffers and solutions

Table 3.7: Standards and dyes

Table 3.8: Primary antibodies

Table 3.9: Secondary antibodies

Table 3.10: Conjugated primary antibodies for flow cytometry

Table 3.11: Primers

Table 3.12: Microorganism strain used

Table 3.13: Culture media for growing the micro-organism strain

Table 3.14: Consumables

Table 3.15: Plasmids

Table 3.16: Software

Table 3.17: Cell culture media used

Table 3.18: Control and FAHN cell lines used in the study

Table 3.19: Cell lines used

Table 3.20: Cell culture media used

Table 3.21: Cryopreservation of cells

Table 3.22: Thermal Profile of the Reverse Transcription Reaction

Table 3.23: Program for qPCR

Table 3.24: Seeding parameters of neural differentiated cells

Table 3.25: Calculate the required amount of viral vector

Table 3.26: 4% polyacrylamide-SDS stacking gel

Table 3.26: 15% polyacrylamide-SDS stacking gel

Table 4.1: STR Analysis of FAHN cell line

Table 4.2: Result of mutation analysis

Table 4.3: Measurements on myelinated axon

11 Abbreviation

AD	Alzheimer's disease
ALS	Amyotrophic lateral sclerosis
AP	Alkaline phosphatase
ATG3	Autophagy-related protein 3
ATG4	Autophagy-related protein
BafA1	Bafilomycin A1
BMP	Bone morphogenetic protein
BSA	Bovine serum albumin
CNP	2',3'-cyclic nucleotide 3'-phosphodiesterase
CNS	Central nervous system
DES	Dihydroceramide desaturase
DMEM	Dulbecco's Modified Eagle's Medium
DMSO	Dimethyl sulfoxide
EB	Embryoid body
ER	Endoplasmic reticulum
FA2H	Fatty acid 2-hydroxylase
FAHN	Fatty acid hydroxylase-associated neurodegeneration
FGF2	Basic fibroblast growth factor
GAPDH	Glyceraldehyde-3-phosphate dehydrogenase
gDNA	genomic DNA
GFAP	Glial fibrillary acid protein
GlcCer	Glucosylceramides
GSL	Glycosphingolipids
HBSS	Hank's buffered salt solution
HD	Huntington's disease

h-iPSCs	human induced Pluripotent Stem Cell
HSP	Hereditary spastic paraplegia
IF	Immunofluorescence
iPSC	Induced pluripotent stem cell
JXP	Juxtaparanodal junctions
KO	Knockout
LC3BI/II	Microtubule-associated proteins 1A/1B light chain 3B
LSM	Laser scanning microscope
MAG	Myelin-associated glycoprotein
MAP2	Microtubule-associated protein 2
MBP	Myelin binding protein
MOG	Myelin oligodendrocyte glycoprotein
NBIA	Neurodegeneration with Brain Iron Accumulation
NDCs	Neuronal differentiated cells
NGS	Next Generation Sequencing
NIM	Neural Induction Medium
NP-C 1/2	Niemann–Pick disease type C 1/2
NPCs	Neural progenitor cells
OLs	Oligodendrocytes
OMIM	Online Mendelian Inheritance in Man
OPCs	Oligodendrocyte progenitors
PBS	Phosphate-buffered saline
PD	Parkinson’s disease
PDGFR α	Platelet-derived growth factor receptor alpha
PFA	Paraformaldehyde
PLP	poly-L-ornithine

Abbreviation

pMN	Motor neuron progenitor domain
PNJ	Paranodal axoglial junctions
PNS	Peripheral Nervous System
pre-OPC	pre-oligodendrocyte progenitora
PSA-NCAM	Polysialylated-neural cell adhesion molecule
qPCR	quantitative polymerase chain reaction
RA	Retinoic acid
RT	Room temperature
SHH	Sonic hedgehog
SM	Sphingomyelins
SNARE	Soluble N-ethylmaleimide-sensitive-factor attachment receptors
SQSTM1/p62	Sequestosome-1
STR	Short tandem repeat

12 Additional figures

12.1 Characterisation of the cell systems

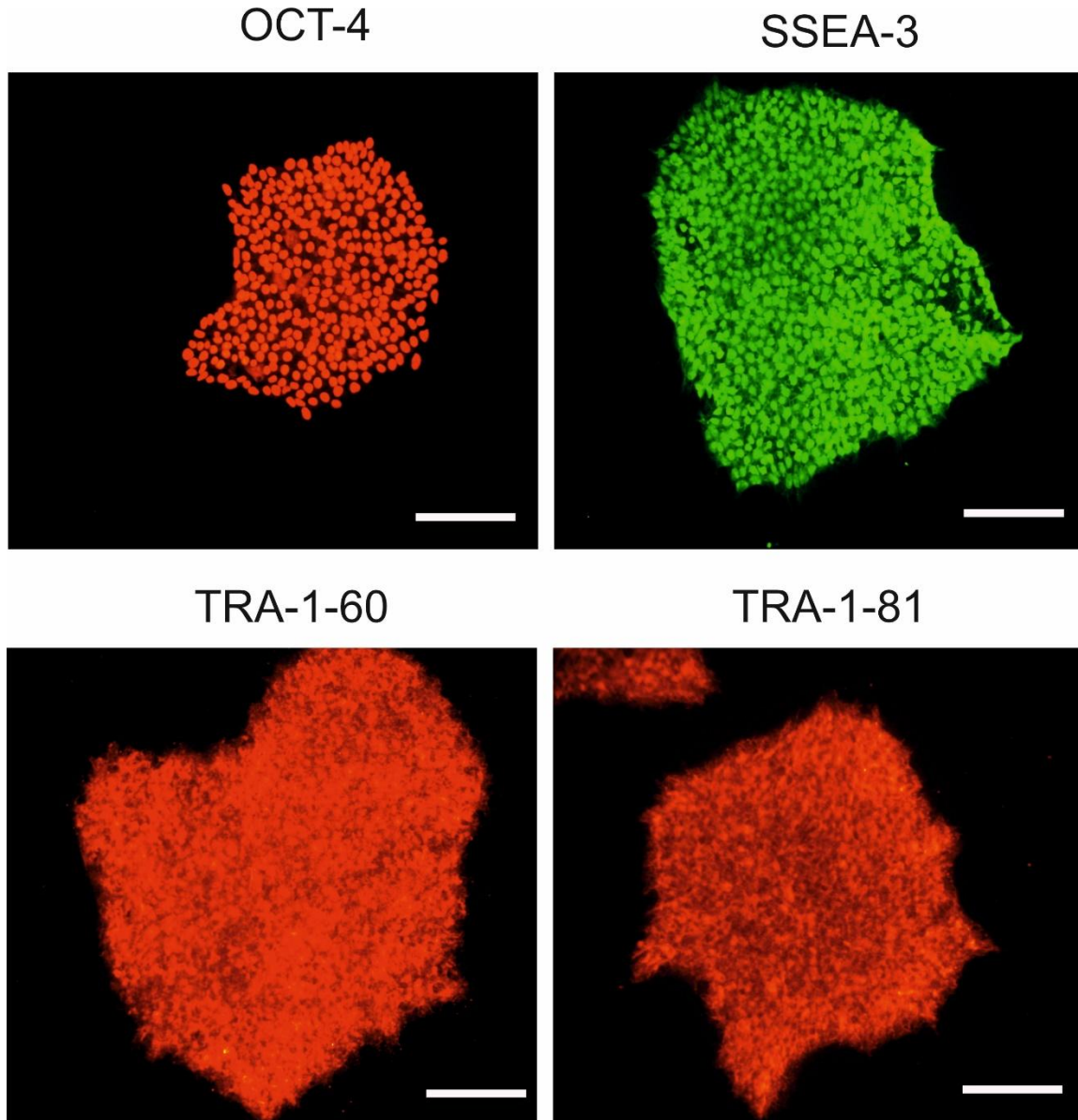


Figure 38: Detection of pluripotency markers in the established iPS cells. The immunocytochemical staining shows that the iPS cell line is positive for the pluripotency markers OCT4 SSEA3, TRA-1-60 and TRA-1-81. Scale 200 μ m.

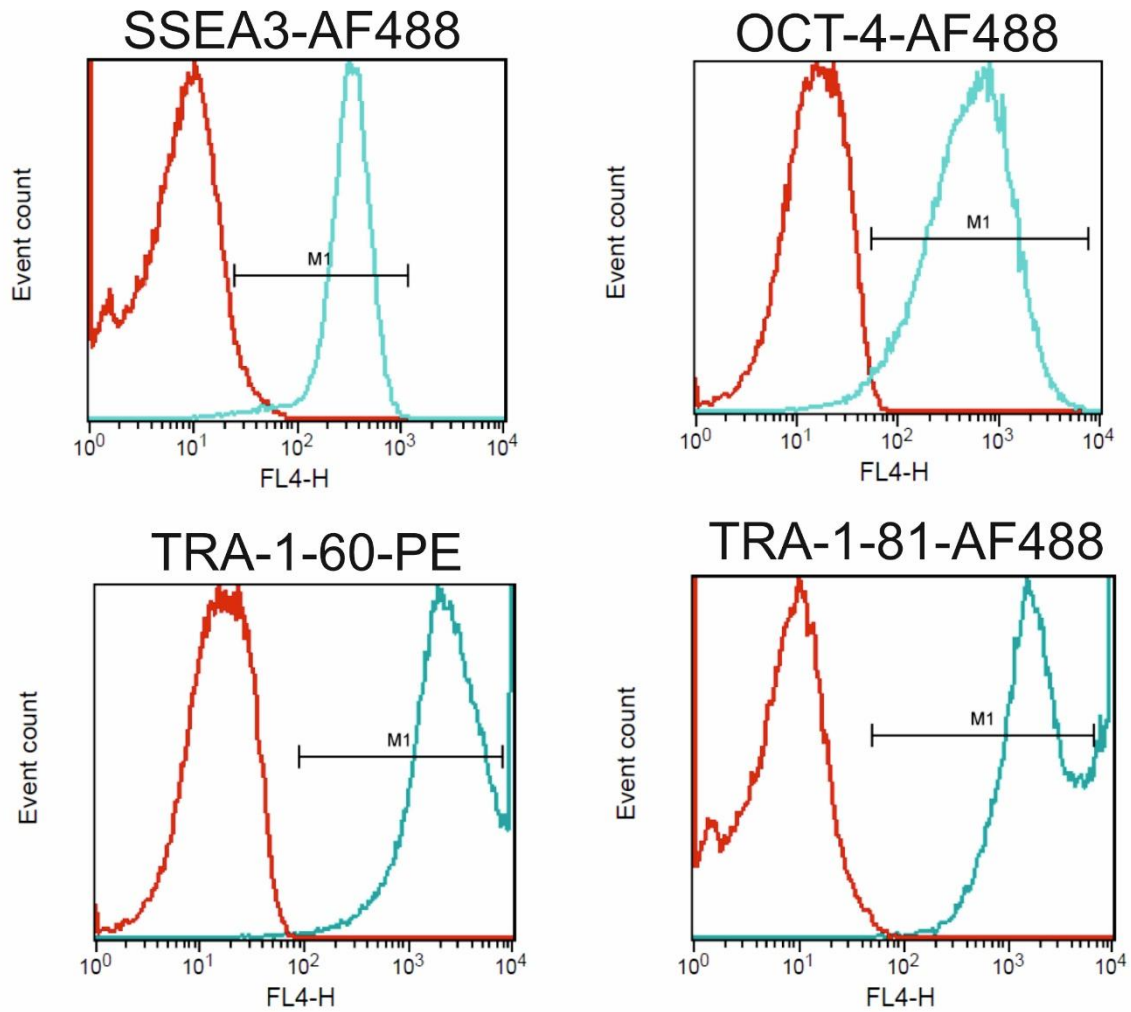


Figure 39: Flow cytometric analysis of pluripotency-associated proteins. The representative histograms show the relative fluorescence intensities of the pluripotency-associated proteins SSEA3, OCT4, TRA-1-60 and TRA-1-81 in the FA2H-deficient iPS cell line versus the relative number of events. The unstained negative control is shown in red; the right shift of the signal after staining with the corresponding fluorescence-coupled primary antibodies is shown in green. The numbers in the histograms indicate the percentage of positive cells. The analysis shows that the pluripotency-associated proteins are expressed in almost all cells of FA2H-deficient cell line.

13 Acknowledgements

I would like to thank Prof Dr. Dr. Andreas Hermann for the opportunity to do my doctorate in the 'Albrecht Kossel' Section for Translational Neurodegeneration. Furthermore, I would like to express my sincere thanks to him for placing a lot of trust in me and my work and encouraging me to work independently. I am extremely grateful for his commitment in supervising me, his constant willingness to help and the valuable suggestions that contributed to the success of this thesis. I also greatly appreciate the fact that he always encouraged me to attend conferences and seminars, which gave me the opportunity to broaden my scientific horizons.

In particular, I would like to thank PD Dr Moritz Frech for his supervision during the implementation and realisation of the thesis, as well as for the good discussions and advice during this time.

I would like to extend my gratitude to Dr. Sunita Venkateswaran from the laboratory of our esteemed collaborator at the Children's Hospital of Eastern Ontario, Canada, for her invaluable contribution in providing us with FAHN patient fibroblast cell lines.

I am extremely grateful to Prof. Dr. Markus Kipp for his invaluable scientific assistance in the preparation of the grant proposal and for his insightful recommendations.

I would also like to thank the staff of the Core Facility for Cell Sorting and Cell Analysis, especially Wendy Bergmann, for her support with flow cytometry, as well as for the constructive discussions and feedback on the experimental setup and data analysis.

I would also like to thank PD Dr. Hugo Murua Escobar, Saskia Krohn and Gudrun Knübel from the Medical Clinic III for Hematology, Oncology and Palliative Medicine for the good cooperation and the sequencing of the cells.

I would like to thank my sensei, Prof. Dr. Dr. Sasaki Katsunori and his wife, for always believing in me, motivating me even when I lost hope. He also never forgets about my birthday and provided me with the best matcha and Japanese snacks at the right time.

I would also like to thank my all friends, but separately to Aida, Julia, Martha, Annaliis, Sawako, Kenta, Takashi, Kubra. Thank you for always being there, for your support, for cheering me up, listening to frustrations, and for the ideas and discussion we had.

I would also like to thank all my all beautiful colleagues and staff at the Section for Translational Neurodegeneration 'Albrecht Kossel', who have supported me with advice and assistance in carrying out my work. Despite occasional problems, it was always a pleasure to work with you. Zahvaljujem se mojoj majki, sestri, bratu i cijeloj mojoj porodici na strpljenju, ohrabrenju i podršci tokom studiranja, doktorske disertacije i svih drugih životnih situacija. Zahvalan sam vam svima na podršci.

Finally, I would like to thank my daughter Sare and my husband Hamza Salih, who have had to put up with my moods and idiosyncrasies over the last three years, but have always supported me. You were always there to give me support and give me a hug, especially in difficult and depressing situations. I'm sorry you two were separated for so long, three years, while I was achieving my dream.

14 Declaration

I, Fatima Efendic, solemnly declare that the thesis entitled

"In Vitro Disease Modeling and Pathophysiological Characterization of Fatty Acid Hydroxylase-Associated Neurodegeneration (FAHN) Using Neural Lineage Cells Derived from Patient-Specific Induced Pluripotent Stem Cells (iPSCs)"

was independently authored by me. No assistance was sought beyond the aids explicitly acknowledged herein. All sources from which I have borrowed text or derived ideas, either directly or indirectly, have been appropriately cited.

Moreover, I affirm that this scientific work has been conducted in strict accordance with the principles of good scientific practice as stipulated by the valid 'Rules to ensure good scientific practice and to avoid scientific misconduct' at the University of Rostock.

Rostock 2024

Fatima Efendic

Curriculum Vitae

Personal Data

Name: Fatima Efendic

Date of Birth: 22.02.1991

Place of Birth: Bosnia and Herzegovina

Nationality: Bosnian

Contact: (+49) 16 28 98 28 57

Address: Bergstraße 7A, 18057 Rostock, Germany

Email: Fatima.efendich@gmail.com

Education

01/2021 – Present

PhD Student, Translational Neurodegeneration Section "Albrecht Kossel" Department of Neurology, University Medical Center Rostock, Thesis Topic: "In Vitro Disease Modeling and Pathophysiological Characterization of Fatty Acid Hydroxylase-Associated Neurodegeneration"

2017 – 2019

Master of Science in Medical Histology & Embryology Istanbul University, Turkey

Final Grade: 3.8 (German grading 1.2) Thesis Topic: "Histological and Biochemical Changes on Isolated Preimplantation and Early Post-Implantation Rats' Embryos Investigated by Zinc Oxide Nanoparticles and Potential Protective Effects of L-arginine"

2012 – 2016

Bachelor Degree in Genetic and Molecular Biology, Bilecik Seyh Edebali University, Turkey

Final Grade: 3.1 (German grading 1.6) Thesis Topic: "E. coli Oxidative Stress Related Mutation Detection Epigenetic Studies on Human Ovary Cancer Cells"

Work Experience

01/2021 – Present

Research Assistant, Section for Translational Neurodegeneration "Albrecht-Kossel" Clinic and Polyclinic for Neurology, University Medicine Rostock; Responsibilities: In vitro iPSCs modeling into neural and glial cells, CRISPR CAS9 approach, 2D and 3D cell culture, myelination

07/2017 – 05/2019

Research Trainee, Histology and Embryology; University of Health Science (UHS), Turkey Responsibilities: Ovary damage, oocyte isolation, embryo pluripotency, endometriosis

06/2014 – 08/2015

Researcher Trainee, Shinshu Medical University, Japan

Responsibilities: Induced pluripotent stem cell research, cardiovascular pluripotent stem cells

Skills

Languages:

- Bosnian: Mother language
- English: Fluent
- Turkish: Fluent
- German: Basic

Computer Skills:

- MS Office: Very good knowledge
- GraphPad Prism: Very good knowledge
- Snapgene: Very good knowledge
- ImageJ, FCSalyzer, Corel Draw, Emperia Studio: Very good knowledge
- Python: Basic knowledge

Lab & Professional Skills:

- General Cell Culture: 2D, 3D cell culture, iPSC modeling, animal surgery experiments (A, B, C certificate course)
- Molecular Biology: PCR, qPCR, RNA, DNA handling, cloning techniques, site-directed mutagenesis, CRISPR/Cas9 gene editing, Western blot, Flow cytometry
- Microscopy & Imaging Techniques: Live staining, immunohistochemistry, immunofluorescence, fluorescent microscopy techniques, confocal microscopy (LSM)

Teaching Experience

13 – 17.03.2023

Rostock Spring School of Neurodegenerative Diseases Neuroscience Practical Course:
Cellular Models of Neurodegenerative Diseases Differentiation of iPSC to neurons and glia

Participation in Scientific Conferences

25-27.09.2024

12th German Stem Cell Network (GSCN) Conference in Jena, Germany

08 – 11.07.2023

XVI European Meeting on Glial Cells in Health and Disease, Berlin

14.03.2023

Schilling-Symposium, Rostock

25 – 27.01.2023

Lund & Rostock Winter School in Gut Gremmelin

13 – 15.10.2022

The 8th International Symposium on NBIA, Lausanne, Switzerland

Prizes and Awards

2024: Travel grant award- 12th GSCN Conference in Jena, Germany

2023: Grant awards Professorinnenprogramm III

2022: Grant award - CTNR Research Fellowship (Centre for Transdisciplinary Neurosciences)

10/2022: Travel grant award - The 8th International Symposium on NBIA in Lausanne, Switzerland

2021: NBIA Research Fellowship

2018: BAP Research Fellowship

Scientific Publications

Manuscript Under submission in Cells Journal: **Efendic, F.**, et al. (2024). “*In Vitro Disease Modeling and Pathophysiological Characterization of Fatty Acid Hydroxylase-Associated Neurodegeneration*”

Efendic, F., et al. (2023). *Generation of the human iPSC lines AKOSi011-A carrying the mutation p.Pro65ser/p.Asp35t and AKOSi012-A, carrying the mutation p.Tyr231his, derived from FAHN patient fibroblasts.* Stem Cell Research, 71, 103178. <https://doi.org/10.1016/j.scr.2023.103178>

Efendic, F., et al. (2022). *Generation of the human iPSC line AKOSi010-A from fibroblasts of a female FAHN patient, carrying the compound heterozygous mutation p.Gly45arg/p.His319arg.* Stem Cell Research, 63, 102863. <https://doi.org/10.1016/j.scr.2022.102863>

Efendic, F., et al. (2022). *Histological and biochemical apoptosis changes of female rats' ovary by Zinc oxide nanoparticles and potential protective effects of L-arginine: An experimental study.* Annals of Medicine and Surgery, Volume 74, 2022, 103290. ISSN 2049-0801.

Sapmaz, T., **Efendic, F.**, et al. (2022). *Effects of metformin, letrozole and atorvastatin on inflammation and apoptosis in experimental peritoneal and ovarian endometriosis in the rat.* Pathology - Research and Practice, Volume 235, 2022, 153951. ISSN 0344-0338.